AN INVESTIGATION OF AUTOMATIC PROCESSING TECHNIQUES FOR TIME-LAPSE MICROSCOPE IMAGES

YUEXIANG LI, MSc.

**Thesis submitted to the University of Nottingham
for the degree of Doctor of Philosophy**

JULY 2016

Abstract

The field of image processing has been extensively investigated, and many algorithms have been developed for it. With the rapid development of digital-image processing, image-processing techniques have been successfully applied to different areas including the monitoring system, production-line control and artificial intelligence.

The analysis of time-lapse microscope images is a recent popular research topic. Processing techniques have been employed in such studies to extract important information about cells—e.g., cell number or alterations of cellular features—for various tasks. However, few studies provide acceptable results in practical applications because they cannot simultaneously solve the core challenges that are shared by most cell datasets: the image contrast is extremely low; the distribution of grey scale is non-uniform; images are noisy; the number of cells is large; and cell behaviours include moving, splitting, merging, appearing and disappearing. These factors also make manual processing an extremely laborious task.

The motivation behind this thesis is to establish a framework that can improve the efficiency of related biological analyses and disease diagnoses. The aim is to develop sophisticated techniques that can automatically process time-lapse microscope images and thereby meet specific demands for different tasks rapidly and accurately.

This thesis establishes a framework in these directions: a new segmentation method for cell images is designed as the foundation of an automatic approach for the measurement of cellular features. The newly proposed segmentation method achieves substantial improvements in the detection of detailed information about, for example, cell filopodia. In addition, an automatic measuring mechanism for cell features is established in the designed framework. The measuring component enables the system to provide

quantitative information about various cell features that are useful in biological research, including length and width of cells, cell size, cell volume and cell shape. Using the extracted measures of cell features, a novel cell-tracking framework is constructed to monitor the alterations of cells. The tracking framework associates cells in adjacent frames based on a newly defined scoring scheme with an accuracy of cell tracking above 90%.

Processing speed is another bottleneck in automatic analyses of medical images. Few of the existing algorithms can be employed in real-time applications because most of them are used for complicated structures or require prior-knowledge to achieve excellent performance and therefore involve expensive computations. In addition, due to the development of high-resolution microscopes, there is an obvious rise in the size of captured cell images that increase the challenge faced by existing algorithms.

To address the issue of processing speed, two fast-processing techniques have been developed to complete edge detection and visual tracking. For edge detection, the new detector is a hybrid approach that is based on the Canny operator and fuzzy entropy theory. The method calculates the fuzzy entropy of gradients from an image to decide the threshold for the Canny operator. For visual tracking, a newly defined parameter is employed in the fast-tracking mechanism to recognize different cell events, such as mitosis, merging and entering. Both of the methods have been evaluated with real cell datasets. The results demonstrate their excellent performance in terms of tracking accuracy: i.e., 97.66%, and processing speed, i.e., 0.578s/frame.

List of Publications

1. **Yuexiang LI**, Siu-Yeung CHO, 'A method for cell image segmentation using both local and global threshold techniques', *International Symposium on Multispectral Image Processing and Pattern Recognition (MIPPR)*. 2013 [Chapter 3]

2. **Yuexiang LI**, Siu-Yeung CHO, John Crowe, 'A tracking system for mouse stem cells', *Optics Within Life Sciences (OWLS)*. 2014 [Chapter 4]

3. **Yuexiang LI**, Siu-Yeung CHO, John Crowe, 'A Hybrid Edge Detection Method for Cell Images based on Fuzzy Entropy and the Canny Operator', *Journal of Image and Graphics*, 2(2), 135-139. [Chapter 5]

Acknowledgements

I wish to record my deepest gratitude to my supervisors, Prof. David Cho Siu-Yeung and Prof. John Crowe, who offered their constructive advice and patient guidance through every step of my PhD career. I gained a lot of professional knowledge from them and learned how to be a qualified researcher. Their thoughtful suggestions and continual passion have constantly encouraged me as I have faced challenges and difficulties with my research. I am grateful to have them as my supervisors. Working with them has been a very rewarding experience in my life.

I would like to thank the University of Nottingham for granting me the intercampus scholarship to pursue my PhD. Thanks to the colleagues in SEB-412 who made the room an excellent place to do research and kindly provided much help with my studies. Special thanks to the iBIOS team from the University of Nottingham, United Kingdom, and to Dr. Carlos Ortiz de Solorzano from the Centre for Applied Medical Research, Pamplona (Spain) who provided me substantial samples of microscopic images with which to implement and evaluate the designed algorithms.

Finally, I would like to thank Miss Yibei Shen for her companionship during my PhD career and my family for their continuous support and encouragement during my 20-year journey as a student.

Table of Contents

List of Figures

List of Tables

Chapter 1   Introduction

1.1 Background

Image-processing techniques have been developed over thirty decades. Since the successes of image digitization in the beginning of twentieth century [1], the field of image processing has gained growing interest from institutional researchers. A number of processing techniques have been developed for tasks that vary from image-quality enhancement to aided-analysis tool in applications such as surveillance systems. Through these endeavours, digital-image-processing techniques have been applied successfully in a broad area that includes the development of geometry information systems, analysis of biological images and artificial intelligence.

Analysis of time-lapse microscope images is a popular topic in the field of image processing. Due to the development of high-resolution microscopes, many cell behaviours can be directly observed from captured images. However, manual processing is an extremely laborious task, as there are often more than hundreds of cells in a series of frames. Thus, analyses of time-lapse experiments increasingly rely on automatic image-processing techniques. The

primary aspects of experimental monitoring are the extraction of cell features and the detection of cell behaviours. The common features used in most biological studies are shape measures of cells, such as the length, width and thickness. These features are important because cells alter their shapes when they encounter changes in external conditions. Biologists can try to understand the mechanisms of cells dealing with different environments through measuring the cell features. Cell behaviours are another important measure in the monitoring of the life cycle of cells. Cells perform distinct behaviours, such as mitosis and merging, in each stage of their growing process. The measure of these activities is extremely important for pathology studies or research on drug testing [2]. Therefore, these factors result in a growing need for high-accuracy automatic-processing techniques for time-lapse microscope images in biological research.

This research aims to develop sophisticated techniques that automatically process time-lapse microscope images that fulfil specific demands in different biological analyses. The focus of this study is on developing automatic frameworks that improve performance in practical applications such as monitoring cell features and tracking cell trajectories. The motivation of this endeavour is to help establish a better understanding of the mechanisms of cell mobility and the effects of varying external environments in the life cycle of cells. The research focuses on developing superb automatic processing techniques exclusively for microscope images. The newly developed techniques will be compared with existing methods to evaluate their performance and to evaluate their potential for real-world applications.

1.2 Motivations

Microscope images are used in numerous biological analyses. Thus, which approach should be used to accurately process and extract important information from the sample images is a typical issue in the research area. Several challenges are shared by the practical applications of microscope images: the image contrast is extremely low; the distribution of grey scale is non-uniform; the images are noisy; the volume of cells contained in the dataset

is huge; and events such as mitosis must be accurately detected. These factors make it hard for the automatic framework to produce accurate measures. Furthermore, since few previous studies have investigated these challenges as an independent topic, automatic processing techniques can gain limited improvements. Tasks such as cell tracking are therefore often manually completed. However, due to the huge volume of cells contained in a series of frames, manual processing can be extremely laborious and time-consuming. Errors made by human eyes are inevitable, because cells are blurred in microscope images. The situation implies an urgent demand for high-performance automatic-processing techniques that are specially designed for microscope images.

In the biomedical area, image-processing techniques have been applied to facilitate analyses of microscope images. For example, the automatic counting system for the white blood cells suggested in [3] shortens the period of disease diagnoses. Microscope images provide plenty of information about the length, size, and shape of cells. Compared to cell counting, the extraction and measurement of these features are more sophisticated processes that require professional automatic processing techniques. To provide better aids in biological studies, this study aims to establish the frameworks that are needed to meet the following qualities.

A. Quantitative

Microscope images have been used in biology for decades; however, due to the lack of efficient aid tools, researchers are accustomed to analysing their images qualitatively rather than quantitatively. The shapes of cells vary as conditions change in their surrounding environments. Measurements of cell features, such as cell size and cell length can provide much useful information in cell monitoring. Automatic processing techniques offer a solution to the problem of quantitative analysis. The designed framework is supposed to measure various required features of each cell contained in a series of time-lapse frames that assist related studies and extend the research area.

B. Accurate

Manual manipulation is high influenced by subjective factors. Human eyes are the primary source of errors in processing. Although computer analysis is objective, the rate of accurate measurement that can be obtained with computers cannot meet the requirements of practical applications because few existing methods can solve the challenges associated with microscope images. Thus, the accuracy of the framework is particularly important for automating the analysis procedure. The primary analysis provided by existing commercial systems is to track the alterations of cells during their life cycles. Accurate rates of cell tracking by traditional approaches—about 70% [4]—are unacceptable for practical analyses. To solve this problem, this study aims to increase the rate to above 90%.

C. Extendable

The features of different types of cells are discriminated. Therefore, biological applications may have special requirements for processing different microscope images. The expansibility of a framework describes how hard it is for that system to process different datasets. Existing approaches are usually difficult to expand, as most of them are designed to solve special problems in particular type of cells or require strict conditions to ensure good performance. We aim to establish a general framework that can be separated to processing modules. Modules work on respective tasks. The whole system can complete different special missions by combinations of modules that can be applied to diverse cell datasets in various medical imaging applications.

D. Efficient

Automatic image-processing techniques can obviously reduce the workload for researchers and shorten the time consumed in manipulations. For example, it takes about 1 minute to manually count about 100 cells in a microscope images that can be shortened by the software to a few seconds. In the actual analyses, there are often thousands of cells in each frame of the video. The operations are more complicated than counting cell numbers. Thus, automatic processing techniques offer outstanding advantages for dealing with huge

datasets. Although existing methods can provide efficient performance, their processing speeds are too slow for real-time applications due to their complex structures. Therefore, another focus of this study is to develop fast processing techniques that can be easily utilized in real-time analyses.

1.3 Contributions

The major contributions made by this study to the field of medical image processing are summarized in the following entries.

1. A novel segmentation technique for detailed detection in cell images

Since image segmentation is an essential prerequisite to analyses [5] such as feature measurement and tracking, the performance of the method used for image segmentation is of particular importance. Thousands of studies have been made in this field in previous research; however, few can detect the cell filopodia. The neural cells use their antennas to transfer information. The alterations of those antennas often have significant meanings in biological analyses. To solve this problem, a novel segmentation method that uses both local and global thresholding techniques is proposed. This hybrid method accurately detects cells to achieve, for example, a 49.66% segmentation accuracy for the rat mesenchymal stem-cell dataset.

2. A framework with excellent performance in cell tracking

The mechanisms of cell motility and their regulation can provide a great deal of information about various biological processes such as embryonic development [6]. Automatic cell tracking is an efficient tool for the quantitative analysis of those processes. However, because the quality of cell images is often low, and because various cell behaviours including mitosis, fusion, and rapid movement must be recognized, most of the existing tracking approaches have been developed for complex structures or work only under strict conditions. A general tracking framework that can be extensively used to track different types of cells is presented. A two-step iterative thresholding approach is developed to remove segmentation errors, and a scoring scheme that uses multiple cell features is proposed for association. For performance

evaluation, this system is applied to four different cell datasets. The results demonstrate that the proposed framework outperforms the winner of ISBI 2013: i.e., it achieved a 92.93% tracking accuracy.

3. Fast-processing techniques for time-lapse cell images

Due to the development of high-resolution microscopes, the size of captured cell images can be extremely large: i.e., often above $900{\times}900$. Although existing image-processing techniques can provide highly accurate performance with these large-size images, few of them can be utilized in real-time applications. Two of the fast-processing techniques are developed exclusively for time-lapse cell images.

3.1 A hybrid edge-detection method

Edge detection is widely used to analyse cell images by cell biologists. Thus, the accuracy of the technique is pivotal to their work. Due to the often low quality of cell images, existing edge detectors fail to routinely produce highly accurate results. To solve this problem, a novel hybrid method is proposed that is based on the Canny operator and fuzzy entropy theory. This method calculates the fuzzy entropy of gradients from an image to decide the threshold for the Canny operator. Its great potential for practical applications is indicated by the processing speed of the proposed detector, which is less than 0.5 sec/frame.

3.2 A fast tracking technique

Automatic tracking can provide efficient statistical measures that are hard to obtain from manual analysis. Existing tracking frameworks can provide accurate results; however, most of them are designed in complex structures or require prior-knowledge that results in low processing speeds. Growing numbers of biological applications require accurate and fast tracking techniques. Hence, a fast tracking framework is proposed. A new cell similarity is defined so that the tracking component can detect most cell behaviours, including mitosis, merging and entering. The framework has been implemented for real-cell datasets and evaluated with respect to the results of

participants in the challenge section of ISBI 2013, which demonstrate the excellent performance of our proposed framework in both tracking accuracy (above 97%) and processing speed (0.578 second/frame).

1.4 Thesis Outline

This thesis consists of six chapters. The project is introduced in Chapter 1. Chapter 2 reviews current technical developments, including segmentation and tracking techniques previously proposed for biological analyses. These techniques form the foundation and provide a multitude of important ideas for the optimization of this work.

In Chapter 3, the novel segmentation method for the detection of cell antennas is introduced (*section* **3.2**). This segmentation method has been compared with several methods that are widely used in recent studies (*section* **3.2.4**). Based on segmentation results, various features of cells that are useful in biological analyses can be measured (*section* **3.3**). The proposed segmentation method and its variants have been applied to the cell dataset captured by University of Nottingham, UK (UNUK), as a case study (*section* **3.4**).

Chapter 4 introduces the proposed framework for cell images. The framework has been applied to three datasets of different types of cells that have been collected by world-wide famous institutions such as the Academy of Sciences of the Czech Republic. The principle under the designed tracking system (*section* **4.2**) is introduced first. Then performances are analysed using different cell features (*section* **4.4.3.1**). Three widely used methods are taken as benchmarks for the performance evaluation of the proposed tracking framework (*section* **4.4.3.2**).

Chapter 5 focuses on fast-processing techniques. The hybrid edge-detection method is introduced first (*section* **5.2**). Then the fast tracking technique is demonstrated (*section* **5.3**). These two techniques have been applied to real cell datasets; their performances have been evaluated via benchmark methods for accuracy and process speed (*section* **5.3.2** and *section* **5.5.2.2**).

In Chapter 6, contributions made by this study are discussed, suggestions for future work are presented, and a general conclusion is summarized.

Chapter 2   Literature Review

With the development of imaging techniques, the quality of medical images gains an obvious enhancement that reduces the difficulties for image-processing techniques to provide reliable results, thus a growing number of image-processing techniques are implemented in medical applications. The automatic techniques improve the efficiency of many tasks. For examples, the task of tracking cells manually costs huge volume of labour since the number of cells in a time-lapse video can be extremely large. Substantial studies on these essential techniques, such as image segmentation, have been made in previous research. The advantages and drawbacks of existing approaches have been comprehensively analysed and improvements for the methods have been developed to provide better performance.

This chapter provides a review of developments of the core techniques involved in this research area, including image segmentation and visual tracking. The theories and properties of the widely used segmentation techniques are provided in the first section. In the second section, the relationship between tracking and the processes of segmentation is presented

within an introduction to the development of tracking techniques. Since this research involves a study of measuring cells from a 3D view, a general review of existing 3D-reconstruction techniques is included in the third section.

2.1 Techniques for cell segmentation

The area of image segmentation has been studied extensively since the early 20th century. As image-processing techniques have been implemented in various practical applications, image-segmentation—the essential step for most processing operations—is a subject of increasing attention. Thousands of approaches have been developed from various theories. A brief review of cell segmentation approaches can be found in [7]. Some of these approaches are highly accepted by researchers and widely implemented in biological applications. Therefore, an introduction to the theories and properties of these existing segmentation methods is presented in the rest of this section.

2.1.1 Thresholding

Thresholding is a traditional method for image segmentation. Due to its simplistic structure, the technique can be easily implemented and requires low calculation capacity to produce stable performance. Therefore, thresholding techniques have been widely used to process biological images, such as the images of blood cells in [8]. This technique separates the pixels in the target image into separate classes by using different threshold values [9]. Assume the original image is $f(x,y)$. Then the thresholding result, $g(x,y)$, can be presented as follows:

$$g(x,y) = \begin{cases} C_N & if\ f(x,y) \geq T_N \\ C_{N-1} & if\ T_{N-1} \leq f(x,y) < T_N \\ & \cdots \\ C_1 & if\ T_1 \leq f(x,y) < T_2 \\ C_0 & if\ f(x,y) < T_1 \end{cases} \tag{2.1}$$

where $(T_1 \ldots T_N)$ represents the set of threshold values and $(C_0 \ldots C_N)$ are the corresponding classes.

In most applications, the technique is used to differentiate only two classes: object and background. The success of this method is based on the assumption that the neighbouring pixels in the same class have close grey values. Using a histogram view, the object area and background are related to different distribution in the figure. Hence, the valley point (T) between the two peaks is chosen as a threshold to separate the two parts.
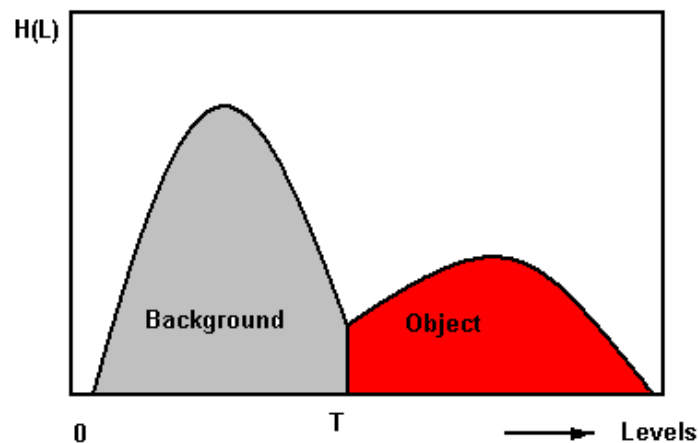
Figure 2-1 Histogram of an Image

Therefore, the core of the thresholding techniques is its way of seeking suitable threshold values. Otsu proposed the value maximized the inter-class variance as the threshold [10]. Kaptur used entropy theory to decide the threshold [11]. Doyle chose the threshold through the P-tile algorithm [12]. Among these traditional approaches, the method proposed by Otsu is highly accepted in later research. Many variants of this typical method have been developed [13].

However, traditional Otsu thresholding has poor performance with most cell images, because the datasets share the following three core challenges: the contrast is extremely low, distribution of grayscale is non-uniform, and the images are noisy. Low-contrast images often lead to no distinct valley in their histograms. It is hard for the Otsu thresholding method to accurately process such images. D. Ye developed a pre-processing technique that uses morphological operators to enhance the quality of MR images [14]. The results demonstrate the excellent performance of the method, which has been

extended to use with microscope images. The traditional Otsu method determines the threshold only by using the image histogram, which results in its sensitivity to noise and in inhomogeneous distributions of grayscales. To address these problems, B. Ma separates the whole image into several sub-images and processes each sub-image using the Otsu thresholding. The method produces the final results by assembling the binary sub-images and removes noises using the morphological operator [15]. Helon V. H. Ayala published a recent paper that introduces the application of novel beta differential evolution (BDE) according to Otsu's criterion to perform image segmentation [16]. In evaluated case studies, the proposed BDE approach performs better in terms of the quality of the final solutions.

2-D Otsu thresholding is another direction for algorithm improvements. The method uses the average values of the pixel values and the surrounding pixels to form a 2-D histogram. Using the generated 2-D histogram, the method chooses the threshold through the Otsu algorithm. The spatial information of the image makes an effective aid in the 2-D Otsu thresholding method. Thus, the robustness of the method to noises has been improved. 2-D Otsu has been broadly investigated and substantial improvements for the method have been proposed [17]. It has been used to process medical images in recent research. S. Kumar suggested using the 2-D Otsu algorithm to perform the segmentation of CT lung images. The proposed method is optimized by a differential evolution algorithm to reduce the computation complexity of 2D Otsu [18].

2.1.2 Edge operators

Based on the assumption that the image gradient changes sharply near cells borders, edge detection has been widely employed for image segmentation. A survey of various edge detectors can be found in [19]. Most techniques (e.g., Sobel, Roberts, and Prewitt) use a differentiation filter to approximate the first-order image gradient. If $f(x,y)$ is a raw image, the first-order gradient is defined as follows:

$$\nabla f(x, y) = \left[G_x, G_y \right]^T = \left[\frac{\partial f}{\partial x}, \frac{\partial f}{\partial y} \right]^T \qquad (2.2)$$

Following the generation of a gradient map, potential edges are extracted by thresholding the gradient. Based upon this approach, modified methods such as the Laplacian of Gaussian operator (LoG) have been established that use the second-order image derivative, also called the Laplacian magnitude, to extract edges. The Laplacian magnitude is defined by the following:

$$\nabla^2 f(x, y) = \frac{\partial^2 f(x, y)}{\partial x^2} + \frac{\partial^2 f(x, y)}{\partial y^2} \qquad (2.3)$$

In 1986, Canny proposed a method that has achieved widespread use. It first applies Gaussian derivatives to the image before isolating candidate edges by non-maximum suppression and extracting them via hysteresis thresholding [20]. The process can be expressed as follows:

$$M_a = \| f(x, y) * \nabla G_a(x, y) \| \qquad (2.4)$$

$$A_a = \frac{f(x, y) * \nabla G_a(x, y)}{\| f(x, y) * \nabla G_a(x, y) \|} \qquad (2.5)$$

where $G_a(x,y)$ represents the Gaussian operator. The boundary points are those that maximize M_a in the direction of A_a.

Approaches that improve the performance of the Canny operator have been developed. Elder and Zucker [21] introduced a method to determine edges at a multitude of scales. An adaptive smoothing method has also been proposed [22]. In more recent work, a method to extract edges missed by the Canny detector was suggested by Ding [23]. R. Medina-Carnicer has proposed a novel way to determine hysteresis thresholds in an unsupervised way [24].

Typical edge detectors share the same problem: sensitivity to noise. There are three main kinds of noise that may be contained in the images: Gaussian noise, Salt and Pepper noise and Poisson noise. Operators perform differently with respect to noise. Table 2-1 evaluates the performance of typical edge detectors

under different conditions.

Table 2-1 Comparison of different edge detection operators

Operator	Gaussian noise	Salt and Pepper noise	Poisson noise	Detail edges	Speed
Sobel	Good	Good	Good	Rough	Fast
Laplace	Poor	Poor	Poor	Accurate	Fast
Roberts	Good	Good	Good	Rough	Fast
Prewitt	Good	Good	Good	Rough	Fast
LoG	Poor	Very Poor	Very Poor	Accurate	Slow
Canny	Good	Good	Good	Accurate	Slow

The table reflects the fact that the Canny operator is more robust with respect to noise. Thus, the Canny operator is used in an increasing number of studies, including the analysis of medical images. N. S. Aruna tested several typical edge operators such as Canny and Sobel, to detect the edges of sickle cells in red blood cells. The study analysed the performance of the operators and concluded that the Canny edge-detection method is preferable for the diagnosis [25]. X. Zhang suggested a hybrid method that uses the Canny algorithm and mathematical morphology to extract cell edges [26]. The edges of cells are first estimated by the Canny operator; then the facture of the edges is filled in by the morphological operation of dilation. The results demonstrate that the combined method has the advantages of high accuracy and good quality of detected edges.

2.1.3 Mathematical Morphology

In recent years, mathematical morphology, which was first applied in image processing by J. Serra [27], has been attracting growing attention from researchers. The technique has been implemented for pre- or pro-processing of images in different systems. The crucial principle of this technique is to achieve the aim of image analysis by using the structural unit to measure and recognize the corresponding shape in the images. The essential operations in mathematical morphology are dilation, erosion and open and close. Sophisticated operators can be derived by combinations of these basic operations [28].

The morphological approach has a simplistic algorithm structure that makes it easier to implement. Furthermore, since spatial information is exploited in the typical morphological method, the technique has better robustness than the thresholding technique. Those factors result in the advantages of employing this approach in practical applications. T. U. Nipon used mathematical morphology to separate the nucleus and cytoplasm of white blood cells [29]. Although the designed edge detector is easy to implement, as it is sensitive to noise, it provides good performance only with high-quality images.

Sensitivity to noise is a traditional problem with the morphological method. Many solutions have been proposed in previous research. The watershed algorithm suggested by L. Vincent [30] is a representative solution for performance improvement. Generally speaking, the algorithm treats a grey-level image as a topographic relief in which the grayscales of pixels interpret their altitude, and it simulates a process of water dropping or flooding to the image to recognize the waterline between adjacent catchment basins. The waterlines represent the local maximums in the image; thus, the gradient map of the image is often used as input for the watershed method. If the image is represented by $f(x,y)$, the gradient map $g(x,y)$ can be presented as follows:

$$
\begin{aligned}
g(x,y) &= grad\big(f(x,y)\big) \\
&= \sqrt{(f(x,y) - f(x-1,y))^2 + (f(x,y) - f(x,y-1))^2}
\end{aligned}
\tag{2.6}
$$

Figure 2-2 uses a graphic view to show the example of gradient map and the positions of the waterline and catchment basins.

(a)

(b)

(c)

(d)
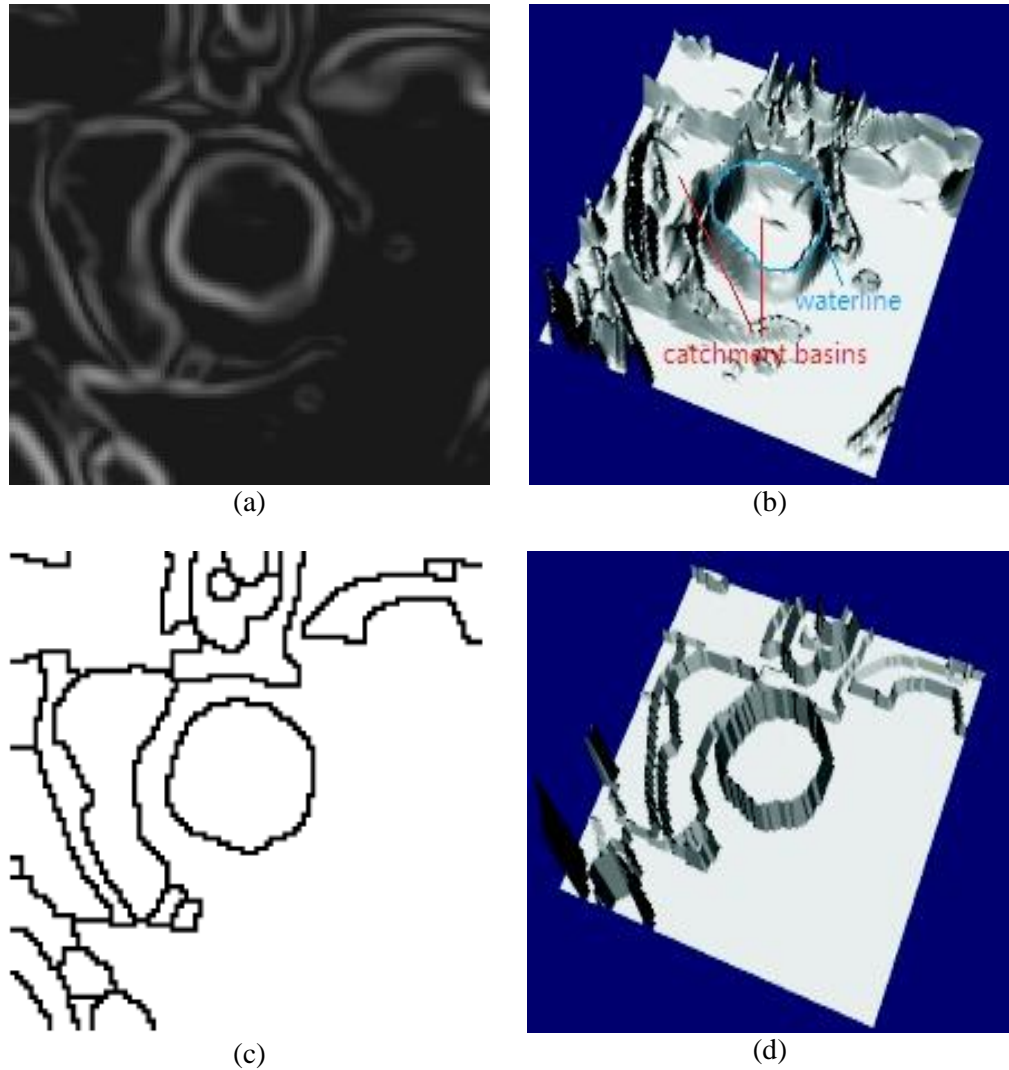
Figure 2-2 Example of gradient map. (a) Gradient image; (b) Relief of the gradient image; (c) Watershed of the gradient; (d) Relief of the waterlines.

The typical watershed algorithm can be organized as follows:

Step 1 – Generation of distance map: The pixels in the gradient-magnitude map are marked in an ascending order according to their pixel values.

Step 2 – Simulation of flooding: A flood is simulated within the marked gradient map such that the points with lower pixel values are submerged earlier. These inundated pixels are the local minimums in the images. Thus, the algorithm detects and marks these points with a FIFO scheme.

Step 3 – Recognition of waterlines: The gradient map is transformed to the image that contains the information of catchment basins after the process of

flooding. Based on this generated map, the algorithm marks the edge points between adjacent basins as waterlines and produces the final result.

The watershed algorithm performance very well in the detection of detailed edges; however, slight alterations of grey levels on the cell surfaces or unexpected noise can result in over-segmentation in the final results. The marker-based watershed labels the gradient map with foreground and background markers such that regional minimums can be only chosen from the marked points. This method removes the fake regional minimums influenced by noise and provides more accurate results. In [31], the revised marker-based watershed algorithm has been used to segment overlapping cells in microscope images.

The mathematical-morphology algorithm is often combined with other methods to reduce the influence of noise. For examples, D. Anoraganingrum proposed a method for segmenting tumour cells based on a median filter and morphological operation [32]. The image is smoothed by a median filter before segmentation by the morphological operator. This approach has been successfully applied to medical images; however, the drawback of the method is that it requires prior-knowledge and interaction from users for accurate segmentation. B. Chanda developed a hybrid method based on watershed and multi-dimensional morphological operators [33]. The method has been evaluated under noisy conditions, and results show that the approach is more robust than other morphological edge detectors. C. Jung recently developed a novel watershed-based method for the segmentation of cervical and breast cell images [34]. The approach has been tested on a variety of real microscope cell images, and results show that it yields more accurate segmentation results than the other watershed-based algorithms. The segmentation of red blood cells has also been achieved with the masking and watershed algorithm, which is introduced in [35].

2.1.4 Deformable model

The deformable model comprehensively utilizes information about regions and boundaries to recognize target edges. This method has been successfully applied for various purposes in image analysis, including segmentation, tracking, and pattern recognition. Thus, a growing number of studies focused on the deformable model have been presented in recent years [36]. The primary advantages of the deformable model are that it can produce integrated edge curves or surfaces and is robust with respect to noise and fake edges. The deformable model includes the deformable contour—also known as snakes or active contour—and the deformable surface that is an extension of the deformable contour for 3-D spaces.

The snakes model, which builds on the theory of energy minimization, was first proposed by M. Kass in 1987 [37]. It is basically a controlled continuity spline under the influence of image forces and external constraints. The snake is pushed by the image forces toward the images features, such as edges and object contours, and the responsibility of the external constraints put the snake near the local minimums. If point set V(s)=(x(s),y(s)) parametrically represents the position of a snake, its energy function can be written as follows:

$$E_{snake} = \int_0^1 E_{int}(v(s)) + E_{image}(v(s)) + E_{con}(v(s))ds \qquad (2.7)$$

where E_{int} is the internal energy of the spline produced by bending, E_{image} generates the image forces and E_{con} generates the external constraint forces.

Let $E_{ext} = E_{image} + E_{con}$, then the external forces (F_{ext}) are formed by the image forces and the external constraint forces. The internal energy (E_{int}) produces the internal forces (F_{int}) that resist deformation. Therefore, the model is supposed to finally be in a balanced state:

$$F_{int} + F_{ext} = 0 \qquad (2.8)$$

Because the original snakes model has various limitations and performs convergence poorly in some corner cases, variants of snakes have been developed. A brief introduction of the popular variants is provided in what follows.

A. GVF snakes model

C. XU proposed the idea of gradient vector flow (GVF) and suggested that GVF replace the traditional external force field in 1998 [38]. This variant model addresses the issue of poor convergence performance with snakes in two cases: 1) initialization of the snake is far from minimum and 2) the target has concave boundaries. The study defines edge map $f(x,y)$ derived from the image $I(x,y)$ as

$$f(x,y) = -E_{ext}^i(x,y) \qquad (2.9)$$

where i = 1, 2, 3, or 4.

If we define the gradient vector flow (GFV) field as the vector field $V(x,y) = (u(x,y), v(x,y))$, the energy functional of GVF can be written as follows:

$$E_{GVF} = \iint \mu\left(u_x^2 + u_y^2 + v_x^2 + v_y^2\right) + |\nabla f|^2 |V - \nabla f|^2 dx dy \qquad (2.10)$$

where μ is a controllable smoothing term.

E_{GVF} gives rise to the GVF forces (F_{GVF}) that are used to replace the default external force in this revised model. Although the GVF snakes model solves the problem of poor convergence, it has a primary drawback of its own: it smooths the edges of the contour with the smoothing term, μ. It is a trade-off issue. Although the rounding can be reduced by setting lower μ, the effect of smoothing is also weakened in this situation. A. Rajendran proposed a hybrid approach to segmenting brain tumours with the GVF snake model and fuzzy clustering [39]. F. Zhang developed an improved GVF snake model to perform contour extraction [40].

B. The balloon model

The balloon model was introduced by L. D. Cohen in [41]. The model was primarily designed to address the issue of shrinking in the default method. The typical snake shrinks inwards without substantial image forces and without mismatching its size with the minima contour. The image force is an important term in the default method that pushes the curve to the lines that correspond to the desired features. Assume the mapping of a snake for a contour s as $s \leftrightarrow v(s) = (x(s), y(s))$. The potential term of the image force is,

$$P(v) = -|\nabla I(v)|^2 \qquad (2.11)$$

where I is the image.

The curve is attracted by the local minima of the potential, and the image force can be represented in terms of the potential as follows:

$$F_{image} = -\nabla P \qquad (2.12)$$

Hence, the normalized term of the image force is, $F = -k \frac{\nabla P}{||\nabla P||}$, where k is the normalization factor. The study provides an analysis of the image forces and suggests that a new force—inflation—should be added to act on the snake and thereby provide a more dynamic behaviour for the contour. Combining the inflation term with the image force, the resultant can be expressed as follows:

$$F_{inflation} = k_1 \vec{n}(s) \qquad (2.13)$$

$$F = k_1 \vec{n}(s) - k \frac{\nabla P}{||\nabla P||} \qquad (2.14)$$

where k_1 is the magnitude of the force and $\vec{n}$ is the unit normal vector of the curve at $v(s)$.

The magnitude of k_1 should be the same as the image normalization factor k, and k should be slightly larger than k_1 to allow forces to stop the inflation at image edges. Therefore, the variant model can stop the shrinking of the default curve and guide the curve to the desirable attributes. In recent research, the

balloon snake model has been combined with fuzzy classification to achieve automatic segmentation of brain MR images [42].

C. Geometric active contours

The geometric snakes, geodesic snakes [43] and conformal active contours [44] are based on ideas from Euclidean curve-shortening evolution. The division and fusion of contours depend on the detection of objects in the image. "Level set" is a popular way to implement these revised models. In level-set based methods, the contour is seen as a point set in the zero level of a high dimensional surface. The model operates the surface to drive the curve towards the desirable edges. The process is depicted below.
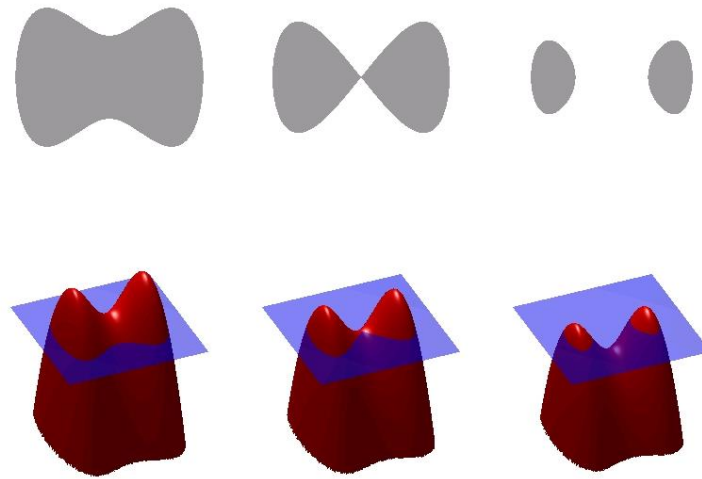
Figure 2-3 Process of curve alterations

If curve C moves along the normal direction at speed v, then the level set function φ satisfies the level set equation:

$$\frac{\partial \varphi}{\partial t} = v(k, I)\vec{n}|\nabla \varphi| \tag{2.15}$$

where I is the image, k is the curvature of the contour $v(k, I)$ is the speed function. $\vec{n}$ is the unitary normal vector of the contour. ∇ is the gradient operator.

Level-set deformable models provide excellent flexibility of topological alterations for the generated contours; thus, they have been extensively employed in biological applications. J. P. Bergeest proposed a segmentation approach for cell nuclei in 3D fluorescence microscopy images based on level-set deformable models and convex minimization [45]. An advanced version of level-set segmentation has been developed by O. Dzyubachyk. The approach is able to complete the task of accurate multi-cell segmentation that is difficult for default models. Seven modifications are implemented in the revised version to considerably improve its performance [46]. K. Zhang proposed a novel region-based active-contour model (ACM) and tested it with microscopic images in [47]. Although the level-set deformable model is acceptable for most applications, the expensive computation of the model is a barrier to better performance. Approaches to reduce the volume of computations have been suggested in recent studies [48].

2.1.5 Others

The field of image segmentation has been extensively studied and hundreds of approaches have been developed. Various new ideas or theories—such as genetic algorithm—have been successfully introduced in this filed to solve the segmentation issue. A brief introduction to other popular segmentation methods is presented in this section.

2.1.5.1 Region growing

Region growing is a method that has been broadly employed in the area of computer vision. A point set is initialized by the method as seeds. The seeds then grow by merging the neighbour pixels according to a pre-defined membership function. The region-growing approach has the advantage of a simple algorithm structure that makes for easily implemented and cheap computations. However, the default region-growing approach requires the manual setting of seed points and is sensitive to noises that influence its performance in practical applications. To address the drawbacks, S. Y. Wan suggested a symmetrical region-growing algorithm to provide a better robustness to noises [49]. L. Zheng created an automatic scheme for the

region-growing approach [50].

Region-growing segmentation has been successfully used to process microscope images. An automatic segmentation method for nuclei in 3D microscopy images of *C. elegans* was introduced by F. Long in [51]. The approach combines the region-growing technique with the watershed algorithm to perform automatic segmentation. Its performance demonstrates its robustness of intensity fluctuation with nuclei.

2.1.5.2 Neural network

W. E. Blanz and S. L. Gish first suggested using artificial neural network (ANN) to perform segmentation [52]. A forward three layers ANN is employed to segment the images. The attributes of the pixels are placed as the input nodes, and the output layer is the labels for each object in the image. The ANN model solves the problem of image segmentation from the view of pixel clustering in a manner that provides robust performance under noisy conditions. However, a large number of samples is required to pre-train the ANN models so they can provide accurate segmentation. Because it is difficult to collect substantial samples in some practical applications, this factor severely restricts the development of ANN models.

The neural network model is highly acceptable in medical applications. P. Phukpattaranont employed the neural network model and mathematical morphology to establish a segmentation of cancer cells in a microscopic tissue image of breast cancer [53]. The approach defines two classes for pixels in the areas of cells: P and N. The input layer of the neural network is the red-green-blue (RGB) component of the pixels; the output layer is the corresponding class for the pixels, background, P and N. The P and N pixels are translated to binary maps using the mathematical morphology to remove noise and fill holes. The approach combines two result binary maps and produces the final segmented image after post-processing. This method performs very well under both low and high histological noise conditions. Deep learning is a novel technique that uses the very deep neural network to address tasks such as face-recognition image processing. Recent studies have

used this technique to segment MR images [54].

2.1.5.3 Genetic algorithm

Genetic algorithm (GA) became popular particularly through J. Holland's 1970 book, *Adaptation in Natural and Artificial Systems*. The essential idea of the algorithm is to solve problems through a simulated evolutionary process of genes. The default genetic algorithm typically has four steps,

***Step 1 – Initialization*:** The GA proceeds to initialize a population of possible solutions. The size of the population depends on the nature of the problem. The initial population is randomly produced to cover the entire range of the search space.

***Step 2 – Selection*:** A proportion of the existing potential solutions are selected to breed a new generation during each successive generation. The solutions are selected through a fitness-based process according to which more fit solutions (as measured by a defined fitness function) are more likely to be selected.

***Step 3 – Genetic operators*:** The model generates a second-generation population of solutions from the selected potential solutions by using a combination of two genetic operators: crossover and mutation. Although these two operators are known as the typical genetic operators, other operators—such as colonization-extinction or regrouping—might also be employed.

***Step 4 – Termination*:** The generational process is repeated until it reaches a termination condition. Following provides examples of common terminating conditions: 1. The solution satisfying the minimum criteria is found. 2. The number of generations reaches the fixed limit. 3. Manually inspect.

The genetic algorithm is routinely utilized to generate solutions for optimization and to search for problems in various medical applications. B. Sahiner used GA to search suspicious areas in the X-ray image of a breast [55]. D.-H. Chen employed GA to segment ultrasound images of a heart [56]. A multilevel thresholding approach that uses the real coded genetic algorithm

was developed by S. Manikandan to segment medical brain images [57] . In recent research, the genetic algorithm has been applied to the problem of object registration (i.e., object detection, localization and recognition) in a set of medical images that contain different types of blood cells [58].

2.2 Techniques for cell tracking

Existing tracking algorithms in the field of computer vision can generally be classified as tracking by model evolution and tracking by detection. The principle of the former type is to find cells in the first frame and then update their position and shape through the entire sequence, frame-by-frame. Each tracking cell is processed by a model that evolves to fit the particular cell in subsequent frames. Contour evolution is the typical approach in this group. For the latter type, the key idea is to detect all cells in the entire time-lapse video and then to associate corresponding cells between adjacent frames. Examples for this group are typical segmentation and association and most stochastic filtering methods. The probabilistic objective function that associates cells is the core for this type of method. A brief review of existing cell-tracking methods can be found in [59].

Table 2-2 Comparison of three default models

	Contour evolution	Stochastic filtering	Segment and associate
Mitosis and merging	+	-	-
Appearing and disappearing	-	-	-
Low temporal resolution	-	+	+
Fast motion	-	+	+
Accurate segmentation	+	-	+

Several core challenges that occur during cell tracking are summarized: 1) accurate detection of mitosis and merging, 2) accurate detection of appearing and disappearing, 3) low temporal resolution of cell frames, 4) the tracking of cells with fast motions, and 5) accurate segmentation of cells. Studies have been made that compare the performances of the three typical tracking models

with respect to these challenges. Results are listed in the table below. The '+' indicates that the default method effectively handles the corresponding challenge, and the '-' indicates that the method has difficulties with the particular task.

The table clearly indicates that none of the three default models can simultaneously address all of the core challenges in cell tracking. Therefore, various improvements for the default models have been dramatically suggested in previous research. A brief review of the widely acceptable achievements is presented in the following.

2.2.1 Contour evolution

Contour evolution uses the deformable model to simultaneously perform segmentation and tracking tasks. In the tracking algorithm, the deformable model alters its shape to dynamically trace cells between adjacent frames. Many developments have been made in this field. For example, N. Ray introduces his work of applying the active contours with a modified energy functional to track leukocytes in [60]. C. Zimmer designed a tracking tool for cell-based drug testing by using parametric active contours [2].

In recent studies, most of the proposed methods are based on the theory of 'level set'. The advantage of this method is that it is easy to change the topology of contours; however, it requires large computations. D. P. Mukherjee and his colleagues proposed a framework of cell detection and tracking that uses image-level sets computed via threshold decomposition [61]. The level-set analysis makes it possible for this approach to automatically recognize and track multiple cells without the manual initialization step that is required in the methods based on default active contours. The energy functional that complements shape-based segmentation with a spatial-consistency tracking technique is integrated in the approach. It is with success of tracking rolling leukocytes from sampled time-lapse sequences. M. Maska presented a level-set-like and graph-cut framework in [62] to robustly track the evolving shape of whole fluorescent cells in a time-lapse series. The

framework has been simulated on 2-D and 3-D time-lapse series of rat adipose-derived mesenchymal stem cells and human lung squamous-cell carcinoma cells, respectively.

Although algorithms based on contour evolution have been developed in the past few decades, it is difficult to utilize the algorithm to track rapidly moving cell because the contour-evolution method needs overlapping areas of the same cell in neighbouring frames to perform recognition.

2.2.2 Stochastic filters

If the motion of the target object can be modelled, stochastic filters have extremely powerful performance. Mean-shift and Kalman filters can all be classified in this category.

2.2.2.1 Mean-shift

Mean-shift [63] is an analysis technique that is used to seek the maxima of a density function. It is an iterative method. Assume x as the initial estimate. The kernel function, $K(x_i - x)$, is given. The weighted mean of the density in the window determined by K can be represented as follows:

$$m(x) = \frac{\sum_{x_i \in N(x)} K(x_i - x) x_i}{\sum_{x_i \in N(x)} K(x_i - x)} \tag{2.16}$$

where $N(x)$ is the neighborhood of x_i, a set of points for which $K(x) \neq 0$.

The mean-shift algorithm sets $m(x) \rightarrow x$ and repeats the estimation until $m(x)$ converges. There are several frequently used choices for the kernel function, such as the Gaussian kernel:

$$K(x) = c_{k,d} k(||x||^2) \tag{2.17}$$

where $c_{k,d}$ is the normalization constant that makes $K(x)$ integrate to one, and $k(x)$ is called the profile of the kernel, which is $e^{-\frac{||x||^2}{2}}$ in the Gaussian kernel.

The mean-shift algorithm is an application-independent tool that makes it very well suited for the analysis of real data. This technique has been widely employed for various tasks in image processing, including pixel clustering and visual tracking. The algorithm tracks objects based on recursive estimations of the density function of the posterior probability and has been successfully used to process microscopic images. In [64], O. Debeir tracks the centroids of cells by updating centroid locations with the mean-shift algorithm. The accuracy of the centroid localization is of high importance in this algorithm.

2.2.2.2 Kalman filter

The Kalman filter [65] is based primarily on Bayesian theory. It offers a recursive solution for estimating the state of a process by minimizing the mean squared error. The filter is often conceptualized as two distinct steps: predict and update. The predict phase produces an estimate of the current state according to the state estimate from the previous time step. Since no observation information from the current time step is involved in this prediction of current state, this state estimate is therefore known as a priori state estimate. The following update phase then refines the state estimate by combining this a priori estimate with the results of current observations to produce the improved prediction: an a posteriori state estimate.

Phase 1 – Predict

The predicted (a prior) state estimate is represented as follows:

$$\hat{x}_{k|k-1} = F_k \hat{x}_{k-1|k-1} + B_k u_k. \tag{2.18}$$

The predicted (a prior) estimate error covariance is represented as follows:

$$P_{k|k-1} = F_k P_{k-1|k-1} F_k^T + Q_k \tag{2.19}$$

where F_k is the state transition model applied to the previous state x_{k-1}. B_k is the control-input model applied to the control vector u_k. $\hat{x}_{n|m}$ represents the estimate of x at time n given observation up to and including $m \leq n$.

Phase 2 – Update

The updated (a posteriori) state estimate is represented as follows:

$$\hat{x}_{k|k} = \hat{x}_{k|k-1} + K_k \tilde{y}_k. \qquad (2.20)$$

The updated (a posteriori) estimate error covariance is represented as follows:

$$P_{k|k} = (I - K_k H_k) P_{k|k-1} \qquad (2.21)$$

where K_k is the optimal Kalman gain. H_k is the observation model that maps the true state space to the observed space. $\tilde{y}_k$ is the measurement residual.

The Kalman filter has been applied in various fields, and has been largely developed to address particular issues in recent research. Consider, for example, the Extended Kalman filter (EKF) and Unscented Kalman filter (UKF). These variants can process the non-linear Gaussian model, which is difficult for typical Kalman filters. Improved algorithms have been proposed in various studies. W. J. Godinez developed a probabilistic-tracking approach that combined the Kalman filter with the principles of the particle filter [66]. The approach yields a more accurate performance than previous probabilistic approaches at very competitive computation times.

2.2.3 Segmentation and association

A segmentation-and-association algorithm first segments the objects in each frame across the sequence and then associates the same cells in different frames with the specific criteria. Therefore, this type of method can be routinely separated into two phases: segmentation and association. The quality of segmentation results is pivotal. Most of the algorithms mentioned previously have been tested with real datasets. X. Chen employed a revised hybrid approach that is based on the thresholding-and-watershed algorithm to segment cancer cell nuclei in time-lapse microscopy [67]. In the proposed framework, the Otsu thresholding technique is employed to produce binary

maps of the images. However, the thresholding technique fails to address the ambiguity caused by the overlapping nucleus. The improved watershed algorithm introduced in [68] is therefore applied to solve the issue. Experimental results from the hybrid method do an excellent job of segmenting cell nuclei, especially overlapping nuclei.

Object association is another core of segmentation-and-association tracking approaches. Various methods have been suggested. For example, in [69], C. D. Hauwer associated cells in adjacent frames by using the Euclidean distance. The robustness of this method is poor, because it detects tracks that rely heavily on information about the positions of the objects. In more recent researches, D. Padfield defined a tracking method for high-throughput cell images by using the coupled minimum-cost flow network [70]. R. Bise proposed a cell-association component by using global data association, which considers hypotheses of initialization, termination, translation, division and false positives in an integrated formulation [71]. F. Amat presented an open-source computational framework for the segmentation and tracking of cell nuclei in [72]. Klas E. G. Magnusson employed the Viterbi algorithm for cell association [73]. These algorithms perform well at specific tasks, but most of them are in complicated structures that require an enormous number of computations. A method must be developed that yields very accurate tracking with relatively little calculation.

2.3 Techniques for 3D reconstruction

Cell volume is a common measure that is employed in most biological studies. Since measurement of cell volume requires information about cell thickness, this method relies on techniques that can accurately reconstruct a 3-D view of cells. Phase unwrapping is widely used to establish this 3-D view. It constructs the 3-D model by the phase map that is rebuilt from a wrapped phase signal. Phase unwrapping can be separated to two catalogues: temporal-phase unwrapping [74, 75] and spatial-phase unwrapping. The difference between them is the rule to generate the phase map.

The temporal-phase unwrapping method captures several pieces of wrapped phase data in different time steps. It then produces the phase map by comparing the captured samples. Spatial-phase unwrapping, on the other hand, needs only one piece of wrapped phase. It unwraps the phase by comparing the values of different points in the captured map. Due to the mobility of cells, it is difficult to ensure that the images captured in different time steps have the same image topology. This limitation makes it hard for temporal-phase unwrapping to complete the reconstruction of a time-lapse microscopic video. The spatial-phase unwrapping method will be presented in details in followings.

In general, there are two primary types of spatial-phase unwrapping: path-dependent and path-independent. Figure 2-4 shows the general process of reconstructing a wrapped signal.

(a)   (b)
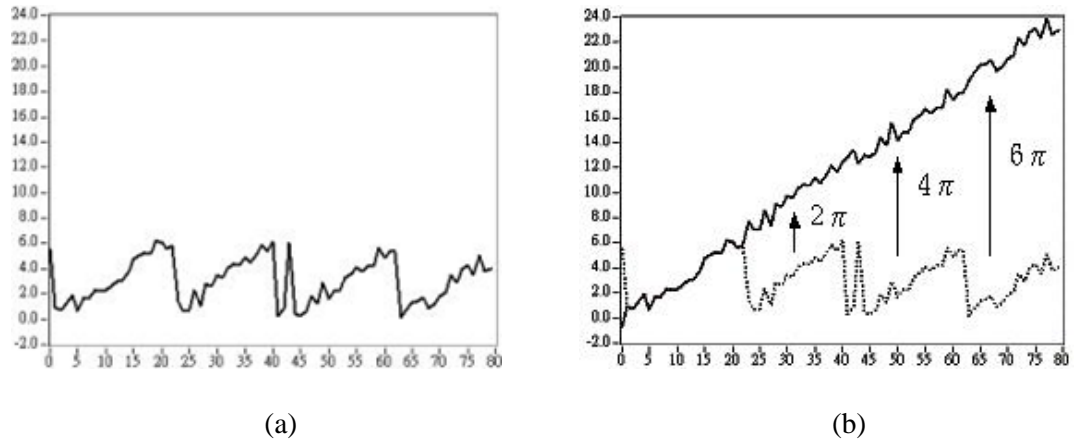
Figure 2-4 Unwrapping: (a) the original wrapped signal; (b) the result unwrapped signal.

2.3.1 Path-Dependent Phase Unwrapping

Path-dependent phase unwrapping was first proposed by Macy in 1983. The formula for it is written below:

$$\emptyset(x,y) = \int_C \left\{ \emptyset(x,y-1) + 2\pi Round\left[\frac{\emptyset(x,y) - \emptyset(x,y-1)}{2\pi}\right]\right\} dr \quad (2.22)$$

The principle of this method is to measure the phases in two neighbouring points in a pre-set path C. If the difference between them is larger than π, a period phase 2π is added to or subtracted from the phase of the processing

point. The process is shown in the following.
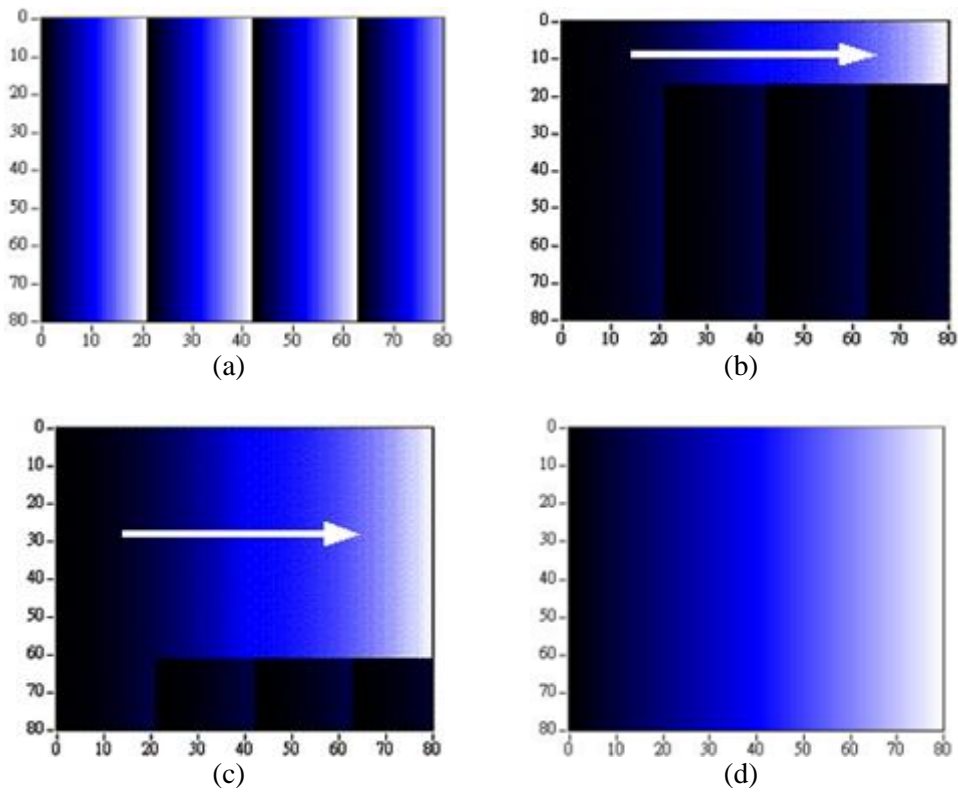
Figure 2-5 Phase unwrapping process: (a) wrapped phase, (b) unwrapping process from left to right, (c) unwrapping process from up to down, (d) unwrapped phase.

The simple structure of this method leads to its short processing time. However, performs poorly when dealing with the discontinuous points that are often produced by noises in the phase map. Points that have differences from adjacent points larger than 2π are referred to as discontinuities.
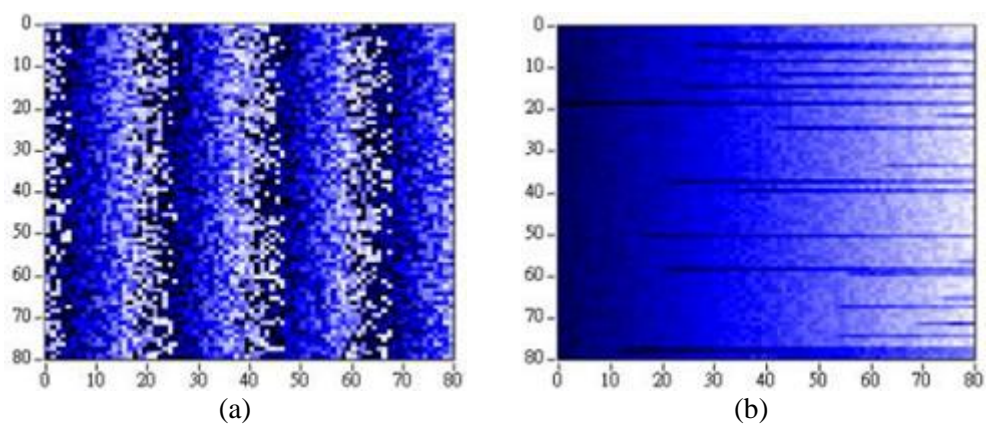
Figure 2-6 Process of reconstructing the signal with discontinuities: (a) signal with discontinuities; (b) result of unwrapped phase.

The path-dependent method is supposed to produce the error phase due to the discontinuities. Furthermore, the generated error phase is transmitted through all of the following points in the path, as shown in Figure 2-6.

Researchers have proposed methods to address the problem, including the minimum-spanning-tree method [76], the minimum-discontinuity method [77] and the priority-queue approach [78]. Most of these methods focus on how to determine a better pre-set path that can reduce the influence of discontinuities. For example, J. Feng introduced them to address the problem of height discontinuities in a recent publication [79]. Two robust filters (designated filters A and B) were proposed in their paper. Filter A comprises a noise-and-phase-jump detection scheme and an adaptive median filter; filter B replaces the detected noise with the median phase value of an N×N mask that is centred on the noisy pixel. With the proposed robust filters, three reconstruction paths are also proposed to provide a robust and accurate reconstruction performance.

2.3.2 Path-Independent Phase Unwrapping

The area of path-independent phase unwrapping has been studied extensively and various methods have been developed. Among the existing approaches, the cellular-automata phase unwrapping method (CA PhU) suggested by D.C Ghiglia in 1987 has been widely accepted by later researchers. This method is seen as typical of path-independent phase-unwrapping methods and it gains growing interest from researchers.

The steps of the mentioned approach can be concluded as follows:

Step 1 – Measuring phases with neighbours: The method processes each point in the phase map as base point P_0 in Figure 2-7 by measuring the differences between P_0 and the four neighbouring points.
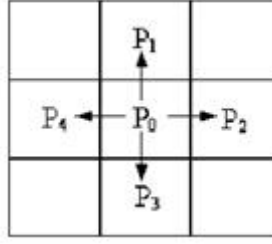
Figure 2-7 Comparisons with neighbour points

Step 2 – Calculation of the assigned weights: The original weights of the four neighbouring points are 0. The weight '+1' is assigned to the neighbour if the difference is larger than π, and the weight '-1' is assigned if the difference is smaller than - π. Assume that $p(x, y)$ represents the phase value of point (x, y). Then the sum of assigned weights can be written as follows:

$$sum = \sum_{ij} int \left[\frac{|p(x-i, y-j) - p(x,y)|}{\pi} \right] \left[\frac{|p(x-i, y-j) - p(x,y)|}{p(x-i, y-j) - p(i,j)} \right] \tag{2.23}$$

$$\begin{cases} i = 0, for\ j = 1, -1 \\ j = 0, for\ i = 1, -1 \end{cases}$$

Step 3 – Alteration of the phase of the base point: There are four cases for phase alterations according to the value of 'sum'. First, the typical CA PhU adds 2π to the phase of the base point with a positive 'sum'. On the other hand, second, if the 'sum' is negative, then the default method removes 2π from the phase. Third, No alteration is made to the phase if all the weights are of the original values, which should be 0. 4. If additional weights '+1' or '-1' are assigned, although the sum of those weights is 0, the default CA PhU adds 2π to the phase of the base point.

Step 4 – Iterations: The completion of processing the whole phase map using the method introduced in Step 1—Step 3—is called a *local iteration*. The completed 'local iteration' generates a newly revised phase map that is used as input to begin a new local iteration. The unwrapping framework repeats this process until it reaches a steady state in which two phase maps are periodic successively produced by the local iterations.

Step 5 – Decision of termination: The framework averages the two periodically occurring phase maps and then measures the differences of phase between adjacent points on the averaged map. This process is called a *global iteration*. The unwrapping process is completed if there is no phase difference larger than π or smaller than –π; otherwise, the framework enters the local iterations again with the averaged phase map.
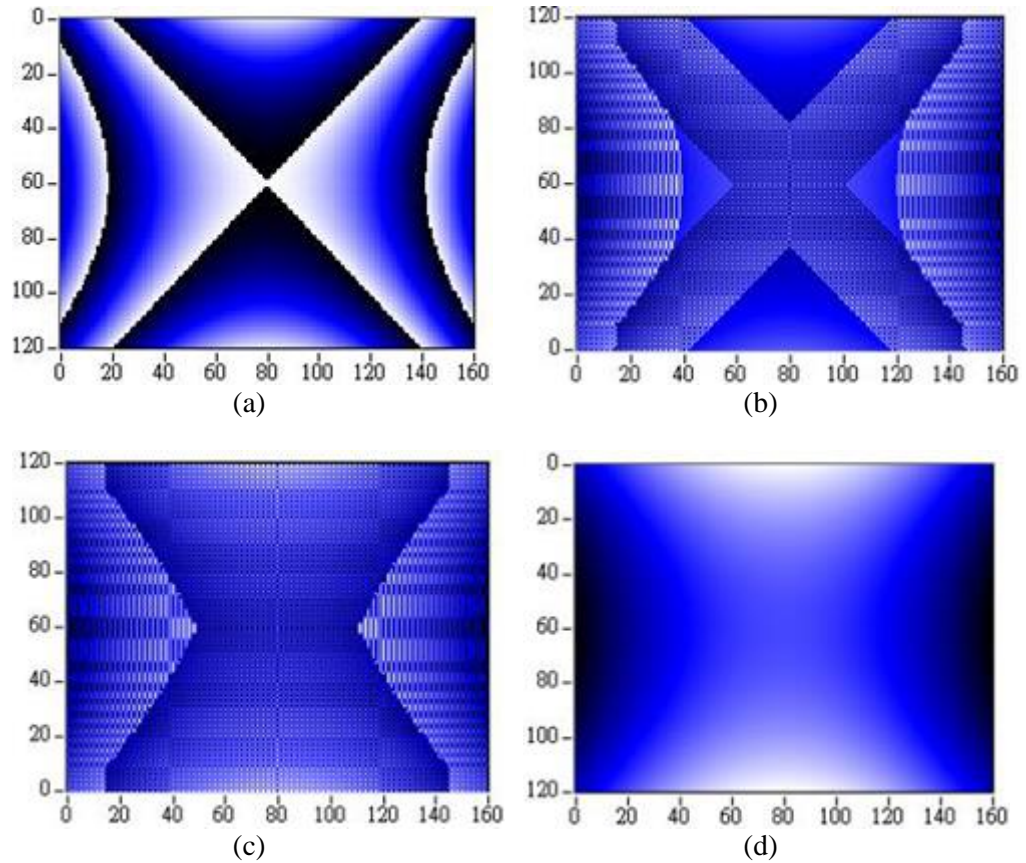
Figure 2-8 Process of CA PhU. (a) Wrapped Phase; (b) Result of 20 local iterations; (c) Result of 60 local iterations; (d) Unwrapped Phase

Default CA PhU is a parallel calculating method. This means that its performance is independent of the choice of paths. This factor enhances the robustness of its discontinuities in phase map. However, the large number of iterations results in a huge volume of computations that delays the response time of the framework and increases the requirements of the hardware employed for implementation. M.J. Huang proposes an improved parallel 2π phase-unwrapping method to overcome these drawbacks [80]. The method defines only one direction for the alteration of phase. Consider the low-to-high model, for example. The model defines only the addition operation that is

increasing 2π to the phase of the base point on condition that there is a difference of larger than π with the neighbours. In other words, the restriction of the direction for altering phase in this method dramatically reduces the number of potential calculations. New ideas have been introduced in more recent studies of path-independent phase unwrapping. For example, Y. Huang employed phase-derivative and total-variation (TV) to the path-independent phase-unwrapping approach to de-noise the wrapped-phase map obtained from a shearography experiment [81].

2.4 Conclusion

This chapter constitutes a study of several automated image-processing techniques: segmentation, visual tracking and 3-D phase reconstruction. The histories of development of these techniques and the relationships between them were presented. Typical models in each of the fields were introduced in detail, including thresholding, mathematic morphology (for the field of segmentation), the contour-evolution model (for the field of tracking techniques) and variant approaches for the field of phase reconstruction.

To establish a robust and powerful automated cell-monitoring system, the performances of these techniques are of pivotal importance. Therefore, this study analyses the advantages and drawbacks of existing approaches that provides directions of further improvements and also forms the foundation of the research presented in this thesis. The following chapter, Chapter 3, introduces a novel segmentation method designed exclusively for cell images and presents a case study of feature measurements by using the real cell datasets captured by the University of Nottingham, United Kingdom.

Chapter 3   Cell Features Measurement

3.1 Introduction

The primary morphological features of cells include length and width, size, volume and adhesion area. Analysis of these features of cells in different environments is essential to the study of various biological processes. Y. R. Chang proved that it is important to observe morphological changes of blood cells in clinical diagnoses [82]. X. M. Cheng analysed samples of marrow cells and suggested that observation of their shapes can provide pivotal help in the treatment of certain diseases [83]. Some monitoring frameworks of cell features have already been established. For example, Nano Analytics invented a cell-monitoring system called cellZscope that makes it possible to observe cells living in up to 24 different cultures [84]. In recent studies, T. A. Zangle suggested a quantification process of biomass and cell motion in human pluripotent stem-cell (PSC) colonies [85]. Zangle's study investigates the working mechanism of proliferation and biomass control with early events in the differentiation of PSCs—another great application of quantification monitoring in biology [85]. However, core problems are shared by the

applications: i.e., the accuracy of feature measurement in the frameworks is often low, and few of the systems are entirely automated. Therefore, cell-feature measurements and the revision of the generated results require enormous manual labour. Faults caused by human eyes are inevitable in this manual approach due to the high density of cells and the low quality of cell images. These factors form the driving force behind the development of an automated method that can provide accurate measurements of cell features.

Cells have 1-D features, such as length and width, 2-D features, such as size and adhesion area, and 3-D features, such as cell volume. Different approaches are used to measure the features in each dimension. 1-D and 2-D features are measured from the binary maps of cell images that are generated by the segmentation method, and the 3-D features can be measured from the 3-D model of cells established by 3-D reconstruction. Hence, segmentation and 3-D reconstruction are core components in the process of cell feature measurement.

This chapter introduces a newly designed segmentation method that can accurately segment cell images and accurately detect cell antennae. This method and its variants are used to segment real cell datasets captured by the University of Nottingham, United Kingdom (UNUK). An evaluation of the performance of the proposed method and of existing widely-used approaches is then presented. Features of the cells contained in the datasets are measured using the defined methods, and the generated measurements are analysed.

3.2 The framework of cell segmentation

Image segmentation techniques aim to disjoin target objects from their background areas. Image segmentation is an essential step in many computer-aided processes, such as pattern recognition; thus, many studies have focused on improving the accuracy of segmentation. Image segmentation techniques such as thresholding and watershed are widely used in biological applications. The driving force behind the design of a new segmentation approach is the need for detections of cell filopodia. Cell filopodia can provide

useful information in many biological analyses [86]; however, most existing segmentation techniques have a hard time detecting them accurately. Hence, a novel segmentation approach that is based on local and global thresholding techniques is designed to address the problem.

3.2.1 Overview of framework

The principle of the thresholding technique is to classify the pixels into separate groups that depend on their threshold value. According to the means-to-decide threshold, thresholding techniques can be separated to two categories: local thresholding and global thresholding. Assume that $f(x,y)$ represents the grey values of the whole image, and that $p(x,y)$ represents the grey values of the points that surround (x,y). The ways of deciding the value of threshold can be expressed as follows [15]:

$$T = T[x, y, f(x, y), p(x, y)] \tag{3.1}$$

The technique is called global thresholding for the situation in which T is decided only by $f(x,y)$. The structure of this approach is simple; thus, it has an excellent processing speed. However, because little spatial information is taken into account in the global-thresholding approach, the technique is extremely sensitive to noise and provides acceptable performance only for images with little content and uniform distribution of grey scales. The local thresholding technique determines the threshold value T relative to $p(x,y)$ only. In other words, the values of threshold vary for different positions in the image, which reduces the influence of the non-uniform distribution of grey scales. Although the local-thresholding approach addresses the drawback of global thresholding, it results in another issue: due to the lack of a comprehensive view of the topology of the image, the technique may fragmentarily detect its targets. Therefore, these two techniques—local and global thresholding—are combined in the framework of a new segmentation approach to yield better performances. The structure of the framework is organized as follows:
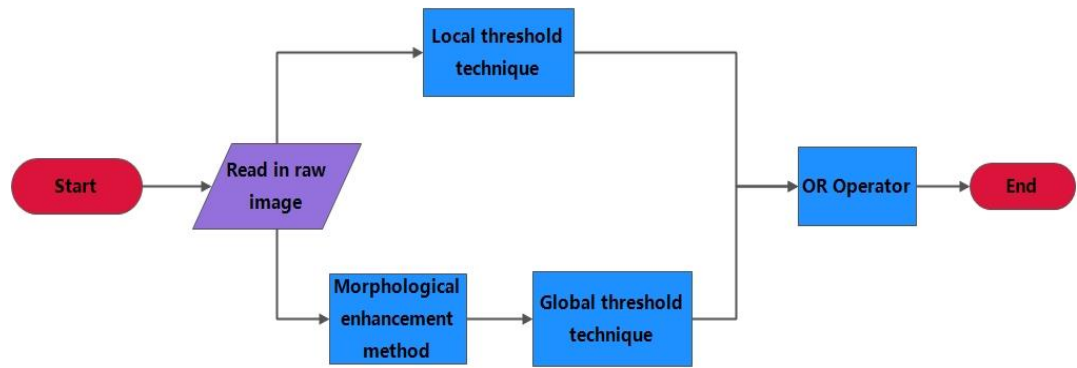
The raw image is first processed by local and global thresholding techniques. The two generated binary maps then go through the logical 'OR' operator to produce the final segmentation result. Details of the two core techniques, local and global thresholding, are presented in what follows.

3.2.2 Local-thresholding technique

The local-thresholding technique is primarily employed to recognize detailed information—such as information about cell filopodia. Therefore, the newly designed segmentation approach outperforms existing methods. The process of implementing the local-thresholding technique is presented as follows:

Step 1 – Generation of sub-images: The local thresholding method separates an image into several sub-images. The number of sub-images depends on the size of original image. For example, if the sample image is 2048×2048, it can be divided into 16 512×512 sub-images that exhibit uniform greyscale distribution and contain less content.

Step 2 – Generation of threshold matrix: The Otsu thresholding method [10] is used to generate thresholds for each of the separated sub-images. The matrix of thresholds is formed by placing the generated thresholds in positions that correspond to the sub-images, as shown in Figure 3-2.

$$
\begin{array}{cccc}
T_{11} & T_{12} & T_{13} & T_{14} \\
T_{21} & T_{22} & T_{23} & T_{24} \\
T_{31} & T_{32} & T_{33} & T_{34} \\
T_{41} & T_{42} & T_{43} & T_{44}
\end{array}
$$

Figure 3-2 Threshold matrix

Next, the threshold matrix is linearly interpolated to the size of original cell image.

Step 3 – Thresholding: The threshold matrix is scaled to the size of the original image via interpolation. The local-thresholding approach then compares the original image with the generated threshold matrix image on a pixel-by-pixel basis. Points larger than the corresponding threshold are labelled as one group and the other points are classified to another group. A binary map of the original image is then produced.

Although the detailed information of cells, such as the filopodia, can be efficiently extracted using the local-thresholding technique, the main bodies of objects are usually detected in fragmentation. Thus, the global thresholding technique is introduced in the framework to address this fragment issue caused by the local-thresholding approach.

3.2.3 Global thresholding technique

Global thresholding is one widely used segmentation approach. Due to its simple algorithm structure, global thresholding is very easy to implement. However, since it uses the same threshold to segment the whole image, a non-uniform distribution of greyscales of cell images may cause errors: e.g., cells of low contrast may be missed. Thus, the method described in [87] is used to enhance the quality of cell images. It uses morphological transforms, top hat and bottom hat, to extract the bright field and dark field in the image. If *f* is a grayscale image and *b(x)* is a grayscale structuring element (e.g., a 5x5 square matrix), then top-hat and bottom-hat transforms are represented as follows:

$$T_{top-hat} = f - f \circ b \tag{3.2}$$

where $\circ$ denotes an opening operation. This opening operation can be defined as $A \circ B = \cup_{B_x \subseteq A} B_x$, which means that it is the locus of the translations of the structuring element B inside the image A:

$$T_{bottom-hat} = f \bullet b - f \tag{3.3}$$

where $\bullet$ is the closing operation that can be obtained by $A \cdot B = (A^c \circ B^s)^c$, X^c denotes the complement of X relative to E (that is, $X^c = \{x \in E | x \notin X\}$) and B^s denotes the symmetric of B, that is, $B^s = \{x \in E | -x \in B\}$. Here, E is a Euclidean space.

The above means that the closing is the complement of the locus of translations of the symmetric of the structuring element outside the image A.

To increase contrast, the approach processes these two fields back to the original image, as shown in (3.4).

$$f_{enhanced} = f + \frac{T_{top-hat}}{2} - \frac{T_{bottom-hat}}{2} \tag{3.4}$$

The threshold for the enhanced cell image is decided by the Otsu method, which is established from the idea of measuring the between-class variance. Differentiated from the local-based approach, the value of threshold is unified for the entire image in the global-thresholding technique.

3.2.4 Performance evaluation

3.2.4.1 Experimental results

The microscopic images of progenitor neural cells captured by the iBIOS team from the University of Nottingham, United Kingdom (UNUK) are used as sample images to demonstrate the proposed segmentation approach. One example experimental result from each phase of the proposed method is presented in Figure 3-3. Figure 3-3 (c) shows the segmentation results generated by the local-thresholding technique. Figure 3-3 (d) shows the result

of global thresholding. The shortcomings of these two components can be observed from the results: fragmentation occurred in the local technique, and detail detection is poor in the global approach. Compared to the results produced by each individual technique, the final segmentation result (Figure 3-3 (e)) reflects an improvement provided by the hybrid method. Figure 3-3 (f) shows the original cell image (Figure 3-3 (a)) marked with the detected cell profiles, which are in black.
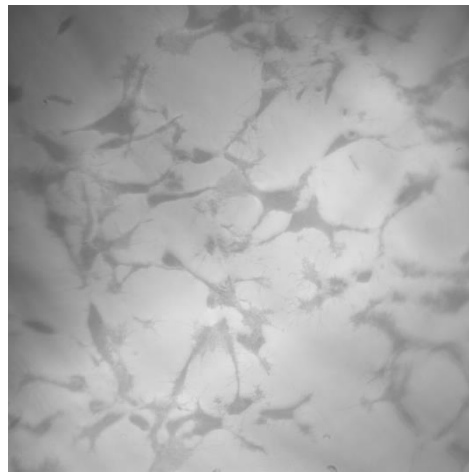
(a)
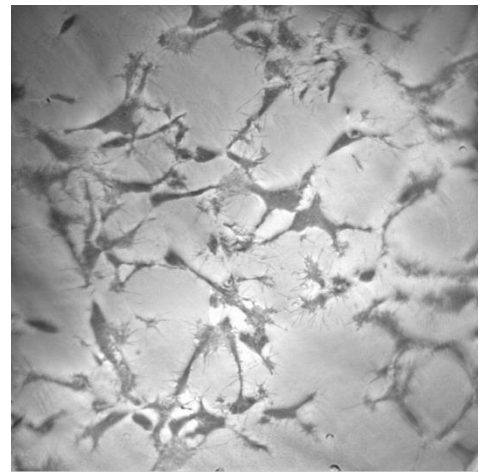
(b)
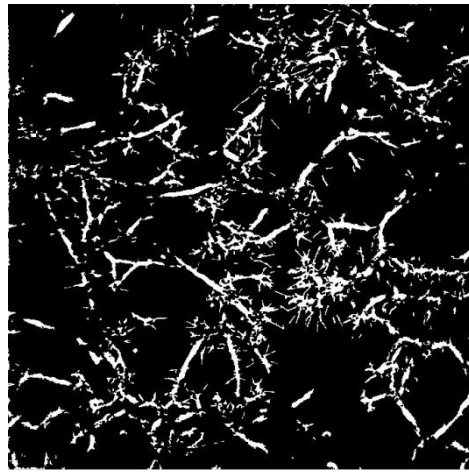
(c)
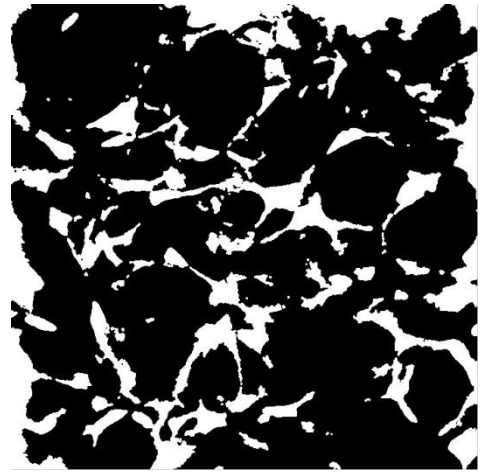
(d)

(e)
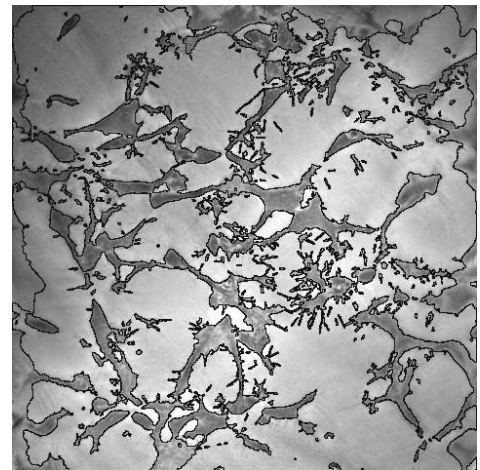
(f)

Figure 3-3 Example experimental results: (a) the original cell image, (b) the enhanced cell image, (c) result of local thresholding, (d) result of global thresholding, (e) final result, (f) cell image with cell profiles.

(a)

(b)

(c)

(d)
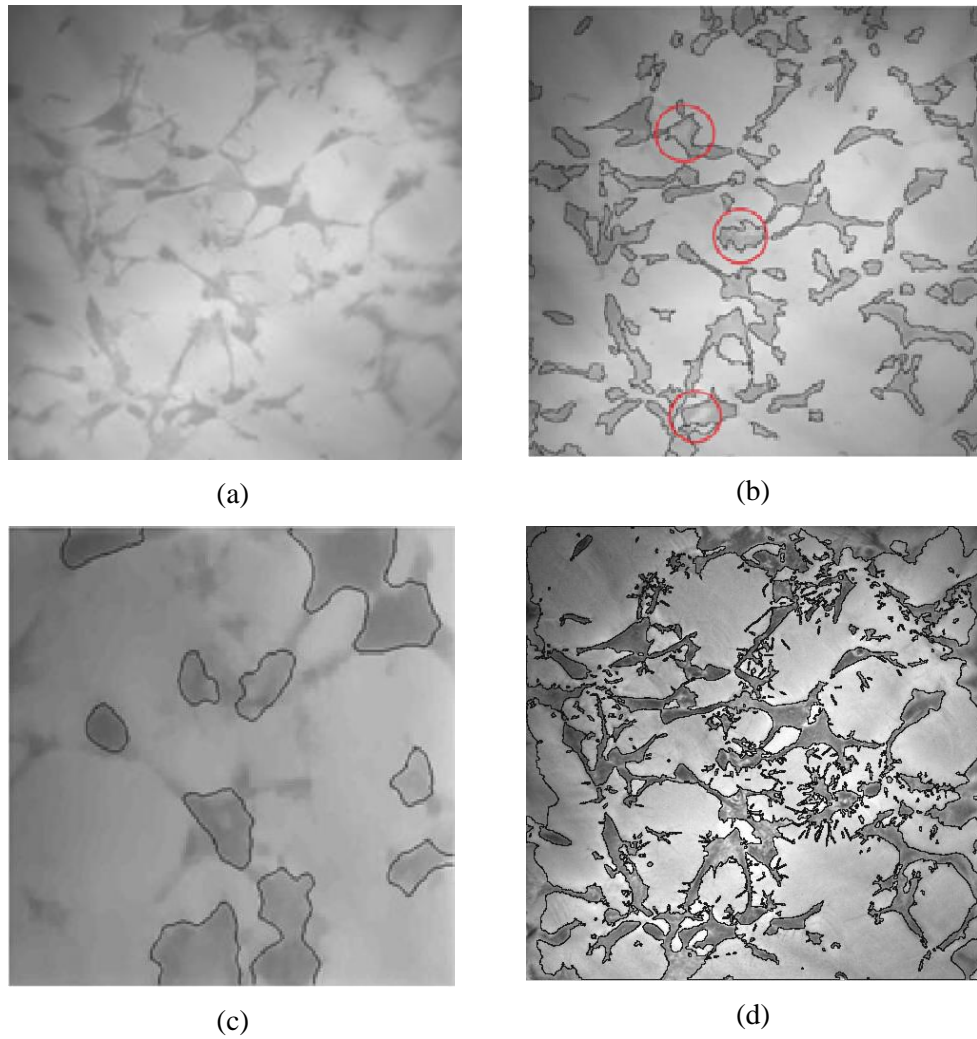
Figure 3-4 Segmentation outcomes: (a) original image; (b) result from watershed. The red circle indicates the segmentation error. (c) Result from level set; (d) result from the proposed segmentation method.

To further demonstrate the improvement of segmentation accuracy from the proposed approach, it is compared with typical segmentation methods, including watershed, 2-D thresholding and level-set methods. The outcomes are presented in Figure 3-4. Due to the non-uniform distribution of grayscales, errors occurred in the results of the watershed (Figure 3-4 (b)) and 2-D thresholding (Figure 3-4 (c)), which have been marked with red circles. The level-set approach requires a large workload of computations; therefore, the sample has been reduced to a narrow view. However, because of the low image contrast, the level-set based segmentation also fails to perform an accurate segmentation. Large cell areas are missed in its segmentation result

(Figure 3-4 (d)).

Furthermore, the results provide no detection of detailed information, such as information about the cell filopodia (Figure 3-4 (b-d)). This reflects the fact that the popular algorithms are unable to detect details. Figure 3-4 e) shows the result of the proposed segmentation framework that is based on hybrid thresholding techniques. The proposed approach performs well in the recognition of cells and cell filopodia and refines the faults labelled in the other results. The performance of the newly proposed framework can be expected from these preliminary comparison studies.

However, since the ground truths of segmentation of this dataset are not generated by the iBIOS team, it is difficult to quantitatively evaluate the segmentation performance of the proposed approach with this dataset. Hence, a published time-lapse microscopic dataset is employed to provide the quantitative evaluation.

3.2.4.2 Segmentation accuracy

A. Introduction of dataset

The dataset records the moves of rat mesenchymal stem cells (MSC) on a flat polyacrylamide substrate. It was captured by Dr. F. Prosper of the cell-therapy laboratory at the Center for Applied Medical Research (CIMA) in Pamplona, Spain. Detailed information is listed below.

Table 3-1 Detailed information of MSC dataset

	Sequence No.	Image Size	No. of Frames	Total No. of Cells
Rat mesenchymal stem cells (MSC)	1	992×832	48	15
	2	1200×782	48	10

Because the shapes of the MSC cells are close to those of the progenitor neural cells, most of which are long and slim, this published dataset is used to evaluate the segmentation accuracy of the proposed approach. Images from the dataset are shown as examples in Figure 3-5.
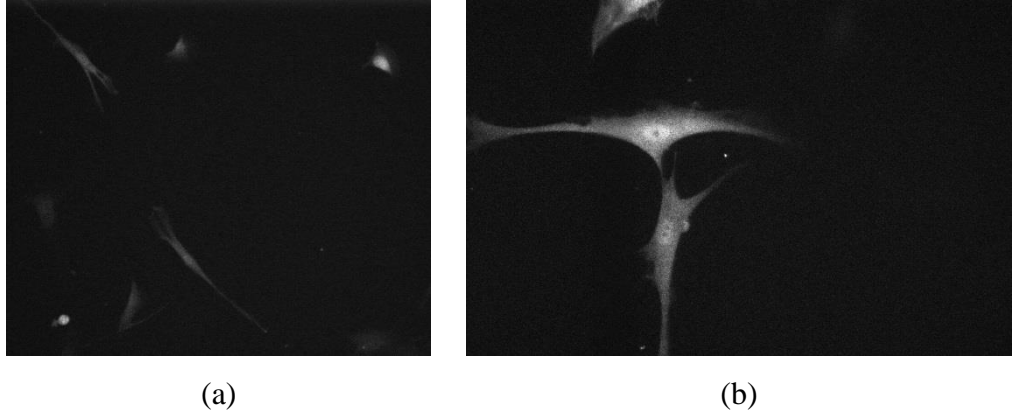
Figure 3-5 Images from Spain MSC dataset: (a) sample image from sequence#1, (b) sample image from sequence#2.

The segmented ground truths of the dataset are provided by the experts. The accuracy of the segmentation approach can therefore be measured based on the Jaccard similarity index (J) of the sets of pixels of matching objects:

$$J(S, R) = \frac{|R \cap S|}{|R \cup S|},$$

where R denotes the set of pixels that belong to a reference object and S denotes the set of pixels that belong to its matching segmented object. A ground truth object, *R*, and a segmented object, *S*, are considered to match if and only if the following condition holds:

$$|R \cap S| > 0.5|R|$$

The J index is calculated for each reference object in a video. It varies between [0 1], where *1* represents perfect match and *0* represents no match.

The segmentation measure (**SEG**) is computed by the mean of J indices of all reference objects in a particular video.

B. Evaluation with benchmark algorithms

Typical segmentation approaches—including watershed, global Otsu, local Otsu, global Fuzzy-entropy thresholding and local Fuzzy-entropy thresholding—are tested by using the MSC datasets as benchmark methods. A segmentation method based on level set is also implemented. It was found not to work with the datasets. The segmentation accuracies (SEG) of the proposed

approach and the benchmark algorithms are listed in Table 3-2.

Table 3-2 Comparison of SEG (%)

Sequence No.	MSC		
	1	2	Average
Watershed	27.98	19.66	23.82
Global Otsu	32.67	47.94	40.31
Local Otsu	31.12	44.65	37.89
Global Fuzzy-entropy	36.47	49.75	43.11
Local Fuzzy-entropy	40.52	39.85	40.19
Proposed Method	**43.03**	**56.29**	**49.66**

From the table, the typical watershed approach yields the lowest SEG, i.e., 23.82%, among the presented approaches. The global and local-thresholding techniques using Otsu and fuzzy entropy produce close segmentation accuracies: i.e., 40.31% and 43.11% for the global Otsu and fuzzy entropy, and 37.89% and 40.19% for local thresholding using Otsu and fuzzy entropy. Overall, the frameworks that use fuzzy-entropy provide more accurate segmentation results than the ones using Otsu. Our proposed segmentation approach achieves a SEG of 49.66%, which is better than that of the typical segmentation algorithms presented.

3.3 Specification of cells' features

Features of cells, such as size and shape, often provide important information in biological applications. Because of a lack of proper processing techniques, it can be a laborious task to measure these features. As a consequence of the development of image-segmentation techniques, measurement is becoming automated in recent researches. Cell size and cell shape are the primary cell features for extensive analyses. Each is briefly introduced, and the measurement methods are presented in this section.

3.3.1 Introduction of different cell images

The images used in the experiment were captured by the biology science team from the University of Nottingham, United Kingdom. There are 33 sets of images of neural progenitor cells in the database that record the results of

turning off CO_2 supply. The time interval for sampling is 11 days, and 3 sets of samples are captured each day. Each set contains two kinds of images that are captured by the total-internal-reflection microscope (TIRM) and phase-contrast microscope. An advanced microscope has been built by the team that can simultaneously produce these two kinds of images.
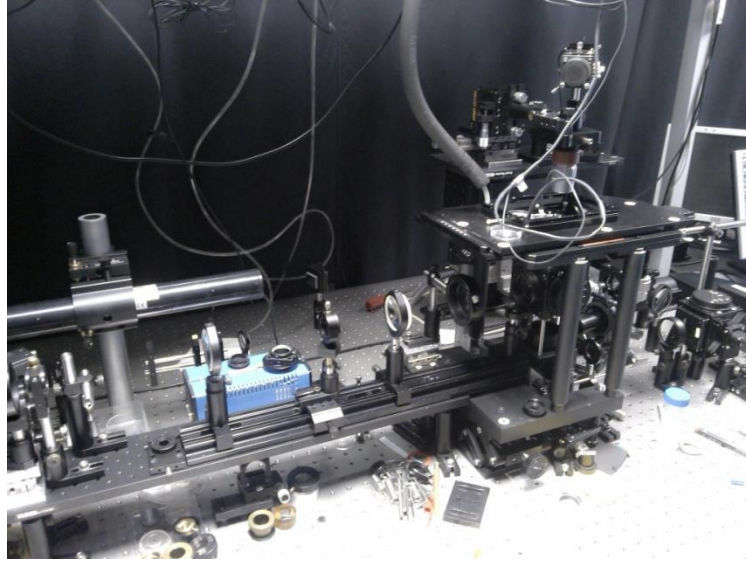
Figure 3-6 Image of an home-built advanced microscope in the University of Nottingham UK

Samples of these two kinds of images are shown in Figure 3-7. The difference between them is the direction of observation. The TIRM observes the cells from the bottom of the object slide; hence, the cell areas in the TIRM image are also called cell-adhesion areas. The phase-contrast microscope observes the cells in the opposite direction, i.e., from up to down, thus the areas of cells in the phase contrast images are the real sizes of cells.

(a) (b)
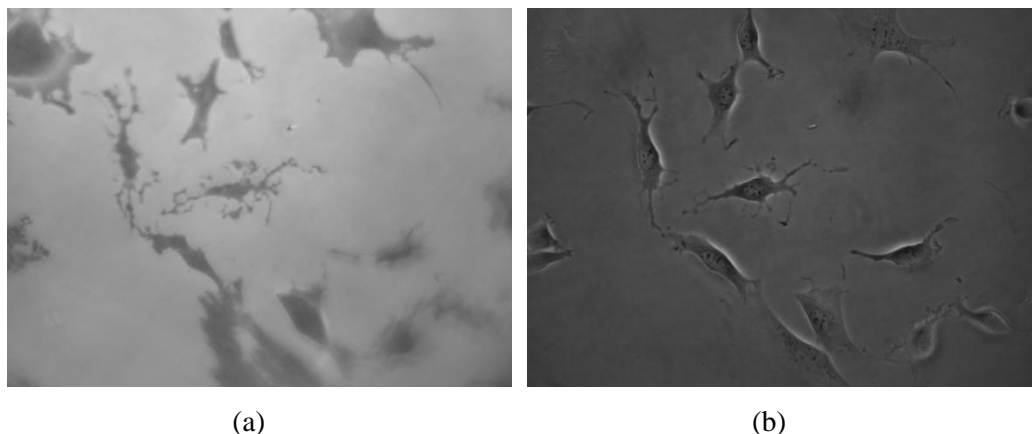
Figure 3-7 sample images from iBIOS team. (a) TIRM image; (b) Phase image (with $3\pi/2$).

The detailed information of the dataset is listed below.

Table 3-3 Detailed information of the dataset

Image Types			Number of Samples	Frame size
TIRM image	Narrow field			1392×1040
	Wide field			1600×1200
Phase image	Narrow field	Phase of 0	33	1392×1040
		Phase of $\pi/2$		
		Phase of π		
		Phase of $3\pi/2$		
	Wide field	Phase of 0		1600×1200
		Phase of $\pi/2$		
		Phase of π		
		Phase of $3\pi/2$		

3.3.2 Methodology for feature measures

Using the captured cell images, various features of cells—such as cell area, cell volume and cell shape—can be measured quantitatively with defined approaches.

3.3.2.1 Cell Area

In 2D space, the primary measurement of cell size is the cell area detected in the input images. To measure cell area, the original cell images are first transformed into a binary map using segmentation techniques. Then the area is calculated by accumulating the markers the represent the same cell. Consequently, the performance of image segmentation is of pivotal importance for the calculation of cell areas. The newly designed segmentation method and several famous segmentation approaches—such as watershed and level-set—are tested with the experimental datasets. An evaluation of their performances is provided to determine their ability to deal with real cell datasets.

3.3.2.2 Cell Volume

In 3D space, cell volume is the main measure of cell size. Two parameters are often used to calculate cell volume: cell area and cell thickness. Cell area is measured with the segmentation technique; thus, the aim of the task is to accurately measure the thickness of cells by reconstructing the 3-D model of cells. Therefore, 3-D reconstruction is the core technique for the calculation of cell volume.

Using the phase images captured by phase-contrast microscopy, a wrapped-phase map can be generated. Phase-contrast microscopy is an optical microscopy technique that converts phase shifts in light that passes through a transparent specimen into brightness changes in the image. Phase shifts are invisible; but they become visible when shown as brightness variations. The structure of the microscope is shown in Figure 3-8. The phase ring in the microscope is used to change the phase.
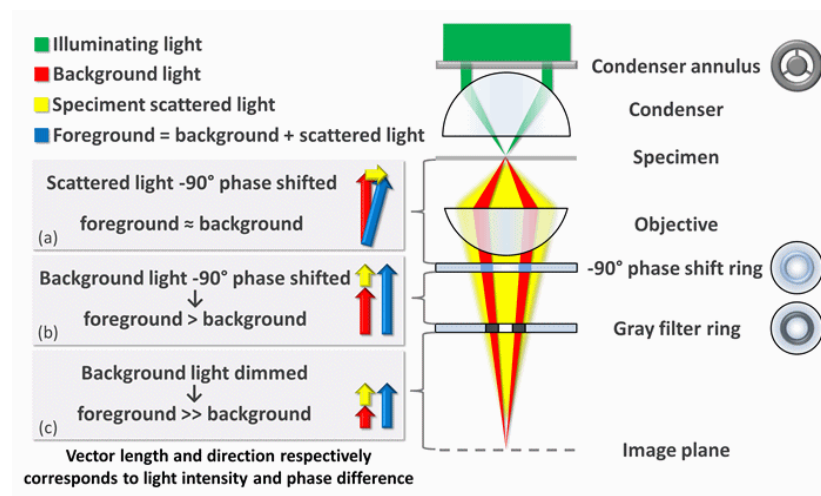
Figure 3-8 Phase Contrast Microscopy

Four images in phases of 0 (Figure 3-9 (a)), $\pi/2$ (Figure 3-9 (b)), π (Figure 3-9 (c)), and $3\pi/2$ (Figure 3-9 (d)) are needed to produce the phase map. The sample of each phase is shown below.

(a)

(b)

(c)

(d)
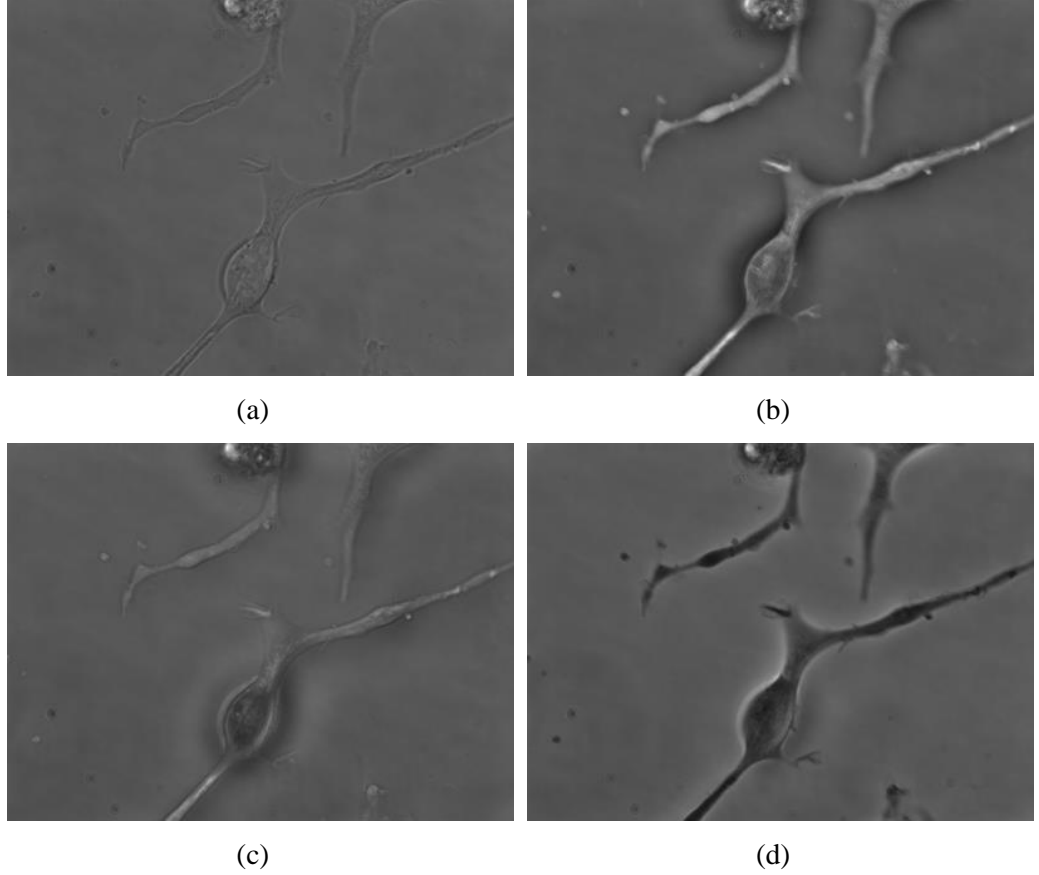
Figure 3-9 Samples of phase images: (a) image of 0 phase, (b) image of $\pi/2$ phase, (c) image of π phase, and (d) image in $3\pi/2$ phase.

With the four phase images, the phase map can be produced by the following formula:

$$\text{Phase} = \frac{I_{3\pi/2} - I_{\pi/2}}{I_{\pi} - I_0} \qquad (3.5)$$

The preliminary phase map from the formula is wrapped. A path-dependent phase-unwrapping technique is employed to resolve the wrapped-phase map. A 3-D view of cells can be established with the unwrapped-phase map.

3.3.2.3 Cell Shape

Cell shapes can vary widely; for example, rat mesenchymal stem cells are long and slim while mouse stem cells are circular. As a result, the appropriate characteristic for shape measuring varies with the shape of the targets. The designed system uses three general parameters to represent the morphology of a cell: length, width and roundness. The input for this process is also the binary map. The system applies the minimum convex polygon that contains the cell to determine the length and width; the roundness is computed by a pre-built function in the software.

| (a) | (b) |
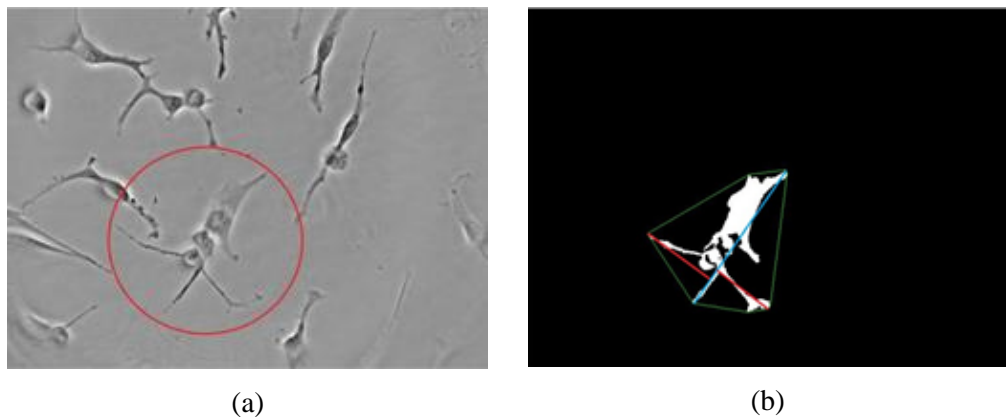
Figure 3-10 Morphology measurements: (a) the image with the target cell, (b) the binary map of the circled cell. In (b), the green outline is the minimum convex polygon, the blue line is the length, and the red lines are the width.

The first step to calculate the two features is to draw the minimum convex polygon encircling the cell, as in the green convex marked in Figure 3-10 (b). Then, the distance between each pair of edge points is measured and the longest one is recorded as the length of the cell, like the blue line shown. With the blue line, the cell is separated into two parts. For each side, the longest distance from the edge point to the blue line is calculated, and the width is the sum of the two longest lines in different sides (the red lines).

3.4 Experimental results and analysis

The automatic cell-monitoring framework is applied to a real cell dataset captured by University of Nottingham, United Kingdom as a case study. This is done to demonstrate the excellent cell-feature measurement provided by the

designed framework. The system can automatically and very accurately extract features such as cell size and cell shape. Furthermore, the system measures the cell from both 2-D and 3-D views to produce a comprehensive view for the observation of alterations in cell features. In this section, experimental results are presented followed by an analysis of the performances of the employed methods.

3.4.1 Cell Area

Neural progenitor cells are taken as specimens in experiments that investigate the mechanism of the neural progenitor cells in an environment without CO_2 supply. Researchers from the iBIOS team predicted the variations of cell areas in two kinds of cell images, as shown in Figure 3-11. The blue line describes the variations of cell area observed from the phase microscope; the green and red lines represent variations of cell areas in the TIR microscope. Theoretically, living neural progenitor cells adhere to the bottom of the slice that can be observed from the TIRM image. The specimen cells gradually die as the volume of CO_2 reduces in their environment. They stop attaching to the bottom and go up to the surface of the slice after they die, as can be observed from the phase images. Therefore, the population of dead cells can be monitored by comparing the cell areas in these two images. A prediction was made by the Bio-Science team from University of Nottingham.
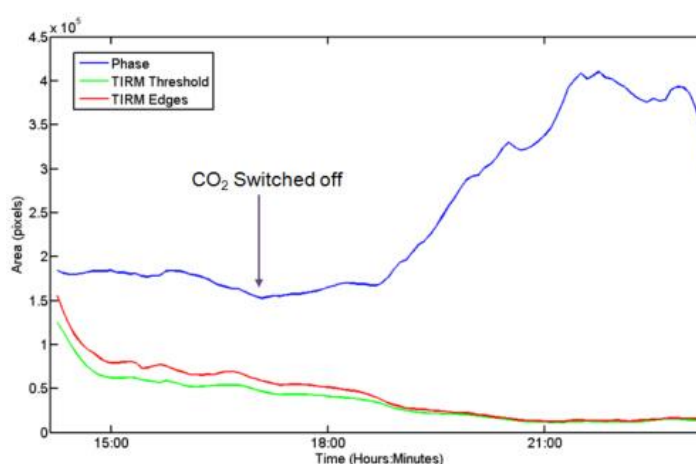
Figure 3-11 Prediction of changes in cell areas

(a)　　　　　　　　　　　　　　　(b)

(c)　　　　　　　　　　　　　　　(d)

(e)
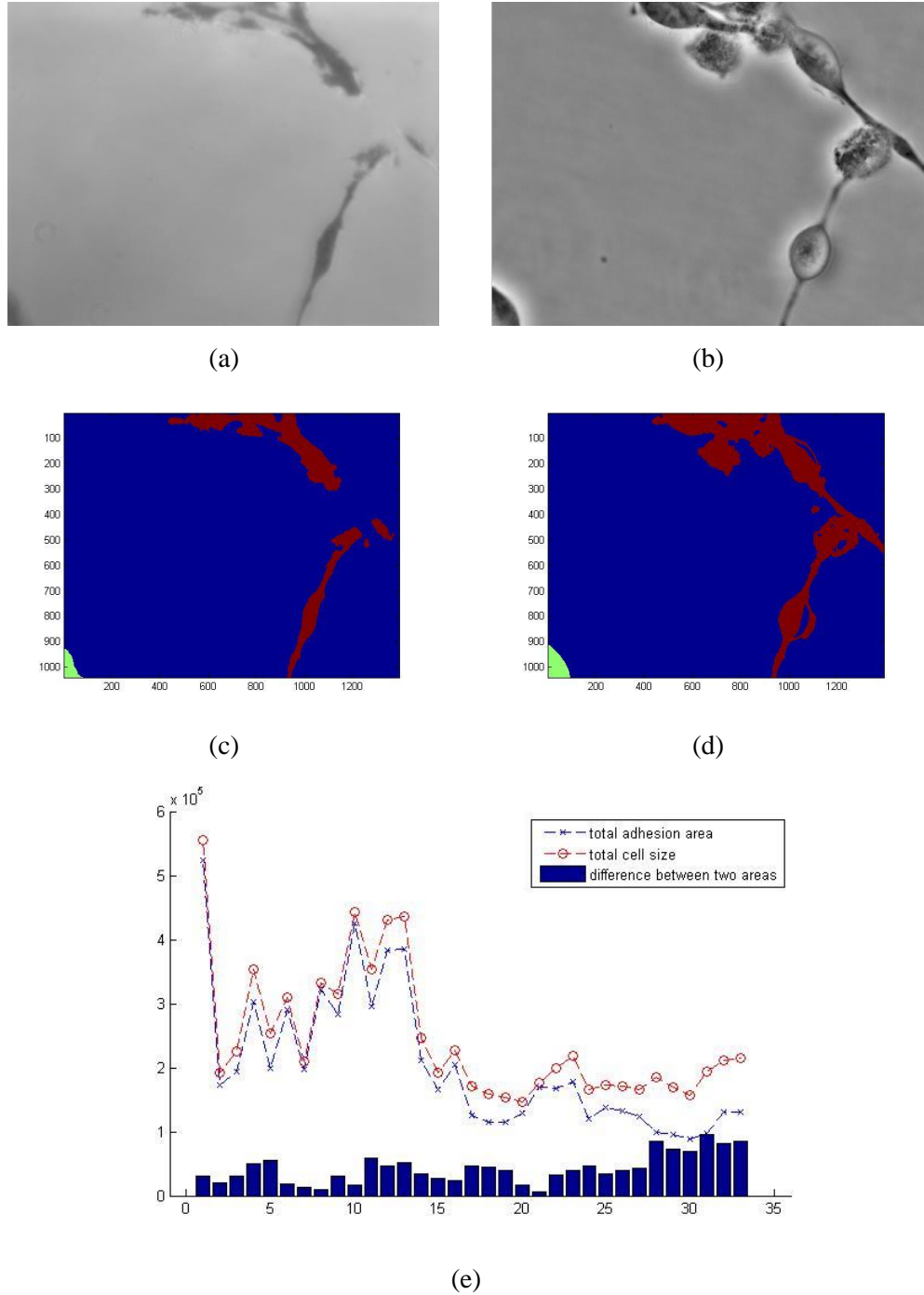
Figure 3-12 Outcomes in the experiment: (a) TIRM image (frame #30), (b) generated phase map (frame #30), (c) segmentation result of TIRM, (d) segmentation result of phase map, (e) changes of the two areas through 33 frames

To analyse the captured real-cell datasets, our proposed segmentation algorithm is employed to segment the cell images. With the segmentation result, the cells are marked with different labels and their areas can be measured. In the experiment, two parameters—adhesion area in the TIRM image and cell size in the phase map from Eq. (3.5)—are calculated and

compared to see if the reality is consistent with the prediction. The narrow field images are tested and shown in Figure 3-12 (a-d) for easy observation.

Figure 3-12 (e) shows an abnormal climb up in both adhesion area and cell size from frame #1 to frame #14. This occurred because of some unstable variations in the cell environment. Therefore, the observation point was switched to a new area. The data from frame #15 to frame #33 is thus valid for analysis. The differences between these two measures increased after CO_2 supply was stopped, which means that cells leave the bottom and rise to the surface. In other words, cells gradually die if there is no CO_2 in their living space. This finding is consistent with the prediction made before experiments (Figure 3-11).

3.4.2 Cell Volume

Since volume is a 3-D parameter, the 3-D view of cells should first be built to calculate it. Using the phase images, a wrapped phase map can be produced. Information about cell thickness is encoded in the phase map. A path-dependent unwrapping approach is employed to resolve the phases. The reconstructed 3-D view of cells that uses the phases resolved by the path-dependent approach is presented below.

Figure 3-13 (c) shows an example of a 3-D reconstruction of the phase map shown in Figure 3-13 (b). The colour bar in Figure 3-13 (c) is used to measure the thickness of cells. Different colours in the 3-D reconstruction can be transformed to their corresponding heights. By comparing figures Figure 3-13 (a) and (b), unexpected noisy phases are found to be generated around the cell areas in Figure 3-13 (b). These noisy phases are also reconstructed in the 3-D model of Figure 3-13 (c).
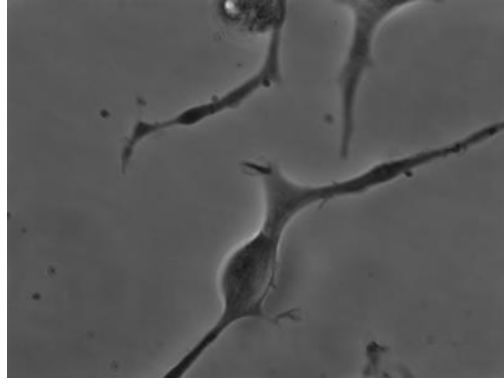
(a)
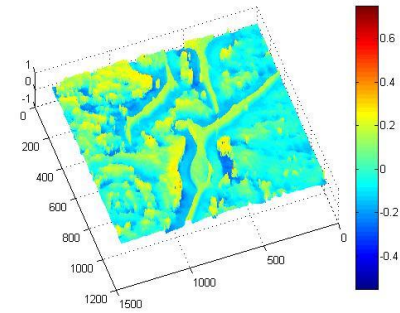
(b)   (c)

Figure 3-13 3-D Reconstruction using the unwrapping method: (a) the dark field image (phase of 3π/2) (b) generated phase map, and (c) 3D reconstruction.

Therefore, to suppress the influence of noise, the image in the phase of $3\pi/2$, also called dark-field image Figure 3-13 (a), is used to distinguish the areas of cells in the 3-D reconstruction. The framework first extracts the cell areas by segmenting the dark field-cell image. It then revises the unwrapped phase image by assigning small weights to the areas around cells to suppress the noise in the background. The revised result is compared with the original phase map in Figure 3-14. Most of the noisy phases in the original reconstruction (Figure 3-14 (a)) have been removed from the revised reconstruction (Figure 3-14 (b)).
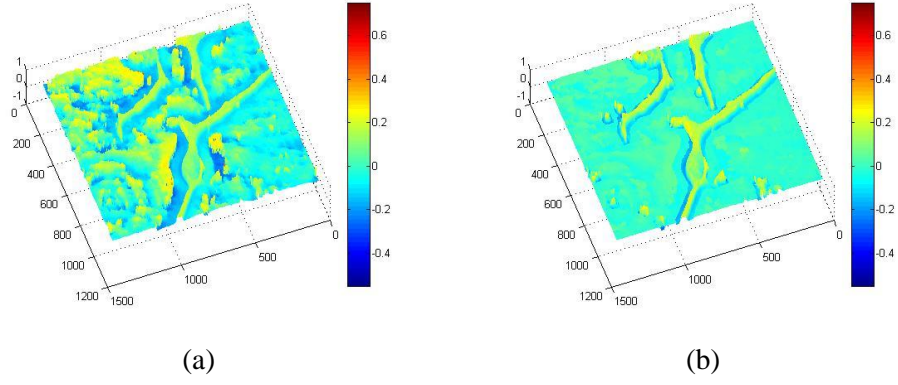
Figure 3-14 Comparison between unwrapping methods: (a) original phase map, (b) phase map with noise suppressions.

The phase-unwrapping technique is rarely applied to microscopic images. In recent research, G. Popescu proposed a method called PSI that rebuilds the 3-D view of cell images exclusively [88]. The phase distribution associated with the microscope image is retrieved by the following:

$$\emptyset(x,y) = \tan^{-1}\{\frac{\beta(x,y)\sin[\Delta\emptyset(x,y)]}{1+\beta(x,y)\cos[\Delta\emptyset(x,y)]}\} \tag{3.6}$$

with

$$\tan(\Delta\emptyset) = \frac{I_{3\pi/2} - I_{\pi/2}}{I_\pi - I_0} \tag{3.7}$$

and

$$\beta(x,y) = \gamma\frac{[I_0 - I_\pi + I_{\frac{3\pi}{2}} - I_{\frac{\pi}{2}}]}{\sin[\Delta\emptyset(x,y)] + cos[\Delta\emptyset(x,y)]} \tag{3.8}$$

where $\gamma = \frac{|E_0|^2}{4}$ and E_0 is the uniform field in the image plane.

The result of the PSI provides more information about the details of phases than the general path-dependent unwrapping method, as can be observed from the below figures.
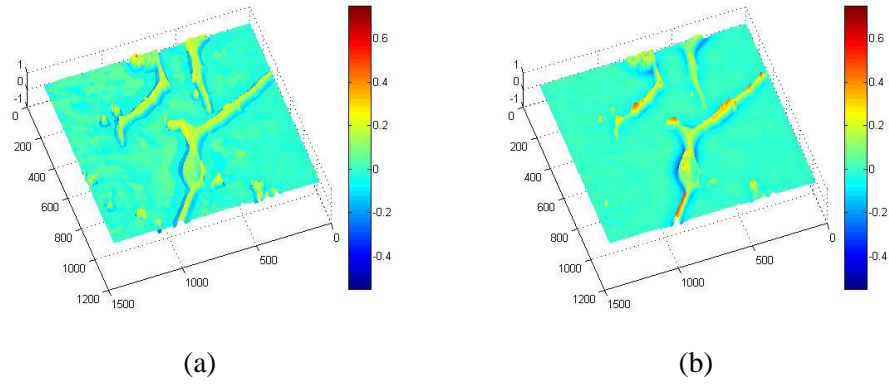
Figure 3-15 Results comparison: (a) result from general unwrapping method, (b) result from PSI.

Compared to the general path-dependent method (Figure 3-15 (a)), the thickness of cells reconstructed by PSI (Figure 3-15 (b)) varies in a wider range. This wide variance can be observed by comparing the variations of colours of the two 3-D reconstructions. In other words, loss of detailed information is found in the result generated by the general path-dependent unwrapping approach. This situation is produced as a result of the relationship between the wavelength of light and the size of the target used for reconstruction. The general path-dependent method is used to build a 3-D view of macroscopic objects that are larger than the wavelength of light. The situation shifts with respect to microscopic objects such as cells. The diameter of thrombocyte cells is 200 nm, which is lower than the wavelength of visual light (i.e., 400-700 nm).

A pyramid-shaped model is used as an example to explain the phenomenon. The maximum height of the pyramid model is set to 15. To simulate the reconstruction of a microscopic object, the wavelength of light is set to 150 in the simulation: i.e., to ten times to the height of the pyramid. The two approaches are used to reconstruct the 3-D view of the microscopic pyramid with the four artificially generated phase images.
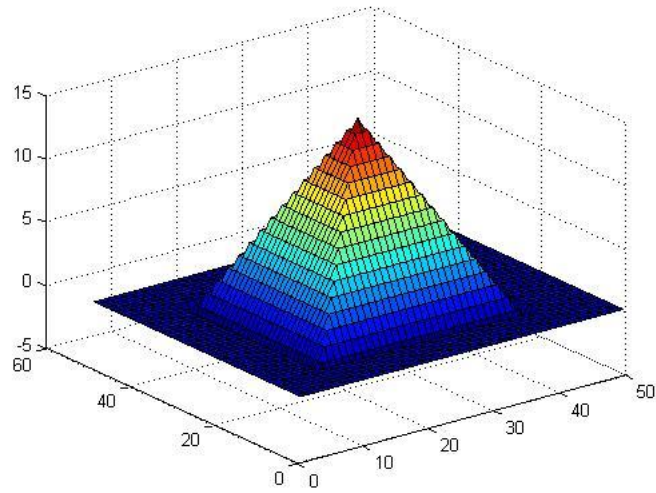
(a)
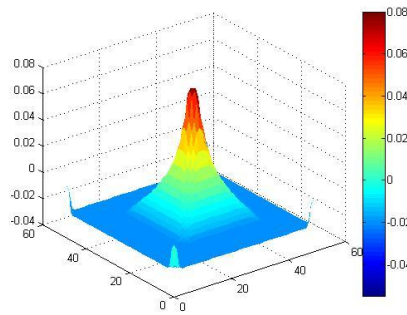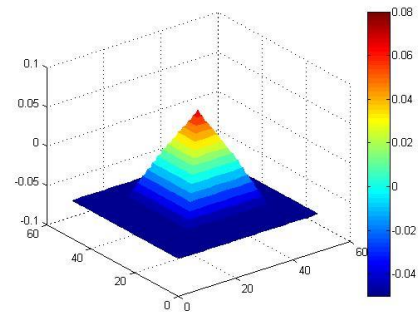
(b)   (c)

Figure 3-16 Reconstruction results from different methods: (a) original pyramid (wavelength of light=150), (b) result from the general path-dependent approach, (c) result from PSI.

The path-dependent approach has a hard time accurately rebuilding the 3-D model of the microscopic pyramid. There is an obvious distortion in its generated result. The result from PSI indicates that the PSI performs better when dealing with objects that are much smaller than the wavelength of light.

However, this recently developed method has excellent performance only with microscopic targets. It fails to reconstruct macroscopic objects. In the second simulation, no alteration is made to the pyramid, but the wavelength of light is switched to 1.5. Thus, the size of pyramid model is larger than the wavelength of light. The results of the two approaches are presented.
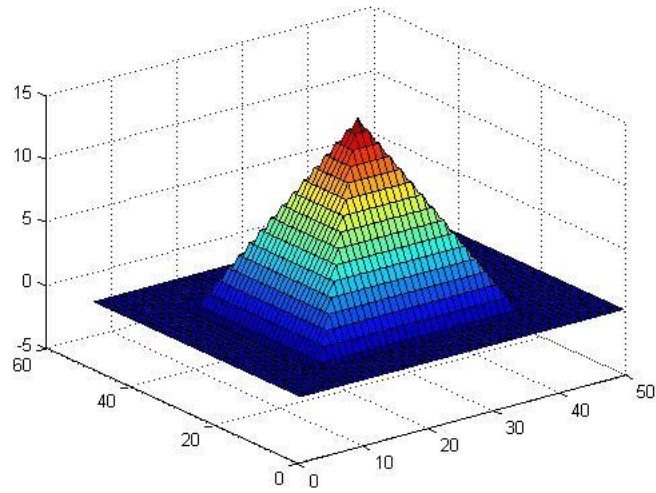
(a)
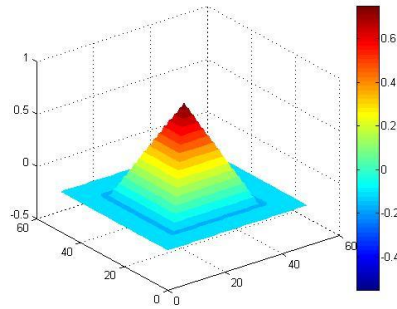
(b)
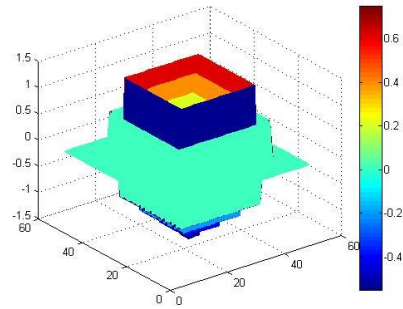
(c)

Figure 3-17 Results with lower wavelength: (a) original pyramid (wavelength of light=1.5), (b) result from the general path-dependent approach, (c) result from PSI.

The results suggest that the PSI stops performing a 3-D reconstruction of the macroscopic target. On the other hand, the path-dependent approach successfully reconstructs the 3-D model. Hence, in summary, both of these two 3-D reconstruction methods can produce a 3-D model of cells. However, since the path-dependent approach is primarily designed for macroscopic objects, distortions often occur while reconstructing microscopic targets (such as cells) by the method. Compared to the path-dependent approach, the PSI method better fulfils the requirements for the calculation of cell volume that has been employed in the monitoring system proposed in this study.

3.4.3 Cell Shape

Using the two techniques—segmentation and phase reconstruction—the shapes of cells can be measured quantitatively. Four basic features of most biological analyses—length, width, thickness, and roundness—are calculated as examples. Two views of the observation area are captured in the dataset: narrow field and wide field.

(a)   (b)
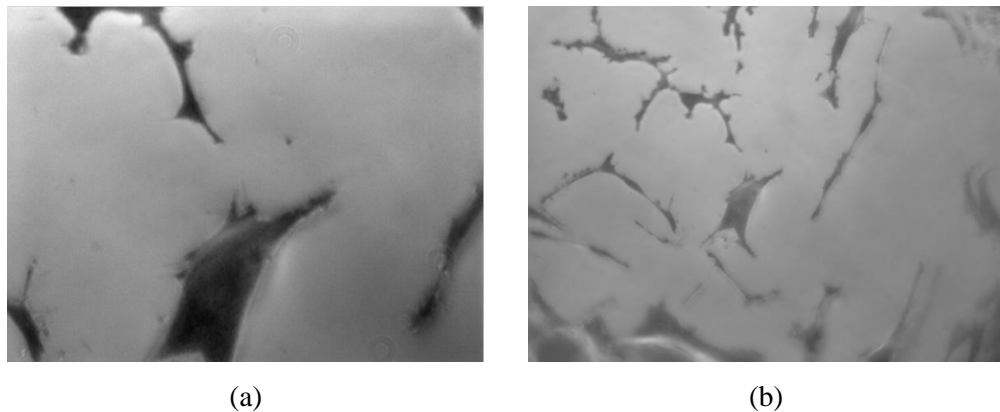
Figure 3-18 Comparison of two types of images: (a) narrow-field TIR image (frame #21), (b) wide-field TIR image (frame #21).

The narrow field zooms in on the centre area of the wide-field image; hence, it can provide more specific observations of details and consequently contains fewer cells than wide-field images. Since the wide-field image can provide a high-quality view to monitor the alterations of shapes for more cells, it is preferable for the experimental simulations.

The cell areas in the TIRM image are referred to the cell adhesion areas that cannot represent the real sizes of cells; thus, the phase map produced by the four phase-contrast images is employed to quantitatively measure the shapes of cells.

(a)   (b)

(c)
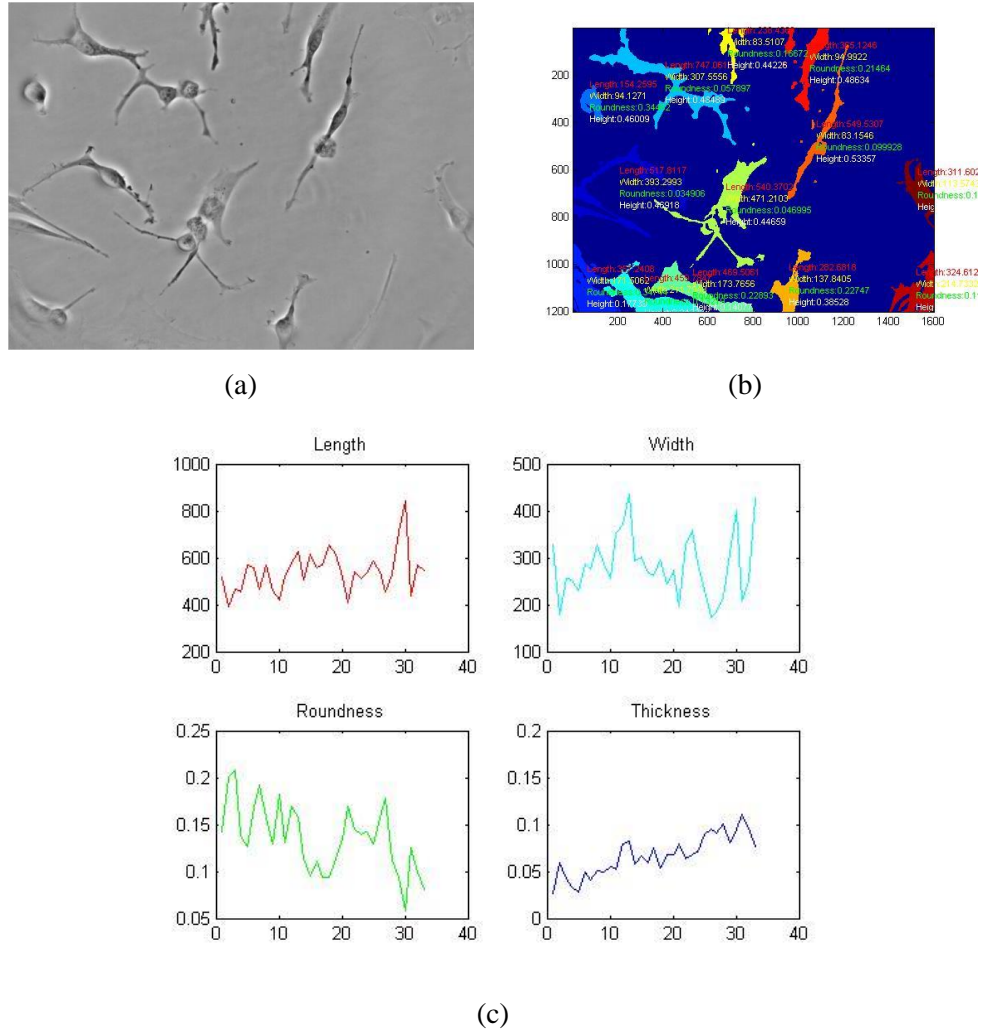
Figure 3-19 Morphology Measurements. (a) Phase map (frame #21); (b) Final outcome; (c) Changes in averages.

Figure 3-19 b) demonstrates the success achieved by the proposed monitoring framework in quantitatively measuring the required cell features. Figure 3-19 c) records across 33 frames the trend of changes in the averages of the four features: cell length, cell width, cell roundness and cell thickness. By analysing these retrieved figures, alterations of the features are found to be consistent with the experimental process. Since most of the cells adhere to the bottom of the slice at the beginning of the experiment, the average thickness is small at the beginning. After the supply of CO_2 is turned off, the cells die and drift to the surface; thus, the cell thickness gradually climbs up in this process and finally reaches a relatively large value. On the other hand, the roundness average falls from a large initial value through this process, which means that the cells alter their shapes from spheres to irregular polygons. The vibrating

averages of lengths and widths reflect the fact that the living environment is not stable for cells such that the cells must continuously alter their shapes.

3.5 Conclusion

This chapter introduced the novel segmentation approach that was exclusively designed to address the problems encountered in most cell images. The newly designed segmentation method combines local- and global-thresholding techniques. This hybrid method is employed to extract cell features from a real-cell image dataset captured by University of Nottingham, United Kingdom. The approach was applied to real-cell datasets and achieved the average segmentation accuracy—i.e., 49.66%. It thereby outperforms typical thresholding approaches. The work of measuring the cell features—e.g. cell volume and cell shape—was also presented. The monitoring results were shown to be consistent with the theoretical prediction.

Chapter 4 Cell Tracking

4.1 Introduction

It is important to understand the mechanisms of cell alterations as cells move during biological processes like the immune response. Because important information about the ability of cells to exert forces on their environment can be extracted from the moving trajectories, a need for the quantitative analysis does exist. The number of images acquired in living-cell studies is large. For example, a live-cell dataset commonly contains more than hundreds of images, each of which contains hundreds of cells. To perform a quantitative analysis, both movements and morphological changes of cells must be accurately tracked—an extremely laborious task for manual tracking. It is therefore worthwhile to develop an automatic tracking system that offers high accuracy.

Similar challenges occur when tracking in various biology experiments. Large numbers of cells must be tracked in each dataset though their similar appearances make it hard to distinguish them. Events such as mitosis and rapid movement are hard to accurately recognize. Since the light conditions are not

stable when images are captured from a microscope, the image quality is typically low, which creates a barrier for cell detection. Also, the sampling frequency varies from less than 10 seconds to 3 images per day, depending on the specific requirements of the applications. Therefore, there may be no obviously spatial overlapped areas of the same cells in adjacent frames. Any of these factors can directly result in the failure of trajectory tracking.

The goal of the work described in this chapter is to develop a reasonable tracking system that addresses these problems. Although the problem of tracking has been comprehensively studied and numerous methods have been proposed, most perform within prior knowledge or specific parameters. These approaches generally recognize cells via spatial overlaps. Consequently, cells with large displacements in neighbouring frames fail to be tracked. Hybrid methods are often built upon combinations of existing methods, leading to a huge volume of computations and a complex framework. All of these shortcomings in existing methods indicate that a general and robust tracking method is badly needed.

In this chapter, a novel framework for cell tracking is introduced. It can accurately detect not only the movements of cells, but also events such as merging, mitosis, entering and leaving. Few parameters are required in the novel approach, and it can be easily adjusted to datasets of different types of cells. To assist the tracking process, multiple features of cells—such as shape, size, and grey scales—have been quantitatively analysed to determine the most discrepant features among cells. Because more features are applied to decide cell associations, the robustness of the method is increased to make it possible to accurately track cells moving at speed. In the system, apart from the main development in the section of tracking, obvious improvements in the segmentation and detection of mitosis and merging have also been developed. All of these improved algorithms together produce a very robust automated cell-tracking system.

4.2 Tracking algorithm with scoring scheme

In this section, the new system is introduced in detail. The new system improves over existing systems in its segmentation algorithm, in its detection algorithm for merging and splitting and in its tracking algorithm. The outcomes of each part have been tested with benchmarks that show a promised enhancement; thus more accurate trajectory-tracking results can be produced with the revised framework.

4.2.1 System outlines

The proposed tracking framework is established on the foundation of a typical segmentation-and-association approach. It first segments the cells in each frame by using the image-segmentation technique; it then associates the same cells according to a specific criterion. While typical approaches rely heavily on cell positions to associate cells, they fail to track cells moving at high speed. To improve the tracking performance of the typical system, cell features such as size and shape are used to assist cell association. A scoring scheme is developed to detect different cell behaviours, e.g. cell splitting and merging. A flowchart of the proposed framework that shows the relationship between different components is presented in Figure 4-1.
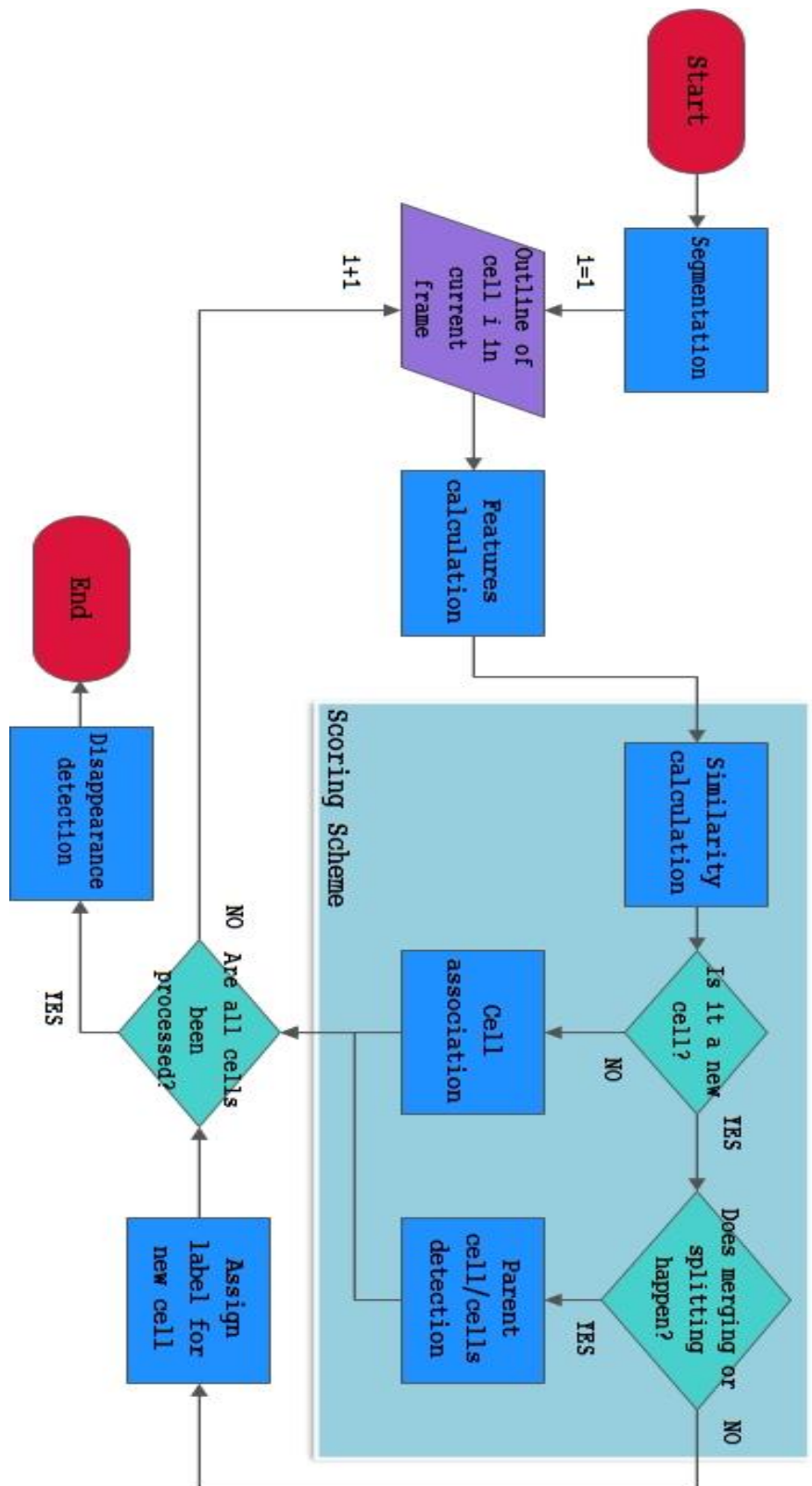
Figure 4-1 Flowchart of the designed system

The features appropriate to assist tracking may be different for specific datasets; thus, the cell features employed for the scoring scheme are substitutable. The system associates cells based on a similarity function that consists of overlapping cell areas, cell positions and cell features—the core of the tracking algorithm.

In what follows, the new system is introduced in detail. Compared to state-of-the-art systems, the new system improves the performance of cell segmentation, cell merging and splitting detection and cell tracking. The results of each part were assessed with benchmark algorithms. The assessment results show that the proposed framework produces accurate tracking performance.

4.2.2 Segmentation

Since the framework is based on the structure of segmentation-and-association, segmentation is an initial step in the process; thus, the performance of the method used for cell segmentation is of particular importance. Due to unstable lighting conditions, the grayscale distribution of captured cell images is usually inhomogeneous. To reduce the error caused by non-uniform grayscale distribution, a two-step, iterative, local thresholding algorithm is proposed. Compared to traditional thresholding methods that use the same threshold to process the whole image, the local-thresholding technique allows different thresholds to process different areas of the image, thus solving the inhomogeneity problem in cell images.

The proposed approach first divides the image into 8x8 sub-images; it then processes each of them in a different way. The final result is produced by assembling the segmentation results of the sub-images. The proposed two-step thresholding first determines whether the sub-image contains cells or parts of cells by comparing the standard deviation of the sub-image with that of the whole image via Eq. (4.1):

$$\begin{cases} if\ \sigma_{sub} < a \cdot \sigma_{whole}, no\ targets \\ otherwise, cells\ or\ part\ of\ cells\ contained \end{cases} \qquad (4.1)$$

where α is a percentage factor that is set to 0.65 in the experiments.

The first threshold, which is calculated using the Otsu approach [10], is applied to the sub-images containing the cells. Due to the non-uniform distribution of greyscales, the extracted cells may be fragmented. To address this issue, a second threshold, also calculated with the Otsu approach, is applied to the minimum square area that contains the cell in the enhanced cell image if the circularity of the cell is lower than a pre-set value (i.e., 0.6, in the paper). The results of the two-step thresholding are assembled to produce the final segmentation result.

The circularity of the extracted cell region is defined in Eq. (4.2):

$$\text{Circularity} = \frac{4 * \text{pi} * \text{Area}}{\text{Perimeter}^2} \tag{4.2}$$

where the perimeter of the object is obtained by the derivative of the object boundary. The value of circularity varies in [0 1], and the circularity of a circle is 1.

4.2.3 Tracking using multiple cell features

In traditional tracking algorithms that use segmentation-and-association techniques, cells are tracked only according to their positions. The approach therefore fails to recognize cells that move at high speed. To address this problem, additional features are measured and used to aid tracking in the approach. This section presents a quantitative analysis of multiple features such as cell size, cell shape, grey scales and the Fourier coefficients in the frequency domain.

4.2.3.1 Feature acquisition

The methods used to quantitatively measure the primary features—such as cell size and cell shape—were presented in section **3.3.2**. Those features mainly provide morphological information about cells. Colour is another common clue that is used for visual recognition. Hence, additional features are taken into account from the view of image grey scales. The histogram of an image is extensively used to analyse the distribution of greyscales. Diverse structures of cells result in different greyscales of cell surfaces observed from microscopes.

Hence, the weighted average of the histogram (G), as defined in Eq. (3), may be used to represent cells for pixel values in cell area:

$$G = \frac{1}{N} \sum_{i=1}^{n} i \cdot h(i) \qquad (4.3)$$

where N is the number of pixels in the cell area, i represents the value of grayscale, n is the maximum grayscale in the histogram, and $h(i)$ represents the entry of the histogram for the corresponding grayscale.

The weighted area is calculated by accumulating the weighted histogram of grayscales. It can be summarized as follows:

$$W = \sum_{i=1}^{n} i \cdot h(i) \qquad (4.4)$$

where i represents the value of grayscale, n is the maximum grayscale in the histogram, and $h(i)$ represents the entry of the histogram for the corresponding grayscale.

4.2.3.2 Cell matching score function

The cell-matching score is a function that is defined to match cells in the neighbour frames. All the assignments of the cell statues are made according to the score. Hence, to introduce the scoring scheme, the similarity function is first defined.

A. Similarity function

The input of the similarity function is the cell features extracted from a given cell and the cells in adjacent frames. The traditional tracking method mainly associates cells in adjacent frames based on the overlapping areas. Cells are often linked to those nearest in the neighbour frame. Errors occur when a cell rapidly moves. To resolve the problem, a score that describes the similarity between different cells is defined in the proposed framework. The similarity score is constructed by combining two components—overlapping factor and distance factor—which can be written as follows:

Similarity score (S) = overlapping factor (O) + distance factor (L)   (4.5)

The overlapping factor is used to track cells with slight movements; the distance factor is defined to track quickly moving cells that have no large overlapping areas between adjacent frames.

Given the cells C_i in frame t and C_j in frame t+1, the overlap factor defined in Eq. (4.5) reflects the degree of overlapping between them:

$$O_{i,j} = \frac{C_i \cap C_j}{\min(C_i, C_j)} \tag{4.6}$$

where $C_i \cap C_j$ represents the size of the overlapping area between the two cells and $min(C_i, C_j)$ is the minimum size of the two cells. The value varies between [0, 1], where *1* means total overlapping and *0* means no overlap.

For the distance factor, Euclidean distances (D) between the processing cell and the cells in neighbour frames are calculated to measure differences in cell positions. If (x,y) represents the position of the central point of cell, the distance can be defined as follows:

$$D_{i,j} = \sqrt{(x_i - x_j)^2 + (y_i - y_j)^2} \tag{4.7}$$

where *i* represents the ith cell in current frame and *j* represents the jth cell in the adjacent frame.

Differences between cell features are used as weights to compute weighted distances. If *F* represents the specific features of the cell, then the distance factor between the ith cell and j[th] cell, L_{ij}, can be defined as follows:

$$L_{i,j} = Norm(|(F_i - F_j)|) \times D_{i,j} \tag{4.8}$$

where *Norm(.)* is the normalization function that transforms the values to the range [0,1].

Since the lower value of distance represents a greater similarity between cells, we inverse the distance by,

$$L_{i,j}^T = 1 - Norm(L_{i,j}) \tag{4.9}$$

4.2.3.3 Cell Association

Cells can be associated with the highest similarity score in the adjacent frame. However, the mechanism causes errors in the event of cell disappearance. For example, if a cell disappears in frame t+1, the corresponding cell in frame t is linked to the wrong cell with the highest score in t+1. To prevent this error, the framework links cells backwards: i.e., connections are made from frame t+1 to frame t. Nevertheless, the new appearances of cells result in another problem. Assuming that Cj is a newly appearing cell in frame t+1, the solid lines in Figure 4-2 represent the correct association and the dotted lines represent the potential links for cell Cj. Due to the lack of a detection scheme for newly appearing cells, cell Cj is mistakenly connected to the cell with the highest similarity score.
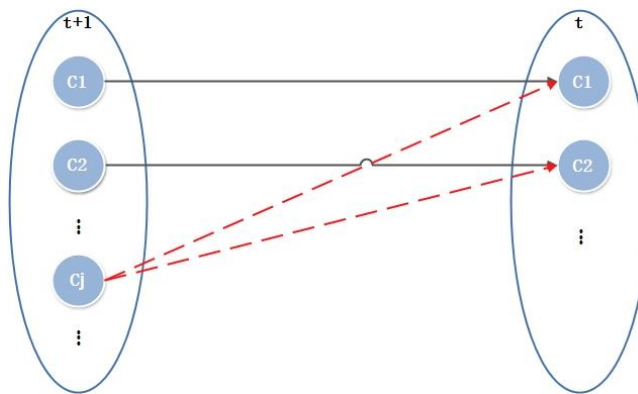
Figure 4-2 Linking problem of the new cell. The newly appeared cell in frame t+1 is incorrectly connected to the cell with highest score in frame t without status verification.

New cells can be classified in two ways: as cells that have entered the region of interest, and as products of cell activities such as splitting and merging. Statuses of newly entering, splitting and merging are assigned to the cells from corresponding events, according to the scores calculated by the detection method. The status of disappearance is assigned to the cells in frame t that disappeared in frame t+1.

A. Cell merging and splitting

Detection of merging and splitting is performed manually in traditional tracking algorithms. An automatic detection method that uses overlapping cell areas is developed for the proposed tracking framework.

For convenience, the cells in frame t+1 that are generated from cell splitting or cell merging are called son cells, and the corresponding cells in frame t are called parent cells. Assume that there are N cells in frame t and M cells in frame t+1. Let $B_{i,j}$ denote the overlapping area between cell i in image t ($C_{i,t}$) and cell j in image t+1 ($C_{j,t+1}$). A look-up table of the overlapping areas can then be formed as follows:

	$C_{1,t+1}$	$C_{2,t+1}$	…	$C_{j,t+1}$	…	$C_{M-1,t+1}$	$C_{M,t+1}$
$C_{1,t}$	$B_{1,1}$	$B_{1,2}$	…	$B_{1,j}$	…	$B_{1,M-1}$	$B_{1,M}$
$C_{2,t}$	$B_{2,1}$	$B_{2,2}$	…	$B_{2,j}$	…	$B_{2,M-1}$	$B_{2,M}$
…	…	…	…	…	…	…	…
$C_{i,t}$	$B_{i,1}$	$B_{i,2}$		$B_{i,j}$	…	$B_{i,M-1}$	$B_{i,M}$
…	…	…	…	…	…	…	…
$C_{N-1,t}$	$B_{N-1,1}$	$B_{N-1,2}$	…	$B_{N-1,j}$	…	$B_{N-1,M-1}$	$B_{N-1,M}$
$C_{N,t}$	$B_{N,1}$	$B_{N,2}$	…	$B_{N,j}$	…	$B_{N,M-1}$	$B_{N,M}$

<div align="center">Figure 4-3 Look-up table of overlapping areas</div>

Since only cells in nearby regions have overlapping areas, most of the $B_{i,j}$ in the look-up table are zeros. Hence, the ancestral relationship between cells can be determined by checking the entries of the look-up table. The algorithm for split/merge detection can be summarized as follows:

Input: look-up table (ToB) of overlapping weighted areas ($B_{i,j}$) between cells in adjacent frames, and the association map (AM).
Output: association map with labels of splitting and merging.

1. Check the ToB column-by-column and pick up the cells j with more than one non-zero $B_{k,j}$, $1 \le k \le N$.
2. Compare the non-zero overlapping areas ($B_{i,j}$) with the cell area of the parent ($C_{i,t}$). The event of cell merging is detected if more than one parent cell satisfies the following condition: $B_{i,j} > \alpha A_i$, where α is a percentage factor (i.e., 0.7 in the experiments).
3. Add the label for cell merging to the corresponding cells in the association map.
4. Check the ToB row-by-row and pick up the cells i with more than one non-zero $B_{i,l}$, $1 \le l \le M$.
5. Compare the non-zero $B_{i,j}$ with the cell areas of the sons ($C_{j,t+1}$). If more than one son cell satisfies the condition, $B_{i,j} > \beta A_j$, where β is a constant (i.e., 0.5), then cell splitting is detected between the parent cell i and the son cells j.
6. Add the labels for cell splitting to the corresponding cells in the association map.

The score scheme with additional statuses, splitting (S) and merging (M), is represented in Figure 4-4. The solid lines represent the correct association. The dotted lines represent potential links, and the dotted lines in red and green represent potential ancestral relationships between son and parent cells.
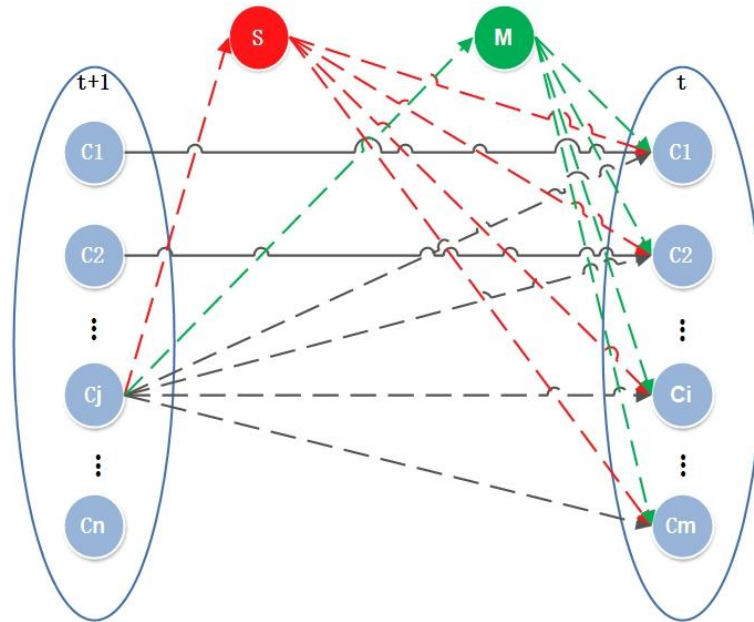
Figure 4-4 Association component with statuses of splitting and merging

J. A. Withers and K. A. Robbins proposed an automatic method for cell event detection. It efficiently computes the overlapping area of the bounding boxes of cells in adjacent frames and their central distances—called the overlap-distance ratio—to detect the event of split/merge.

(a)   (b)
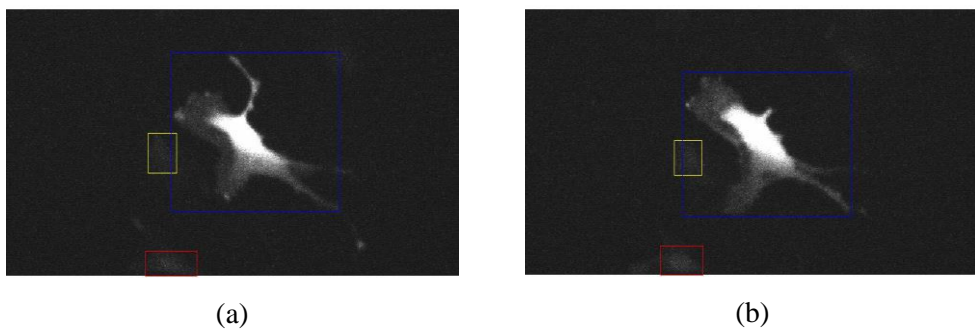
Figure 4-5 Problem of bounding box in MSC dataset. (a) and (b) are two adjacent frames in a sequence in MSC. The cell in yellow box ran into the blue box of another cell, which may be wrongly recognized as a fusion in the typical detection method.

However, a false merging event may be detected by the approach in the case of the fast-moving cell: e.g., the cell bounded with yellow box in Figure 4-5

that is entering the blank area of the bounding box for other cell (i.e., the cell bounded with blue box). Compared to the typical approach [89], our detection method replaces the bounding box with cell area, thus preventing errors caused by fast-moving cells.

B. Cell entering and disappearing

Cells that enter the region of interest (ROI) also produce new appearances of cells. The newly entering cells have no potential parents in the previous frame; thus, their matching scores with the cells in previous frame are low. A pre-set score (S^A)—i.e., 0.8—is employed to accurately detect cell entering. Assuming that cell j is in frame t+1, cell j is detected as newly entering if the following condition is satisfied:

$$\textbf{Newly Entering Cell,} \qquad \textbf{if } \max_{1 \leq k \leq m} \left(S_{k,j} \right) < S^A \tag{4.10}$$

where m is the number of cells in frame t.

A new label is assigned to the newly entering cell.
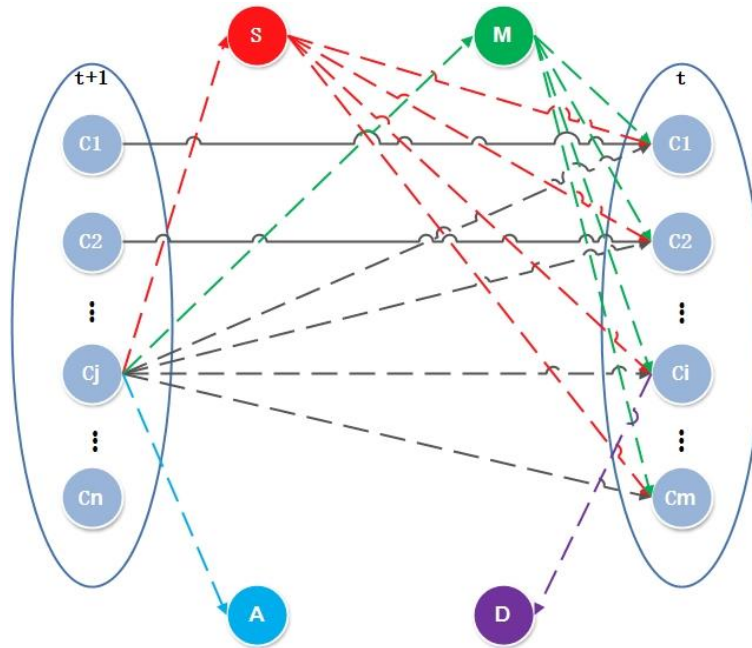
Figure 4-6 Association component with statuses

With the additional scores of newly entering, splitting and merging, all of the cells in the current frame t+1 can be associated with cells in previous frame or

marked with different statuses. The cells with no connections in the previous frame t are marked as disappearing. Cell splitting is labelled as S, cell merging as M, newly entering cells as A and disappearing cells as D. The relationships between statuses are diagrammatically shown in Figure 4-6.

In the proposed framework, a cell j in frame t+1—except for common associations based on similarity scores, which are the black, dotted lines in Figure 4-6—has three additional links to the potential statuses: splitting, merging and new entering. These links are the coloured, dotted lines in red, green and blue. For the cells in frame t, an additional status, disappearing—which is represented by the dotted purple line—is also employed to trace cell disappearances. The uses of statuses enable the framework to record and trace the parent cells in the previous frame and the cell events including splitting, merging, newly entering and disappearing. Hence, the system can finally produce a spanning tree of the tracking cells across all the frames.

4.3 Experimental results

In this section, the results of segmentation and tracking are presented. The results have been evaluated with the ground truths offered by the dataset provider.

4.3.1 Introduction of datasets

Three datasets of different cells, MSC, GOWT1 and SIM, introduced in ISBI 2013 challenge and one dataset, SIM+, from ISBI 2014 challenge [4, 90] are used for performance evaluation. Detailed information about the datasets is listed in Table 4-1. Further information can be found in the *Appendix*. Each dataset contains multiple sequences, and each sequence contains more than 40 frames at high resolution (up to 1024$\times$1024). This results in an extremely large volume of data for the system to process.

	Rat mesenchymal stem cells (MSC)		Mouse stem cells (GOWT1)		Simulated nuclei moving (SIM)						Simulated nuclei of HL60 cells (SIM+)	
Sequence No.	1	2	1	2	1	2	3	4	5	6	1	2
Image Size	992×832		1024×1024		APPR 600×600						APPR. 650×700	
No. of Frames	48	48	92	92	56	100	100	56	76	76	65	150
Total No. of Cells	15	10	27	50	48	59	72	97	62	112	97	145

Cells in different datasets have different characteristics. For example, rat mesenchymal stem cells (Figure 4-7 (a)) are often long and slim while mouse stem cells (Figure 4-7 (b)) are nearly circular. Figure 4-7 (c) and (d) are created by software that simulates the moving nuclei. The system is required to have excellent flexibility among different datasets. Few of the existing methods can perform well throughout these four datasets.

(a)   (b)   (c)   (d)
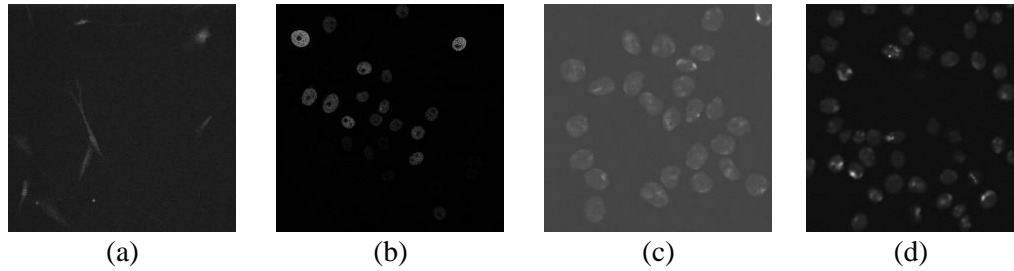
Figure 4-7 Sample image from each dataset: (a) image from MSC, (b) image from GOWT1, (c) image from SIM, (d) image from SIM+.

The dataset providers also provide the manually annotated ground truth, which contains the information of cell moving trajectories and shape variations. Segmentation and tracking accuracies can be assessed using the annotated ground truth.

The proposed framework is compared with four participators of ISBI 2013: COM-US, LEID-NL, PRAG-CZ and KTH-SE. COM-US is a tracking framework that employs the multiple-hypothesis tracking paradigm designed by Compunetix Inc, USA. LEID-NL is a model-evolution based approach in which segmentation and tracking tasks are performed simultaneously. It is an extended framework of their earlier work [91]. In the experiments, LEID-NL failed to work on several sequences of the datasets, which are marked as NA (not available) in the following tables. PRAG-CZ is an improved version of the segmentation-and-association framework proposed by Charles University

in Prague, Czech Republic. The segmentation component for this framework is a local thresholding method that uses k-means for threshold selection. KTH-SE is also a segmentation-and-association framework that segments cell images by thresholding after band-pass filtering. It employs a greedy algorithm in its track linking component to improve tracking performance.

4.3.2 Evaluation criterion

Segmentation accuracy is measured using the Jaccard similarity index (J) introduced in **3.4.2**. For tracking accuracy, if we assume that node M_i^t is cell i in frame t in a sequence, a graph with links can be used to represent the cells tracked by different systems. See Figure 4-8 for an example of such a graph. Different colours visualize different cells, and dotted lines represent parent links. The links between nodes—i.e., the dotted and solid lines that link the nodes in Figure 4-8—are labelled as edges, E. To compare the graph generated by the proposed framework with the manually generated ground-truth map, the evaluation system measures the number of cells not detected (false negatives, FN), the number of cells incorrectly detected (false positives, FP), the number of cells correctly detected (true positives, TP), the split operations that must be corrected in the results (NS), the edges that must be removed (ED), the missing edges (EA) and the edges that mismatch the track link and parent link (EC). The weighted sum of the number of necessary operations required to transform the results to the ground truths can be defined as follows:

$$TRA_P = \omega_{NS}NS + \omega_{FN}FN + \omega_{FP}FP + \omega_{ED}ED + \omega_{EA}EA + \omega_{EC}EC$$

where the weights (ω) are defined manually according to the difficulties of making corresponding operations.

The weights were set according to the manual effort required to revise faults in the generated tracking results. The weights have been listed in Table 4-2. The larger weights indicate problems that are harder to correct.

ω_{NS}	ω_{FN}	ω_{FP}	ω_{ED}	ω_{EA}	ω_{EC}
5	10	1	1	1.5	1

The TRA_P measure is normalized to the [0, 1] interval. It is equal to zero when the results are identical to the ground truths. The accuracy of tracking can then be measured by,

$$TRA = 1 - \frac{\min(TRA_P, TRA_E)}{TRA_E}$$

where $TRA_E = \omega_{FN}|M| + \omega_{EA}|E|$ is the cost of creating the ground truth graph.
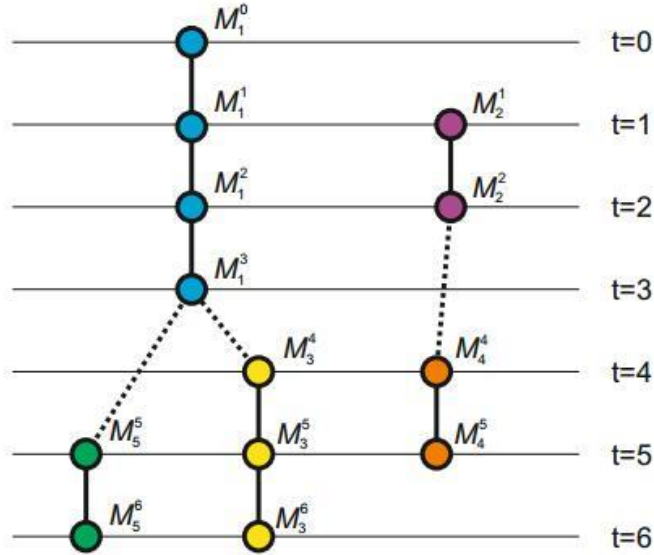
Figure 4-8 An example of ground truth tracks

4.3.3 Segmentation results

4.3.3.1 Results of proposed two-step segmentation method for GOWT1

Since the proposed two-step thresholding technique uses the circularity of cells to refine the segmentation result, it is more efficient to process cells with circular shapes, such as mouse stem cells. An example is shown in Figure 4-9. The segmentation results illustrate that the proposed approach addresses the problem of fragmentation well: i.e., the cells marked with a red circle in the first step (Figure 4-9 (c)) are fully recovered in Figure 4-9 (d).
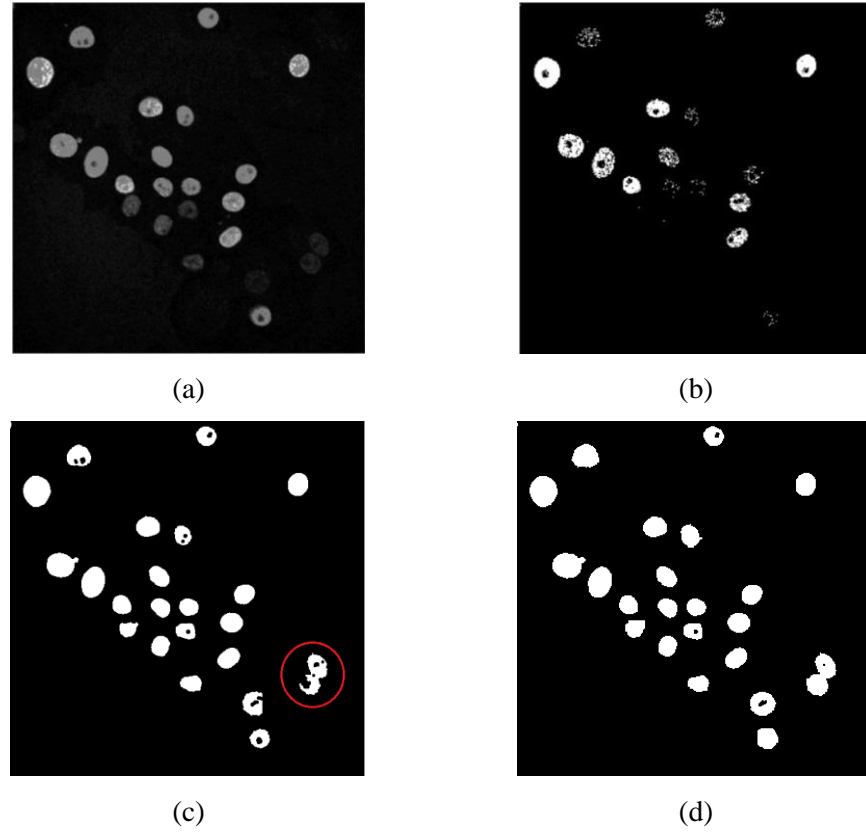
Figure 4-9 Comparison with benchmark algorithm: (a) the original image, (b) result from Otsu thresholding, (c) the result of the first segmentation (the red circle indicates segmentation error), (d) result from proposed two-step thresholding.

To further demonstrate the improved segmentation performance, the result of the widely used approach--global Otsu thresholding [10]—is shown in Figure 4-9 (b) for comparison. Otsu determines the threshold according to the between-class variance of the image. It can be observed from Figure 4-9 (b) that a large amount of cell information is lost. Compared to the result of global Otsu, the proposed approach extracts the outlines of cells very well.

4.3.3.2 Evaluation of segmentation accuracy

The segmentation approaches employed in the proposed framework are evaluated with the Jaccard similarity index (J) introduced in **3.4.2**. The proposed two-step, iterative, thresholding-segmentation method is applied only to the GOWT1 dataset to address the fragmentation problem. The MSC is segmented by the local and global thresholding approach introduced in section **3.2**. The segmentation approach proposed by KTH-SE is used to process the datasets of SIM and SIM+. Apart from the segmentation methods proposed by

the ISBI 2013 participators, two of the typical thresholding approaches—global Otsu and, which provide the best segmentation accuracies for MSC—are also taken as benchmark algorithms. Table 4-3 shows the segmentation accuracies (SEG) of different approaches for each dataset.

Table 4-3 Segmentation accuracy (%)

	MSC		GOWT1		SIM						SIM+	
Seq. No	1	2	1	2	1	2	3	4	5	6	1	2
Global Otsu	32.67	47.97	61.99	83.06	69.85	52.06	64.90	65.59	65.35	52.85	79.21	13.82
Global Fuzzy-entropy	36.47	49.75	59.87	73.71	69.73	54.79	78.81	38.66	77.05	28.12	78.21	25.54
COM-US	32.11	23.73	44.83	53.35	62.63	68.46	68.33	65.36	61.24	66.19	19.42	1.83
LEID-NL	NA	NA	NA	NA	NA	68.96	58.77	73.45	NA	41.03	69.80	NA
PRAG-CZ	41.00	54.93	81.13	**91.90**	90.96	73.76	76.23	75.91	70.97	71.38	69.03	32.14
KTH-SE	**46.23**	**57.95**	58.33	89.42	**92.70**	**89.88**	**86.85**	**87.85**	**81.77**	**84.18**	**83.77**	**34.26**
Proposed Method	43.03	56.29	**85.56**	85.18	92.70	89.88	86.85	87.85	81.77	84.18	83.77	34.26

From Table 4-3, it can be observed that KTH-SE achieves the best segmentation accuracies for MSC, SIM and SIM+ among the benchmark algorithms. Our proposed approach provides the best segmentation accuracy for the GOWT1 datasets: i.e., 85.56%, for sequence #1. It also provides the best reasonable accuracy: i.e., 85.18%, for sequence #2, which is 6.72% lower than the winner, PRAG-CZ (i.e., 91.90%).

4.3.4 Tracking results

4.3.4.1 Evaluation of the frameworks with different features

Each of the presented cell features is tested with the proposed tracking framework. The tracking accuracies (**TRA**) that use different features are listed in Table 4-4.

Frameworks that employ different cell features for cell association are evaluated with respect to the same segmentation results. The entry labelled 'position only' provides the tracking accuracies for the framework using only distance for feature representation. The entries below are for the frameworks that combine distance and different cell features. Table 4-4 shows that tracking accuracy is improved by adding features to the distance. The average increases for each type of cells are 1.04% for MSC, 1.18% for GOWT1, 0.43% for SIM

and 0.05% for SIM+. Although tracking accuracy is increased by adding features for most cell datasets, degradations are found for some sequences: e.g., sequence #1 of MSC and SIM+. Unreliable segmentation results caused the degradations of sequence #1 of MSC and sequence #2 of SIM+. Their accuracies are lower than 50%. The cell features extracted from poorly segmented images may be inaccurate, which can lead to errors in the process of cell association. The dataset of sequence #1 of SIM+ has contains a large volume of cells that move slightly between frames. Furthermore, cells in the two datasets are small and similar in appearance—two characteristics that can result in small differences of cell features between cells. For these reasons, the distance designed to detect fast-moving cells fails.

In general, the results demonstrate that, compared to the tracking framework that uses only cell positions, a framework that adds cell features generates tracking accuracy. One of the main sources of improvement is the correct detection of cells with sharp movements.

Table 4-4 TRA for different cell features (%)

		MSC		GOWT1		SIM						SIM+	
Sequence No.		1	2	1	2	1	2	3	4	5	6	1	2
Position Only		85.79	84.23	97.97	96.07	99.48	98.76	98.25	98.53	97.21	98.21	98.14	50.83
Position and	Size	**86.04**	84.37	**98.68**	97.62	**99.70**	98.86	98.50	98.76	97.69	98.71	98.00	50.85
	Shape	85.79	84.37	**98.68**	97.50	**99.70**	**98.92**	**98.55**	98.71	**98.04**	98.65	98.09	**50.91**
	Histogram of Grayscales	**86.04**	**86.05**	98.63	97.56	**99.70**	98.80	**98.55**	98.73	97.96	**99.02**	**98.16**	50.77
	Weighted area	85.67	85.35	98.51	97.57	**99.70**	**98.92**	98.46	98.73	97.69	98.65	98.00	50.82

To show the advantages of the proposed approach, frames #38 to #41 from sequence 2 of 'MSC' dataset were overlapped to create the image shown in Figure 4-10 (a). It is confirmed by observation that no splitting and merging occurred in the frames, thus the area for each cell in Figure 4-10 (a) can be treated as the ground truth that represents their moving trajectories. The cell in the red circle exhibits a sharp movement between adjacent frames: i.e., 74 pixels. Figure 4-10 (b) and (c) show tracking results from the framework that uses only cell position and from the framework that combines histogram of grayscales. The two tracking results are produced with the same set of segmented frames. The colour lines from the centres of cells in the results represent the detected moving trajectories of cells across the frames. The fast-moving cell is labelled with marker '91' in (b), and it is marked with '88' in (c). While the two frameworks generate similar moving trajectories for other cells, the trace line for the fast-moving cell is missing in (b).

(a)

(b)   (c)
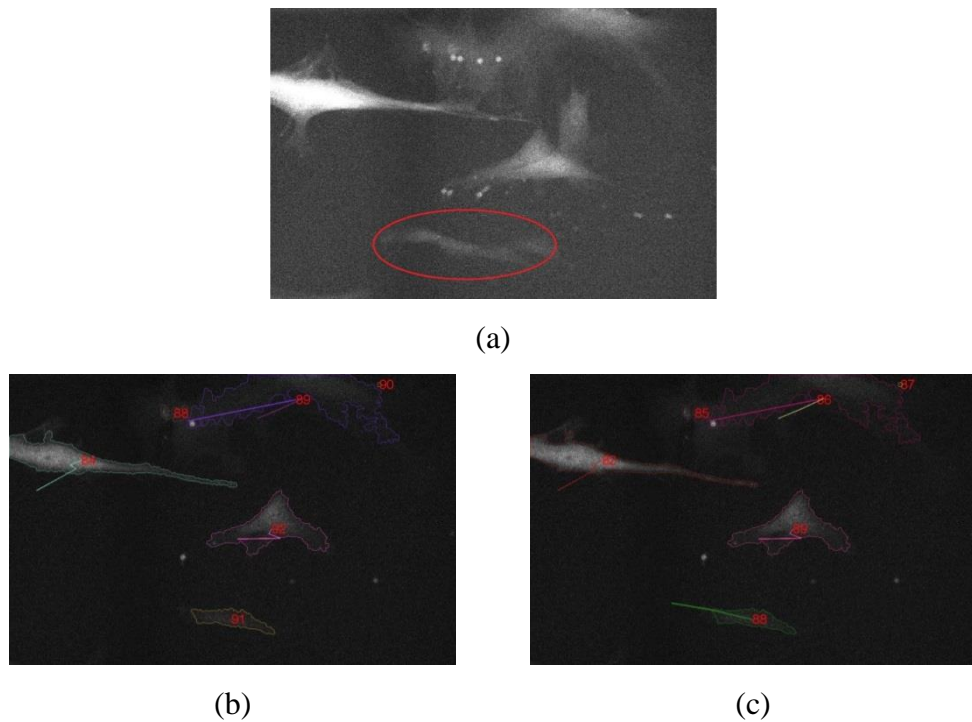
Figure 4-10 Comparison of the performances with cells moving in high speed: (a) the image overlapping the whole testing frames, (b) the traditional algorithm, (c) the proposed algorithm.
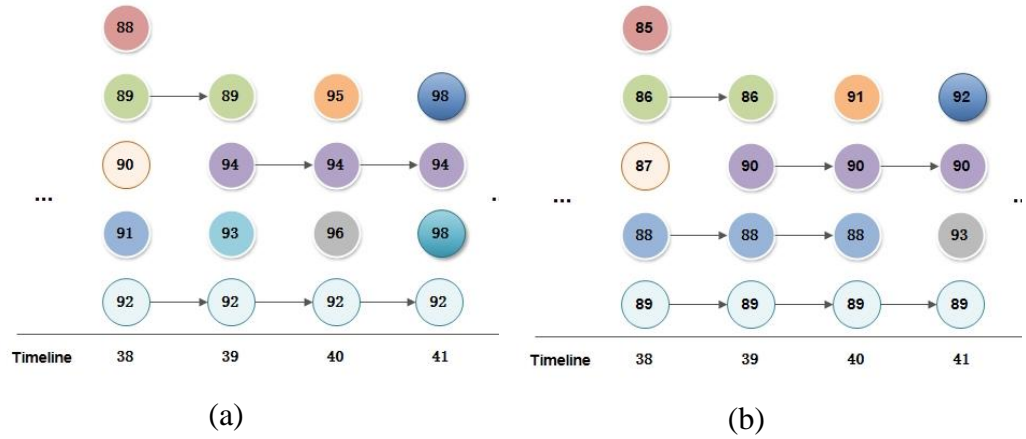
Figure 4-11 Spanning trees of the tracking results: (a) using cell position only, (b) combining position and the feature of weighted area.

The spanning trees of the two tracking frameworks for videos from frame #38 to #41 are generated and shown in Figure 4-11. The circles with numbers represent the cells in each frame. The lifetime of each cell can be clearly monitored from the spanning tree. Figure 4-11 illustrates that the framework with HOG accurately tracks the trajectory for the fast-moving cell marked with the red circle in Figure 4-10 (a), whose movement was not detected by the framework that uses cell position only.

4.3.4.2 Comparison with state of the art methods

In addition to the participators for ISBI 2013, tracking frameworks that employ the global Otsu and global fuzzy entropy for segmentation and the overlapping factor defined in Eq. (4.6) for association—which are named as OA-Otsu and OA-FE—are included for tracking performance evaluation. The tracking accuracies for the proposed framework and benchmark algorithms on different datasets are listed in Table 4-5.

Table 4-5 TRA for different approaches

Seq. No	MSC			GOWT1			SIM							SIM+			Average
	1	2	Average	1	2	Average	1	2	3	4	5	6	Average	1	2	Average	
OA-Otsu	72.49	00.00	36.25	93.30	94.14	93.72	91.13	71.67	88.63	91.26	88.15	72.24	83.85	97.23	00.00	48.62	71.69
OA-FE	64.98	00.00	32.49	76.82	77.69	77.23	73.99	57.11	96.44	46.45	96.56	25.89	66.07	94.76	34.99	64.88	62.14
COM-US	65.41	29.86	47.64	72.99	44.80	58.90	79.07	84.33	89.60	85.45	79.55	83.23	83.54	26.30	00.00	13.15	61.81
LEID-NL	NA	NA	NA	NA	NA	NA	NA	88.71	83.24	89.50	NA	73.29	NA	87.27	NA	NA	NA
PRAG-CZ	59.04	45.92	52.48	98.14	97.72	97.93	90.96	87.69	90.06	92.03	73.93	84.63	86.55	90.29	44.36	67.33	78.37
KTH-SE	86.24	80.07	83.16	93.48	94.52	94.00	99.67	98.97	98.43	98.72	97.78	98.80	98.73	97.52	47.86	72.69	91.52
Proposed Method	86.04	86.05	**86.05**	98.68	97.71	**98.20**	99.70	98.92	98.55	98.80	98.04	99.02	**98.84**	98.16	50.91	**74.54**	**92.93**

Table 4-5 reveals that the OA-Otsu and OA-FE fails to track the cells in sequence #2 of MSC. This is because the cells in sequence #2 of MSC move rapidly, resulting in few overlapping cell areas between adjacent frames. The OA-Otsu and OA-FE use only the overlapping factor for cell association; thus, they fail to track rapidly moving cells. The failures of OA-Otsu and OA-FE demonstrate the need to develop a distance factor for detecting cells with sharp movements.

The PRAG-CZ, KTH-SE and our framework are based on the same framework structure—segmentation and association—which relies on good segmentation for accurate tracking. As shown in Table 4-5, PRAG-CZ achieves the best tracking accuracy for benchmarking algorithms: i.e., 97.93% for the GOWT1 dataset. KTH-SE yields the best accuracies for MSC, SIM and SIM+: 83.16%, 98.73% and 72.69%, respectively. The average accuracies for the proposed framework on MSC, GOWT1, SIM and SIM+ are 86.05%, 98.20%, 98.84%, and 74.54%, respectively. It thus outperforms all benchmark frameworks. As the SEG of our proposed framework is lower than KTH-SE and PRAG-CZ for MSC and GOWT1, the better TRA accuracy demonstrates the excellent capacity of our cell association relative to the proposed scoring scheme. The overall average tracking accuracy of the proposed framework is 92.93%, which is 1.41% higher than that of KTH-SE (i.e., 91.52%).

In summary, adding additional cell features to cell association produces an improvement in tracking accuracy for the system. The proposed framework tracks cell movements and detects cell events—such as cell merging, splitting, appearance and disappearance—with outstanding accuracy: i.e., 92.93%, on average. Trajectories of the cell movements are recorded for further analysis by the framework, as shown in Figure 4-12. The cells are marked with separated identifiers. The different coloured lines represent the trajectories of different cells across the sequences.

<div style="text-align: center">(a)   (b)</div>
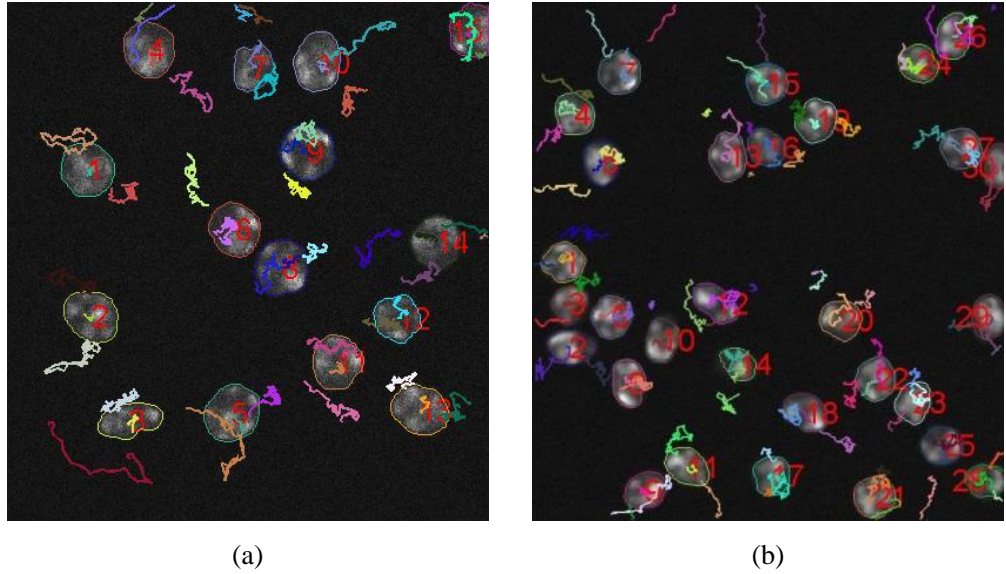
Figure 4-12 Trace lines for cells across the video. (a) The output of sequence #1 from SIM. (b) The output of sequence #1 from SIM+. Lines in different colours represent the moving trajectories for different cells.

4.4 Conclusion

This chapter introduces a tracking framework designed for time-lapse cell images. The framework is a revised version of the typical segmentation-and-association approach. It uses multiple extracted cell features to perform accurate tracking. It achieves excellent tracking accuracy—the average is 92.93% for four different practical datasets—and it addresses the problem of tracking cells with sharp movements, which is difficult for most existing tracking approaches.

Chapter 5   Fast-processing techniques

5.1 Introduction

Image processing is an extensively studied area. The techniques have been successfully implemented in various applications for different purposes. Edge detection and visual tracking are two problems that are commonly encountered during image processing. Substantial efforts have been made to improve the accuracy of the approaches that address these two tasks, such as the revised methods developed in [92, 93]. As a result of these efforts, the accuracies that can be achieved for these two tasks increase and gradually become acceptable for some practical applications.

Microscope images create challenges that are unlike those associated with general images. For edge detection, the relatively poor quality of captured images often results from the fact that the conditions for capturing cell images vary widely. For tracking, the huge volume of cells and various cell behaviours present the primary difficulties. Analyses of these challenges have been made and methods have been proposed in previous papers [70, 94].

Although most of these studies have tried to improve the accuracies of their performances, few provide the improvements of processing speed. The requirements of current biological applications are notably growing. Therefore frameworks are needed that can perform edge detection and visual tracking in real-time.

This chapter first introduces a novel hybrid edge-detection method that is based on the fuzzy entropy and Canny operator. Then it presents a fast-tracking framework designed for microscope images. The performances of these two approaches have been evaluated with benchmark methods; the results demonstrate that they have high potentials to be implemented in real-time applications.

5.2 Edge-detection technique

To assist cell biologists in their research, numerous image-processing techniques have been applied to images of cells. Among them, the method employed for cell segmentation is of pivotal importance, as it is the essential step for many further analyses. However, the conditions for capturing cell images vary widely, which often means that the contrast is extremely low, the distribution of grey scale is non-uniform, and the images are noisy (e.g., with salt-and-pepper noise). These factors increase the difficulty of performing accurate detection. Although there are a great many existing segmentation methods [95, 96], few can simultaneously solve these three problems.

Among the existing methods, the Canny operator is one of the most powerful edge detectors. It has proven success when applied to various tasks. However, due to the low quality often exhibited by cell images, the performance of the Canny operator is lower than would be expected. In this section, a novel method is proposed to improve the performance of the Canny edge detector. The thresholding method based on fuzzy entropy theory is used with the Canny operator to select the threshold gradient. This approach takes more information into consideration when performing the thresholding, which results in greater robustness with respect to noise.

5.2.1 Algorithm

This section presents various ways to address the problems outlined in the Introduction.

A. Low Contrast

The quality of cell images generated by biological microscopes is often less than ideal in terms of contrast and sharpness (i.e., the cells are blurred). This leads to a loss of detail and to the detection of false edges. The existing method [14] of using morphological transforms to enhance image quality is employed in this edge-detection operator. Although this method enhances image contrast, it introduces the problem that the noise in the image is increased as image quality is enhanced.

B. Non-uniform Grey-Scale Distribution

The traditional Canny edge detector is a global operator that uses parameters such as the threshold applied to gradients to process entire images. This leads to problems when the image has a non-uniform distribution of grey scales. In such images, the appropriate threshold varies across the image and should be adjusted from a global value to local values to accommodate fluctuations of grey levels.

To introduce local thresholding, the image is split into sub-images. Each sub-image is then processed with a revised Canny operator. The final output image is produced by assembling results from these sub-images. By allowing different parameters to be applied to different areas of the image, the inhomogeneity problem is solved.

C. Noise

A typical Canny operator uses the following steps to extract edges:

1. Remove white Gaussian noise by smoothing the image with a Gaussian filter.

2. Calculate the magnitude and direction of the gradient at each pixel.

3. If the gradient's magnitude at the processing point is larger than the gradients of the two neighbours when laid in the gradient direction, the processing pixel is marked as the edge. Otherwise, it is marked as the background.

4. Use hysteresis thresholding to remove weak edges.

Applying this approach to real data suggests that inaccuracies in segmentation result primarily from Step 3 since it is a process that is very sensitive to noise. This is the reason why an alternative method is proposed that is based on Fuzzy Entropy, whose basic theory is now introduced.

D. Fuzzy Entropy

Fuzzy entropy is the entropy of a fuzzy set, which loosely represents the information of uncertainty [97, 98]. It is usually used to quantify the value of information included in a message. Defining X as a set of discrete random variable with values $\{x_1, ..., x_n\}$ and $P(X)$ as the probability mass function, the corresponding entropy H is defined as follows:

$$H(X) = \sum_i P(x_i)I(x_i) = -\sum_i P(x_i)\log_b P(x_i)$$

(5.1)

where I is the information content of x, and b is the base of the logarithm.

The thresholding method based on fuzzy entropy theory calculates the entropy of a fuzzy set and then normalizes it as the threshold, which maximizes the entropy. Fuzzy sets were first defined by Zadeh in 1965 [99]. They are sets whose elements have degrees of membership. The pixels in an image exemplify fuzzy sets. In an image, there are usually two classes: objects and background. If a membership function is defined, the degrees of pixels that belong to the different sets can be calculated. Based on the obtained memberships, pixels can be separated into correct groups; this the basic idea behind pixel clustering.

In the proposed method, fuzzy entropy theory is used to distinguish gradients for edges from gradients produced by noise. The gradients of the image

generated by the Canny operator is a set of values that can be classified into two groups: edges and noise. Here the membership functions, μ, are defined by the following:

$$\mu_A(x) = \begin{cases} 0, & x \in B \\ \dfrac{b-x}{b-a}, & x \in A \cap B \\ 1, & x \in A \end{cases} \tag{5.2}$$

$$\mu_B(x) = \begin{cases} 1, & x \in B \\ \dfrac{x-a}{b-a}, & x \in A \cap B \\ 0, & x \in A \end{cases} \tag{5.3}$$

The relationship between membership functions is shown diagrammatically in Figure 5-1.
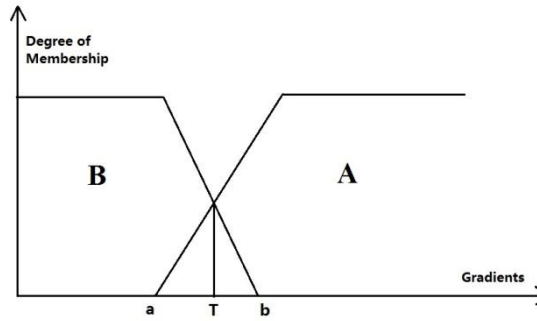
Figure 5-1 Diagram of membership function

The parameters, a and b, are unknown. This means that the entropies of these two groups change in response to alterations in a and b. Theoretically, a larger entropy means that the test objects contain more information. Therefore, the gradient maximizing the joint entropy of this fuzzy set is set as the threshold. The concept of joint entropy was introduced in [100]. Let the entropy be H, so that the entropy for A can be represented as,

$$H(A) = -\sum_{j=1}^{L} \frac{\mu_A(j)h_j}{P(A)} \lg \frac{\mu_A(j)h_j}{P(A)} \qquad (5.4)$$

where $h(j) = \dfrac{N_j}{N_{total}}$; N_j is the number of points whose gradients are equal to j;

and N_{total} denotes the number of total points.

Hence, the joint entropy is,

$$\begin{aligned} H(AB) &= H(A \mid B) + H(B) \\ &\leq H(A) + H(B) \end{aligned} \qquad (5.5)$$

They become equivalent if and only if these two sets of data are independent. From (10), it is obvious that the task of thresholding is converted to that of finding the maximum of the total entropy of gradients.

5.3 Performance Evaluation for edge detection

The proposed edge detector is implemented with the samples captured by the University of Nottingham, United Kingdom (UNUK). The experimental results are presented in this section. An analysis of performances by the proposed approaches and the popular edge detectors is also presented, followed by an introduction to the implementation of the hybrid method in the real-time application.

5.3.1 Experimental Results

Images were processed to compare the results from the revised Canny operator with those produced using typical edge detectors. As introduced in the previous section, the edges in cell images are usually blurred, so details are often lost during the segmentation process. An example is shown in Figure 5-2.

(a)　(b)　(c)　(d)
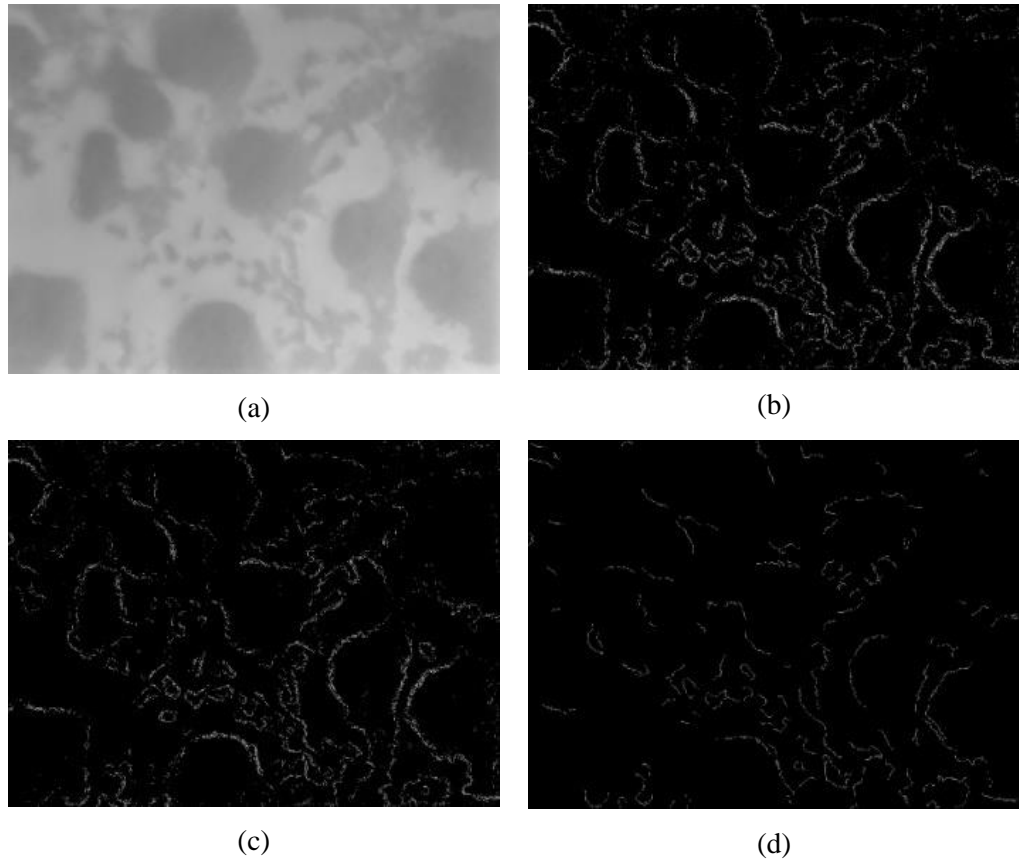
Figure 5-2 (a) Original image; (b) Result from Sobel; (c) Result from Prewitt; (d) Result from typical Canny

Since the typical Canny approach is sensitive to low image contrast, it loses more edges compared to the other methods. Hence, the cell image is first enhanced to make the edges sharp and clear before further processing—although this is at the cost of quality improvement, with the noise increased.

As shown in Figure 5-3, this process not only produces more details but also more noise. The problem changes from one of low contrast to that of increased noise; so a noise-insensitive edge-detection method is required.

(a)

(b)

(c)

(d)
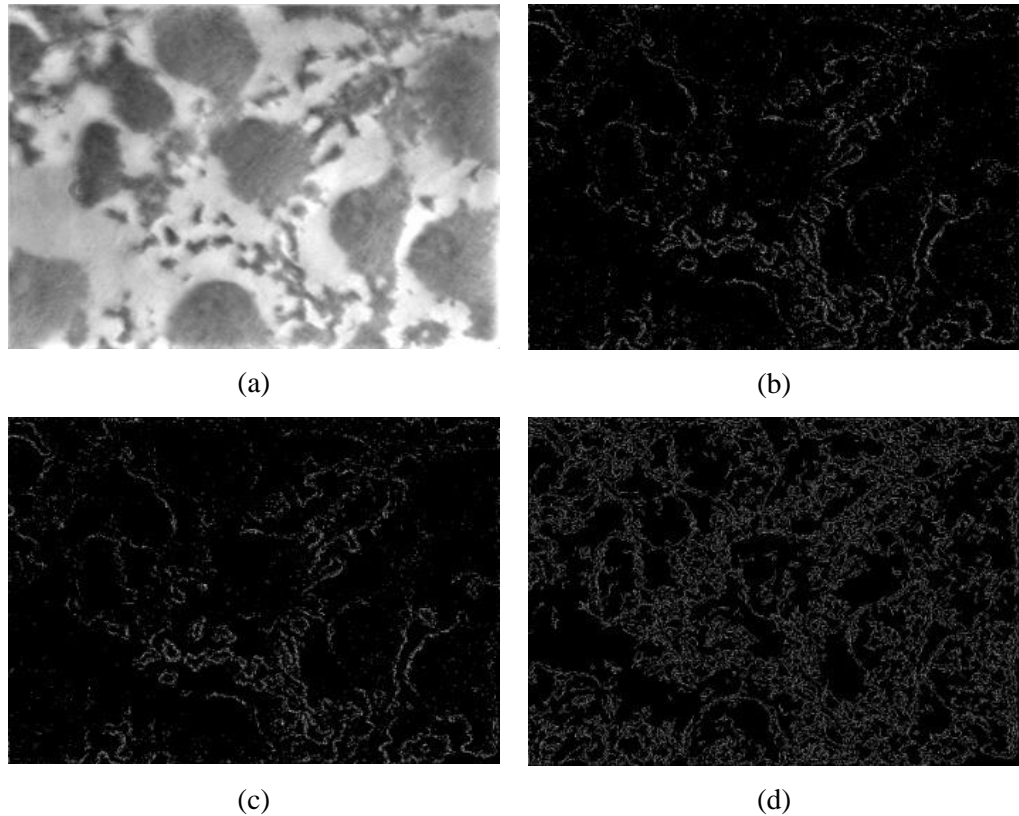
Figure 5-3 (a) Enhanced image; (b) Result from Sobel; (c) Result from Prewitt; (d) Result from typical Canny

The revised Canny method divides the image into sub-images that are individually processed to reduce the impact of the inhomogeneous distribution of grey scales. After image separation is achieved, the method calculates the histogram of gradient (HoG) of the processing sub-image. This is shown in Figure 5-4, where the x-axis represents the values of gradients and the y-axis is the number of points with each value of gradient.
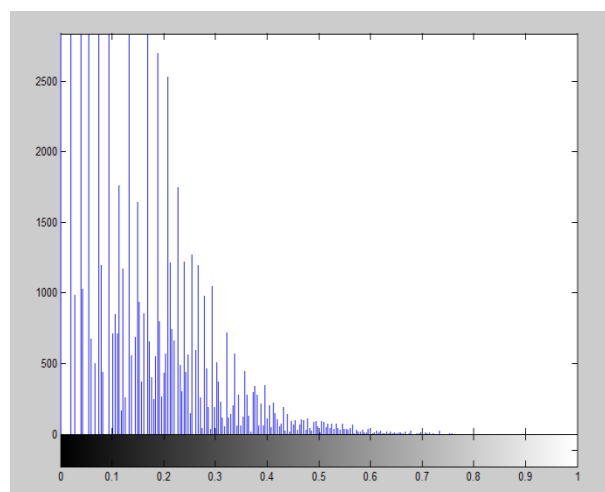
Figure 5-4 Histogram of gradients

The edges, which have high gradients, occupy only a small proportion of points in the image. Conversely, the points in the objects and background, along with those generated by noise, usually have a lower gradient. The problem is to find a value that ideally partitions the points in the HoG into correct classes, which is achieved using the theory of fuzzy entropy.

5.3.2 Comparison with benchmark algorithms

The proposed edge detector was applied to the cell images and its outcomes were compared to those produced by benchmarking algorithms, which are shown in Figure 5-5.

(a)

(b)

(c)

(d)
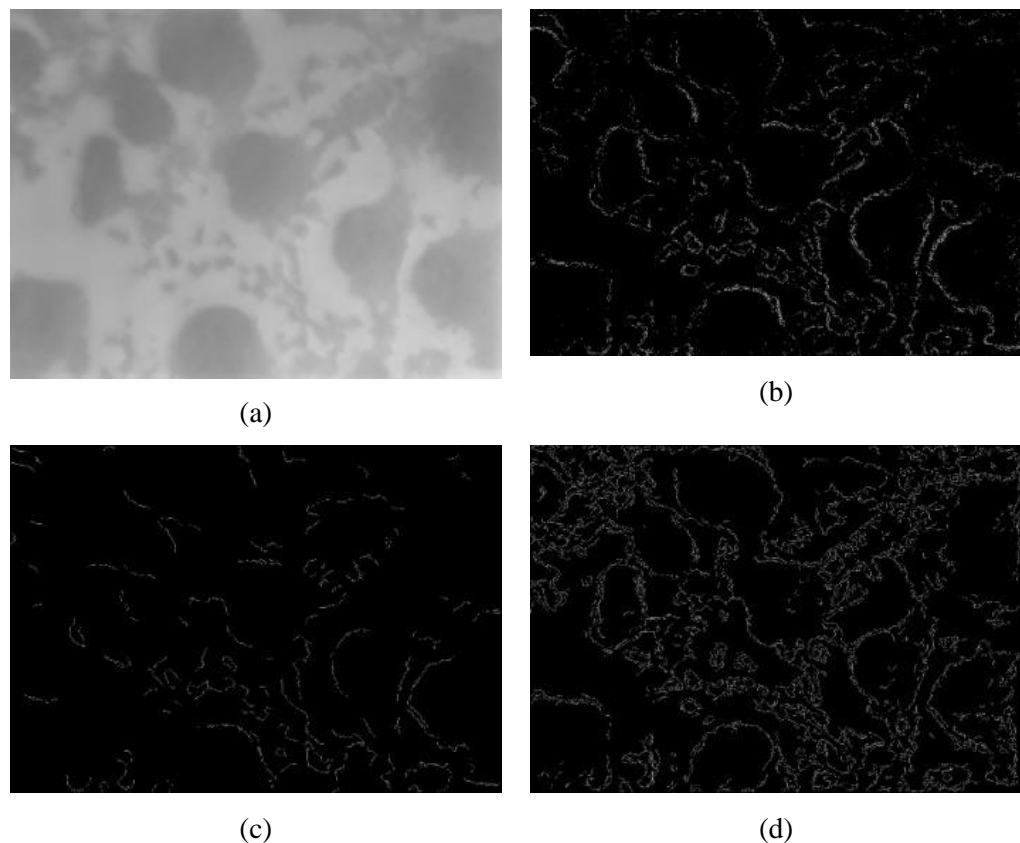
Figure 5-5 (a) Original image; (b) Result from Prewitt; (c) Result from typical Canny; (d) Result from the revised Canny

Due to the low quality of the cell images, there are unexpected problems in the results of the benchmarking methods. In the results produced using the typical Canny (Figure 5-5 (c)), many detailed edges are missed. Though the Prewitt operator (Figure 5-5 (b)) is better, many false edge points occur around the

edge lines and most of the main boundaries are not detected. These problems will definitely lead to difficulties in performing subsequent image analyses.

The proposed method (Figure 5-5 (d)) successfully deals with these problems. Even though the signal-to-noise ratio in the image is high—a problem that is increased even further after image enhancement—the revised Canny edge detector still exhibits an excellent segmentation performance, thus retaining much of the detailed information. It overcomes the three issues of low contrast, non-uniform grey scale distribution, and noise.

Furthermore, the proposed method has been implemented in a real-time system to process video data captured from a camera. The real-time system is established with a common personal laptop with the following hardware: CUP: Intel® Core™ i5-4200U @ 1.60GHz 2.30 GHz, RAM: 4 GB. The sampling rate of the system is set to 0.5 second/frame; thus, to successfully run the software, the processing speed of the hybrid edge detector is faster than the sampling rate, thus meeting the general requirement for real-time applications.

5.4 Fast tracking technique

The alterations of cells—their changing shapes and positions under different treatment conditions—can provide important information about biological mechanisms. Since manual analyses of these large datasets is extremely time-consuming, a large number of automatic tracking methods have been proposed in recent decades. These frameworks have been tested with images of various types of cells. For example, N. Ray uses the revised active contours method to track leukocytes [60]. X. Chen proposed an automatic tracking system exclusively for cancer cell nuclei in [67]. However, most of these existing frameworks exhibit outstanding performances only with specific databases, and the conditions required to produce excellent results are often strict. Complex parameter settings or sufficient prior knowledge may be required. The structures of the existing methods are mostly complex, which means that they may require a very large number of computations. Hence, few of these existing frameworks are applied in real-time applications.

Cell images differ from other types of images. Most datasets for biological applications exhibit the following core challenges. The contrast of the images is often low and the distribution of grayscales is often non-uniform. These low image conditions increase the difficulty of accurately separating target cells from the background. Cells in the same dataset have similar appearances and cells events such as rapid movement, mitosis and cell fusion must be accurately tracked. These factors increase the requirements on the tracking algorithm.

In this section, a fast tracking method for cells is presented that addresses all of these issues. It is a general framework for various types of cells. It can recognize cell behaviours across a time-lapse video, such as splitting, merging and entering. The performance of the system has been evaluated, and the result indicates that it is a good candidate for use in real-time applications.

5.4.1 Overview of tracking framework

To process a time-lapse series of frames, the proposed framework segments each image in the frame stack, then associates the same cells in the neighbour frames across the video. Hence, there are two core components of the tracking system: segmentation and tracking. Since prior research suggests that specific wavelet transform is robust to process biomedical data [101] the segmentation method used in this system is based mainly on the wavelet frames obtained by the transform. The tracking component achieves the cell association by using a newly defined parameter. The cell is classified to corresponding states according to the values of this parameter. The flowchart of the tracking system processing a single frame is presented below.
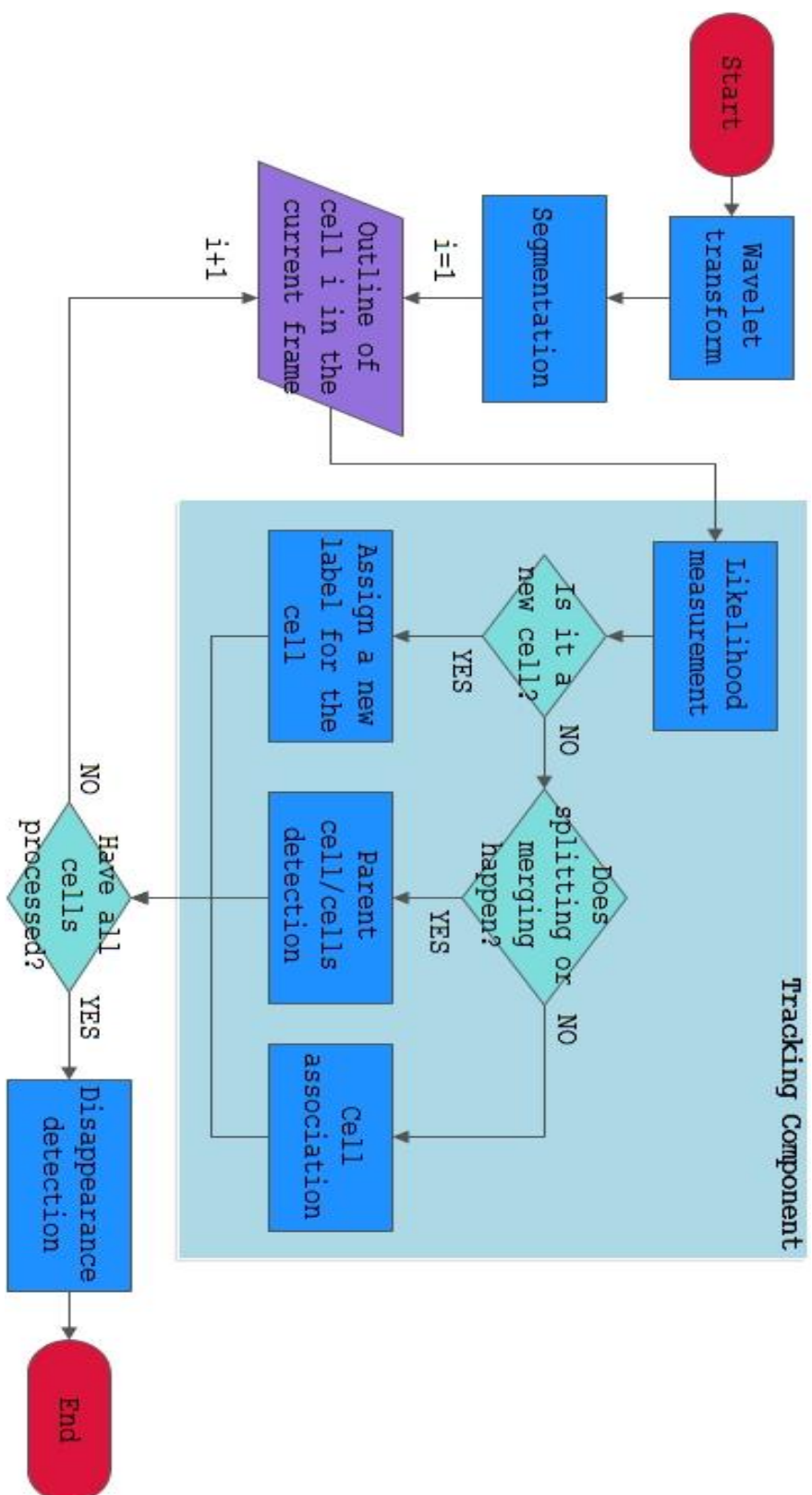
Figure 5-6 Flowchart of the tracking system for each cell in image

The new parameter used for the cell state classification is defined in the component of likelihood measurement. Since the system only uses one parameter to associate cells and recognize different cell behaviours including entering, splitting, and merging, compared to the existing ones, the structure of the tracking component has been obviously simplified. This flexible structure highly improves the processing speed of the system making it possible to be used in more practical applications.

5.4.2 Segmentation

The quality of the segmentation result is crucial to the following steps. However, the cell images are often in relatively high-resolution which will be extremely time-consuming for the traditional methods to process. To balance the problem between accuracy and processing speed, the framework first uses the wavelet transform to decompose the cell image and then uses the Otsu method to segment the generated wavelet frame.

5.4.2.1 Wavelet transform

Wavelet transform is a widely used technique in various fields of image processing, such as image compression and pattern recognition [102]. The 2-D discrete wavelet transform (2D DWT) is applied to produce the wavelet frames of the cell image before segmentation. A brief introduction of the transform is given in this section.

Assume an image as $I(x,y)$. To calculate the DWT of this 2-D signal, the image must be passed through a series of low-pass (g) and high-pass (h) filters. Because half of the frequencies in the signal are filtered, half of the signal can be removed, according to Nyquist's rule. Hence, the outputs from the filters are down-sampled by 2. The process can be represented as follows:
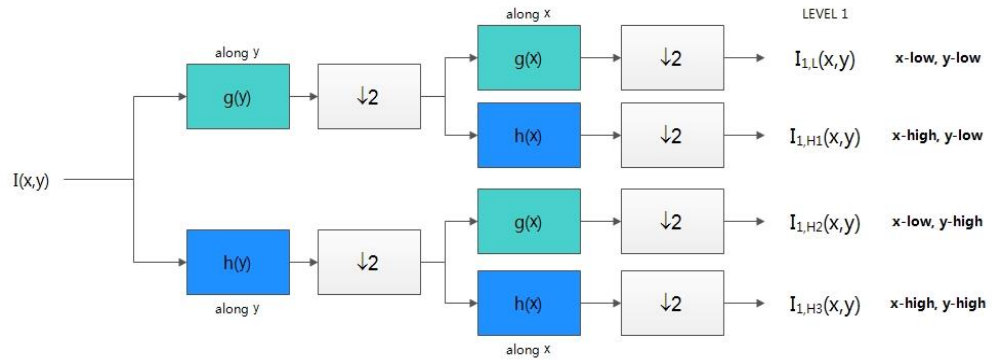
Figure 5-7 Process of the DWT

The outputs of the DWT provide both approximation coefficients and detail coefficients. The approximation coefficients are in the $I_{1,L}(x,y)$, and the other 3 sub-images mainly contain the detail coefficients according to different directions. Take a sample from the dataset as an example. The 4 filtered images are displayed below.

(a)   (b)
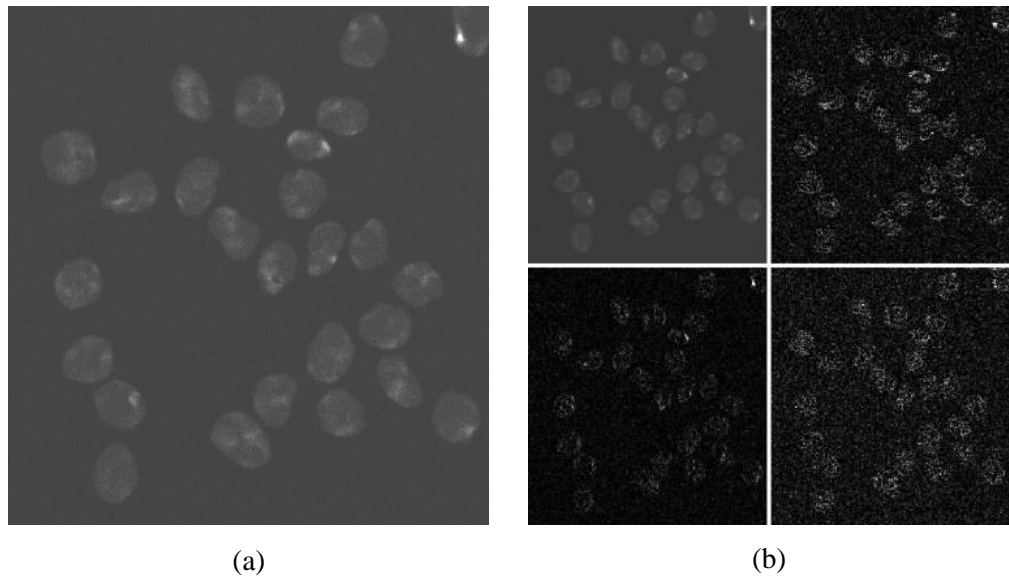
Figure 5-8 a) The original cell image. b) The 4 decomposed images. The two images in the first line are $I_{1,L}$ and $I_{1,H1}$, and the $I_{1,H2}$ and $I_{1,H3}$ are in the second line.

Due to subsampling, the cell image in high resolution is decomposed to 4 half-size sub-images. Since the approximation coefficients are mainly contained in the image from low-pass filters, the wavelet frame $I_{1,L}$ is used as an approximation of the original cell image in the segmentation step to reduce the workload of computations.

5.4.2.2 Segmentation using approximation sub-band

The segmentation method used in this proposed framework is based on the wavelet frame that contains the approximation coefficients. Due to the decreased image size of the wavelet frame, the system uses it as input instead of the original image to reduce the volume of computations. To reduce the influence of the non-uniform distribution of grayscales and low contrast, the method enhances the quality of the input wavelet frame by using top-hat and bottom-hat operations [14].

With these transforms, the bright and dark fields in the wavelet frame can be extracted and the overall contrast can be enhanced. The framework then implements the Otsu segmentation method [10] to disjoin the target cells from the background and produce the final segmentation results. Because the wavelet transform decomposed the original cell image, and because of the easily implemented design of the segmentation method, the time required for frame segmentation can be greatly reduced.

5.4.3 Tracking

After cell segmentation, the framework associates the same cell in adjacent frames by using a defined similarity function. The similarity function calculates the probabilities of correct associations, and all decisions about the status of cells—such as division and merging—are made based on the results of the function. Since only one parameter must be measured in the tracking process for each cell, the structure of the framework is simplified.

5.4.3.1 Similarity function

In the tracking step, the similarity between cells in neighbouring frames represents the probability of correct associations. Higher similarity means greater similarity. In the designed framework, two factors are taken to construct the similarity function: overlap factor and distance factor:

$$Similarity(S) = overlap\ factor(O) - distance\ factor(D) + offset \qquad (5.6)$$

where the *offset* is a pre-set positive number that is used to prevent the similarity from generating negative results.

Assume the two processing cells as $C_{i,t}$ in frame *t* and $C_{j,t+1}$ in frame *t+1*. The overlap factor reflects the degree of overlap between them. This factor varies between [0, 1] where *1* means totally overlapping and *0* means no overlap:

$$O_{i,j} = \frac{C_{i,t} \cap C_{j,t+1}}{min(C_{i,t}, C_{j,t+1})} \qquad (5.7)$$

where $C_{i,t} \cap C_{j,t+1}$ represents the size of the overlapping area between the two cells and $min(C_{i,t}, C_{j,t+1})$ is the minimum size of the two cells.

The overlap factor works for cells with slight displacements between frames. However, due to factors such as large cell volume or varying light conditions, the sampling rate of cell images in experiments may be lower than ideal that usually generates irregularly movements of cells in practical observation. It is therefore difficult for the framework to recognize using only an overlap factor. Hence, the distance factor is used to revise similarity results for cells with obvious movements:

$$D_{i,j} = \frac{D(C_{i,t}, C_{j,t+1})}{max(C_{i,t}, C_{j,t+1})} \qquad (5.8)$$

where $D(C_{i,t}, C_{j,t+1})$ is the Euclidean distance from the centre of gravity of cell $C_{i,t}$ to the centre of cell $C_{j,t+1}$, and $max(C_{i,t}, C_{j,t+1})$ is the maximum size of the two cells.

The similarity function is processed with each pair of cells in adjacent frames. Different decisions for the cell status can be made based on the similarity results.

5.4.3.2 Cell association

The main events for cell observation are cell movement, cell splitting and merging, cell entering and leaving. In the framework, the status of a cell can be recognized based on the results of the similarity function. Due to its simplified structure, the response time of the whole system is further improved.

The detail steps for the process of cell association can be concluded as follows:

1. Generates the look-up map of similarity.

2. Detects cell merging with the threshold (*Th1*).

3. Filters new entering cells with the threshold (*Th2*).

4. Uses the look-up map to link cells.

5. Detects cell splitting based on the results of cell-linking.

6. Marks the cells that have disappeared.

A. Look-up map of similarity

The framework generates a look-up map to represent the similarity between cells in adjacent frames. Assume that frame t contains N cells and that frame t+1 contains M cells. $S_{i,j}$ represents the similarity of cells $C_{i,t}$ and $C_{j,t+1}$. The similarity look-up map can be written as follows:

	$C_{1,t+1}$	$C_{2,t+1}$	…	$C_{M-1,t+1}$	$C_{M,t+1}$
$C_{1,t}$	$S_{1,1}$	$S_{1,2}$	…	$S_{1,M-1}$	$S_{1,M}$
$C_{2,t}$	$S_{2,1}$	$S_{2,2}$	…	$S_{2,M-1}$	$S_{2,M}$
…	…	…	…	…	…
$C_{N-1,t}$	$S_{N-1,1}$	$S_{N-1,2}$	…	$S_{N-1,M-1}$	$S_{N-1,M}$
$C_{N,t}$	$S_{N,1}$	$S_{N,2}$	…	$S_{N,M-1}$	$S_{N,M}$

Figure 5-9 Look-up map of similarity

B. Cell merging

With the generated map, the framework associates the cells in the current frame with those that have the highest similarity in the previous frame. Therefore, each cell in frame t+1 can be related only to one cell in the previous frame, which makes it difficult to identify cell mergers. To solve this problem, a detection method that employs cell similarities is proposed. The process of cell merging is shown in Figure 5-10.

(a)   (b)

(c)
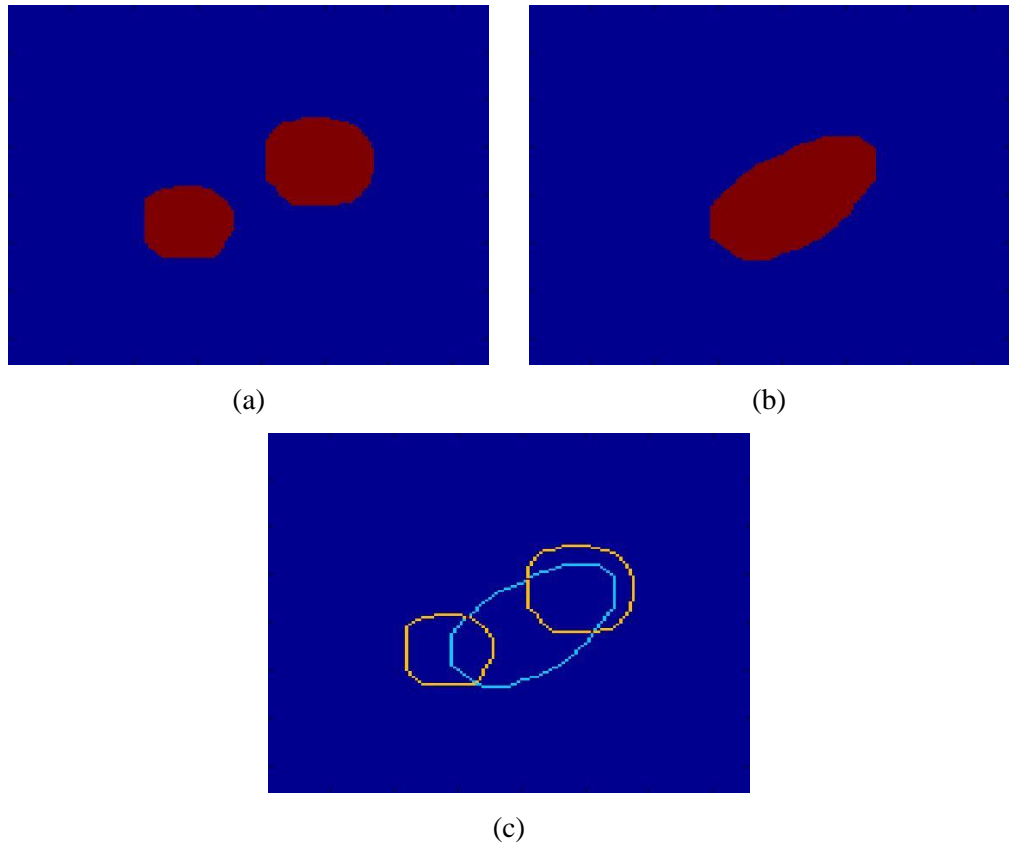
Figure 5-10 a) The cell in frame t. b) The cells after fusion in frame t+1. c) The boundaries of the cells by overlapping two frames.

The two cells—called $C_{x,t}$ and $C_{y,t}$, in Figure 5-10 (a)—merge into one cell, called $C_{z,t+1}$, in Figure 5-10 (b). By overlapping the boundaries of these three cells in Figure 5-10 (c), a large overlapping area is found between the parent cells and the generated cell that is due to the short time interval between adjacent frames. According to Eq. (5.6-5.8), the similarities, $S_{x,z}$ and $S_{y,z}$, are high in the look-up map for cell $C_{z,t+1}$. Therefore, assuming that N cells are contained in frame t, the event of a cell merging with cell $C_{z,t+1}$ in frame t+1 will be detected if its entry in the look-up map contains two or more

similarities and satisfies the following condition:

$$Cell\ merging\ happens, if\ S_{x,z} > Th1\ and\ S_{y,z} > Th1 \qquad (5.9)$$

where $1 \le x \le N$, and $1 \le y \le N$. Th1 is a pre-set threshold: i.e., 0.8.

C. Cell entering and cell movements

The new entering cells are filtered by a pre-set threshold (Th2) (i.e., 0.65) after cell merger is detected. The cell j in frame t+1 is detected as newly entering if the following condition is satisfied:

$$Newly\ Entering\ Cell, if\ \max_{1 \le k \le N}\left(S_{k,j}\right) < Th2 \qquad (5.10)$$

where *N* represents the number of cells contained in frame t.

Merging and newly entering cells are assigned to corresponding statuses and removed from the look-up map of similarity. The proposed framework then associates the cells in the current frame, t+1, with the cells with the highest similarities in frame t and generates an association map (AM) to record the association relationships.

D. Cell splitting and cell disappearing

Like the event of cell merging, there is a large overlapping area between the parent cell, called $C_{i,t}$, and the generated cells, called $C_{c,t+1}$ and $C_{h,t+1}$, in the event of cell splitting. Consequently, the similarities, $S_{i,c}$ and $S_{i,h}$, are relatively high, which links the generated cells ($C_{c,t+1}$ and $C_{h,t+1}$) to the same parent cell ($C_{i,t}$) in the association map (AM). Therefore, the event of cell splitting can be detected by checking the AM to see whether there are two or more cells in frame t+1 associated with the same cell in frame t.

With the detection of cell merging, cell entering, cell movements and cell splitting, all of the cells in the current frame, t+1, can be associated with cells in previous frame t. The framework then labels the cells with no links in previous frame as 'disappearance'.

5.5 Performance Evaluation for fast tracking

This section briefly introduces the dataset used in the experiments and the outcomes from the segmentation and tracking. These results show a high accuracy of both segmentation and tracking.

5.5.1 Introduction of the dataset

The experimental dataset was collected by the Centre for Biomedical Image Analysis (CBIA), Masaryk University of Brno, Czech Republic. The dataset contains 6 stacks of time-lapse microscope images and the trajectories of each cell in the database have been manually traced. The detail information of the dataset is listed in Table 5-1.

Table 5-1 Detail information of the dataset

	Sequence No.	Image Size	No. of Frames	Total No. of Cells
Simulated nuclei moving (SIM)	1	495×534	56	48
	2	569×593	100	59
	3	606×605	100	72
	4	673×743	56	97
	5	597×525	76	62
	6	655×735	76	112

The dataset is generated by simulations of moving cell nuclei. Each sequence contains more than 50 frames, and the average size of a frame is larger than 500×500. It is a huge volume of data for traditional tracking methods to process. Few of the existing methods perform very well either in terms of tracking accuracy or processing speed. To solve the problems, the proposed framework is evaluated with the dataset and an obvious improvement is achieved.

The accuracy of tracking of the framework is evaluated with the provided ground truth. If node M_i^t is the cell i in frame t in the sequence of ground truth, and if the links between nodes are labelled as edges E, then the evaluation system measures the number of cells not detected (false negatives, FN), the cells incorrectly detected (false positives, FP), the cells correctly

detected (true positives, TP), the split operations needed to correct the results (NS), the edges that must be removed (ED), the missing edges (EA) and the edges mismatching the track link and parent link (EC). The weighted sum of the number of operations required to transform the results to the ground truths can be defined as follows:

$$TRA_P = \omega_{NS}NS + \omega_{FN}FN + \omega_{FP}FP + \omega_{ED}ED + \omega_{EA}EA + \omega_{EC}EC$$

where the weights (ω) are defined manually according to the difficulties of making corresponding operations.

The TRA_P measure is normalized to the [0, 1] interval and is equal to zero when the results are identical to the ground truths. Then the accuracy of tracking can be measured by,

$$TRA = 1 - \frac{\min(TRA_P, TRA_E)}{TRA_E}$$

where $TRA_E = \omega_{FN}|M| + \omega_{EA}|E|$ is the cost of creating the ground truth graph.

5.5.2 Tracking result

The proposed tracking framework is based on the structure of segmentation and association. The system segments each frame in the sequence via the proposed segmentation method; it then associates the same cells in the adjacent frames and detects specific cell activities by measuring a newly defined parameter. An example of the tracking result is shown in Figure 5-11.

(a)

(b)

(c)

(d)
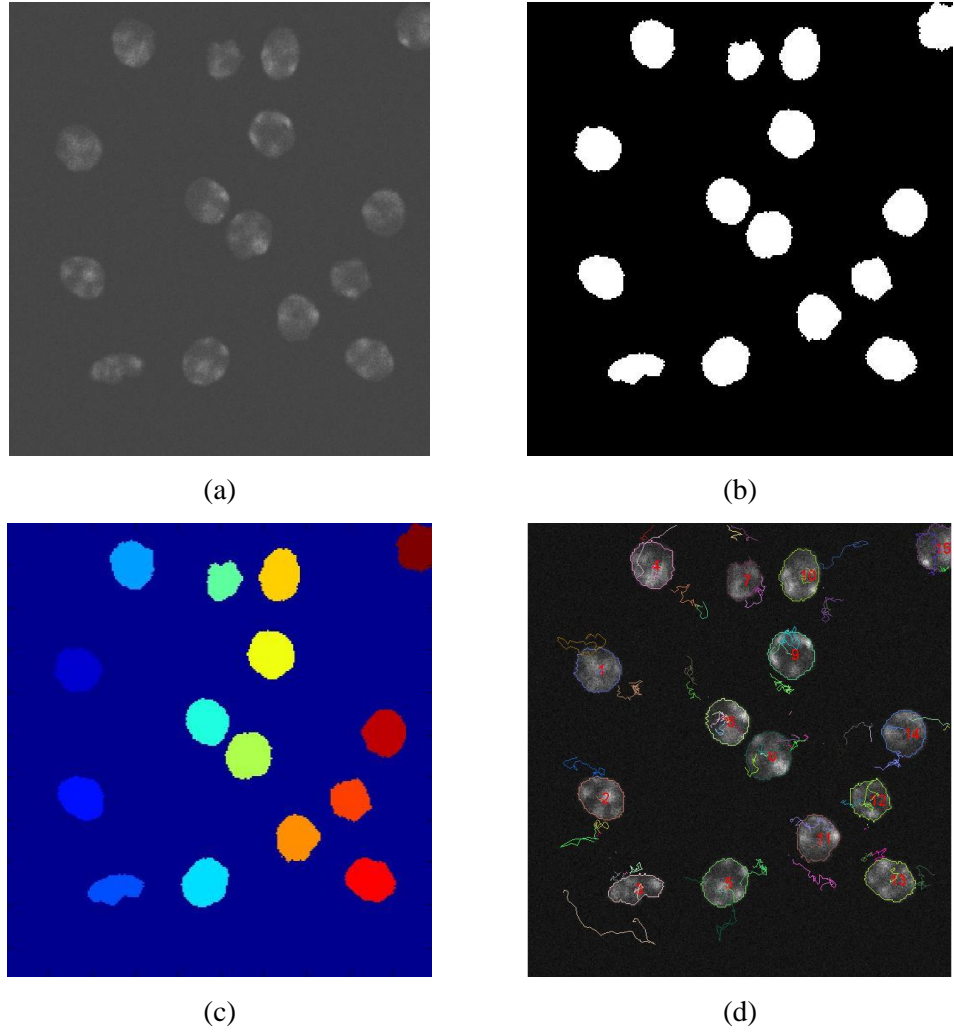
Figure 5-11 Example of the tracking result: a) the original cell image, b) the segmentation result, c) the tracking result by the proposed framework (the different colours represent the labels for the cells), and d) the trajectories of cells across the video.

Figure 5-11 (b) presents the segmentation results for the original cell image shown in Figure 5-11 (a). The framework uses the segmentation results to generate the look-up map of similarity between adjacent frames. Figure 5-11 (c) shows a result from the tracking component. The cells are tracked and labelled with markers of different colours. A final outcome from the tracking system is presented in Figure 5-11 (d). The trace lines in different colours represent the trajectories of different cells across the frame sequence.

The proposed framework processes the cell image at a high speed that is, at average, below one second per frame.

5.5.2.1 Evaluation of DWT with different decomposition levels

In the experiments, processing speed is found to have strong relationship with frame size and the total number of cells. If the time consumption of the proposed framework used to process each frame in the target sequence is $TIM_{per\ frame}$, the processing speed (V_P) (i.e., the number of frames processed by the framework in one second) can be presented as follows:

$$V_P = \frac{1}{TIM_{per\ frame}}$$

Table 5-2 lists the information of each dataset and the corresponding processing speed. The results are generated from the framework with the one-level wavelet transform.

Table 5-2 Comparison of the processing speed

SequenceNo.	1	2	3	4	5	6
Frame size	495×534	569×593	606×605	673×743	597×525	655×735
No. of Cells	48	59	72	97	62	112
Vp	2.43	2.63	2.22	0.7	2.81	1.38

The relationship between frame size and processing speed (V_P) is shown in Figure 5-12 (a). The red line represents the variation of V_P with frame size, which is represented with a blue line. Figure 5-12 (b) shows the variation of V_P (red line) according to different cell volumes (green line). From the presented relationships, both frame size and number of cells have a negative influence on processing speed. A larger frame or volume of cells leads to a greater workload for the system, which slows down the processing speed, as in sequence #4. Moreover, the quality of cell images contained in each of the sequence is also important for the processing speed, because the low image quality requires more operations in the pre-processing step, which increases the time consumption. Thus, the processing speed of this sequence is faster even though sequence #5 has a larger frame and contains more cells than #1 and #2.
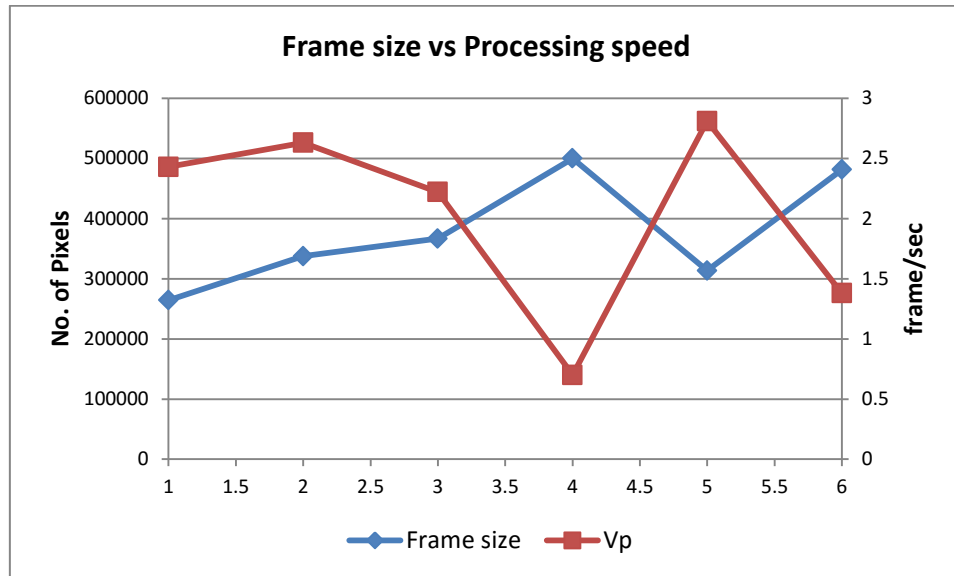
(a)
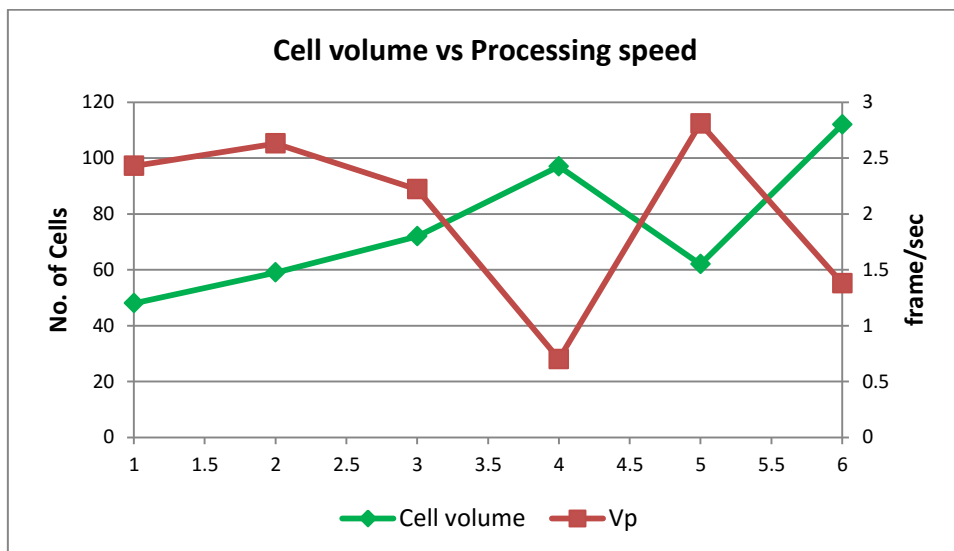
(b)

Figure 5-12 a) Variation of V_P with different fame size b) variation of V_P with number of cells.

<center>(a)   (b)</center>
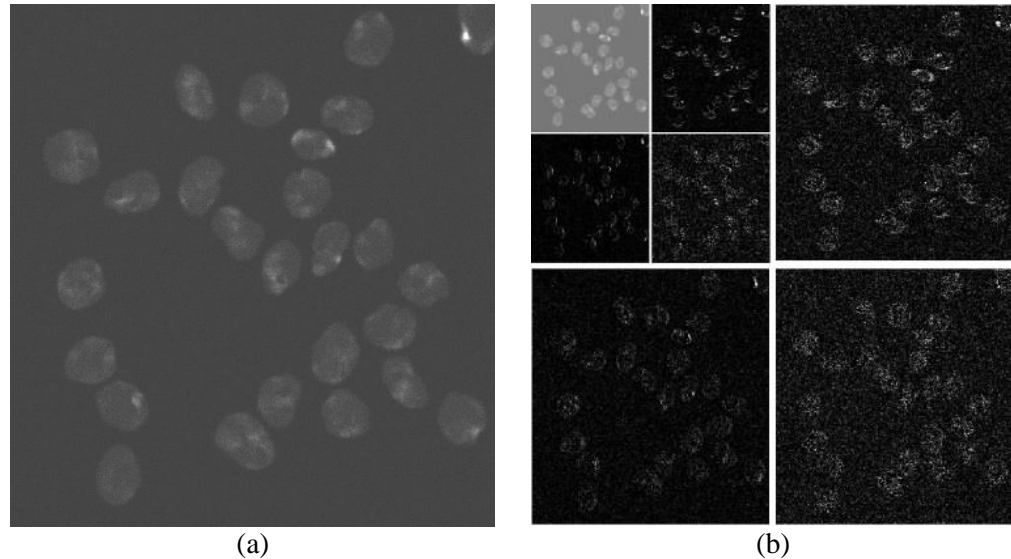
Figure 5-13 Wavelet transform in second layer: a) the original image, and b) the second layer wavelet decompositions.

We also applied a two-level wavelet transform for testing, which transfers the original cell image to a further small size. Due to the loss of more detailed information in the second-level wavelet sub-band, parts of the cells or small cells may be filtered out by the wavelet operation. Segmentation results of these wavelet sub-bands are likely, leading to errors in the tracking step.

The processing speed and tracking accuracy are compared for the frameworks that use different wavelet sub-bands and the framework that lacks wavelet transform in Table 5-3 and Table 5-4. The average processing speed is calculated by $\frac{\text{Total No.of frames}}{\text{Total TIM}}$.

Table 5-3 Comparison of the accuracy (%)

SequenceNo.	1	2	3	4	5	6	Average
Without WT	**99.89**	**99.28**	96.85	97.33	95.30	97.63	**97.71**
(1st Level)	99.18	98.37	**97.10**	**97.53**	**95.68**	**98.11**	97.66
(2nd Level)	91.28	96.49	96.15	97.32	94.61	97.58	95.57

Table 5-4 Comparison of the processing speed

SequenceNo.	1	2	3	4	5	6	Average
Without WT	0.53	0.34	0.52	0.18	0.72	0.27	0.36
(1st Level)	2.43	2.63	2.22	0.7	2.81	1.38	1.73
(2nd Level)	**2.8**	**2.7**	**3.03**	**1.6**	**4**	**2.05**	**2.56**

Comparison of Tracking Accuracy

(a)

Comparison of Processing Speed
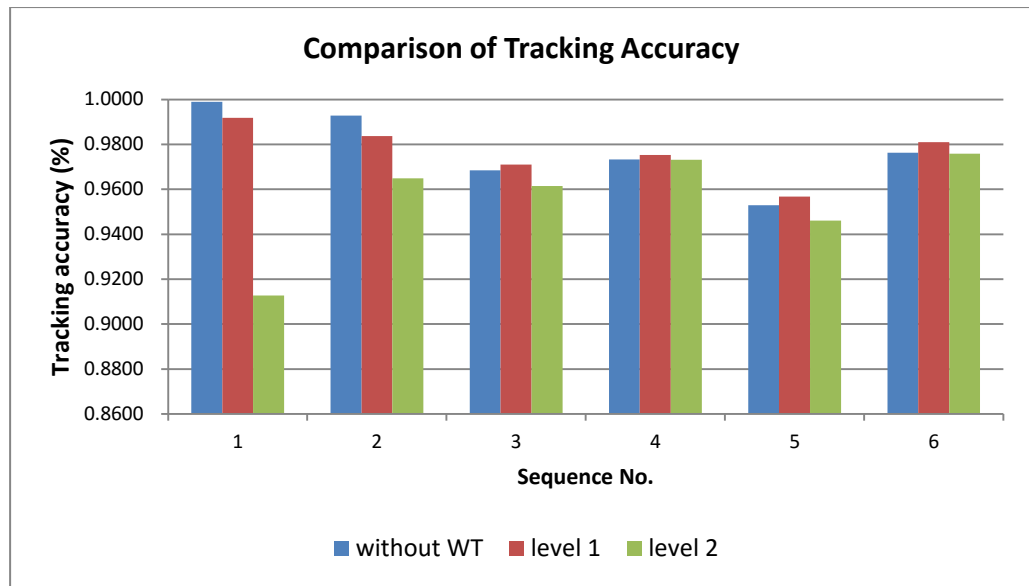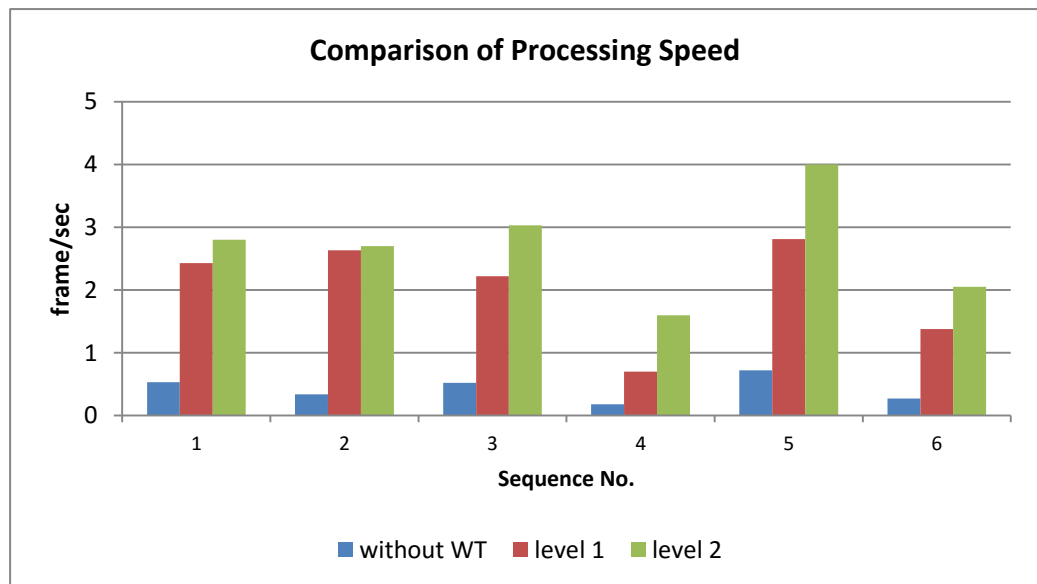
(b)

Figure 5-14 Bar charts for the tracking accuracy and processing speed

Figure 5-14 shows the accuracies and speeds of the frameworks for different microscopic sequences. For convenience of illustration, the framework without wavelets is denoted FWO. The framework with first-layer wavelets is denoted FW1, and the framework with the second-layer wavelets is denoted FW2. The FWO achieves the highest accuracies for sequences #1 and #2: i.e., 99.89% and 99.28%, respectively. FW1 provides the best performance for the rest sequences: i.e., 97.10%, 97.53%, 95.68%, 98.11% for sequences #3 through #6, respectively. Theoretically, detailed information and noise are contained in the high frequency sub-bands of the wavelet transform. Therefore,

though to abandon these sub-bands is to lose information, the noises are nevertheless simultaneously removed. Due to this trade-off issue, the differences in accuracy between FWO and FW1 are relatively small. However, FW1 outperforms FWO in terms of processing speed. As shown in Table 5-4, the average processing speed of FW1 (1.73) is about five times that of FWO (0.36).

FW2 improves the processing speed overall, but it causes a drop in tracking accuracy. The improvement in processing speed is more obvious with sequences that contain a large size frame and a large volume of cells. The ratio of improvement in sequence #4, for example, is 129% of FW1. The tracking accuracy of sequences with a small frame size and low volume of cells suffers from a loss of information caused by the wavelet transforms: e.g., a degradation of 8.61% for sequence #1 compared to FWO. Hence, processing speed and tracking accuracy are in a trade-off relationship. The use of the higher level wavelet should be according to the conditions of the processing sequence. High-throughput cell flow tracking provides a more efficient approach relative to high-resolution sequences.

5.5.2.2 Performance evaluation with benchmark methods

The methods stated in [4] from ISBI 2013 were tested as benchmarks for the proposed system. All of the methods are evaluated for tracking accuracy and processing speed. The results of tracking accuracy are presented in Table 5-5.

Table 5-5 tracking accuracy of different algorithms

Seq. No.	1	2	3	4	5	6	Average
COM-US	79.07	84.33	89.60	85.45	79.55	83.23	83.54
PRAG-CZ	90.96	87.69	90.06	92.03	73.93	84.63	86.55
KTH-SE	99.67	98.97	98.43	98.72	97.78	98.80	98.73
Proposed Method (one level wavelet)	99.18	98.37	97.10	97.53	95.68	98.11	97.66
Proposed Method (two level wavelet)	91.28	96.49	96.15	97.32	94.61	97.58	95.57

COM-US is a tracking framework designed by Compunetix Inc, USA, which employs the multiple-hypothesis tracking paradigm. PRAG-CZ is a

segmentation-and-association based tracking framework proposed by Charles University in Prague, Czech Republic. KTH-SE is also based on the segmentation-and-association scheme, which employs a greedy algorithm in its track-linking component to improve tracking performance. The average accuracy of the KTH-SE with SIM datasets is 98.73%, which is the best among four algorithms. The proposed tracking system with the one-level wavelet transform achieves the second position of average tracking accuracy: i.e., 97.66%, which is 1.07% lower than the KTH-SE.

The processing time (TIM) of these methods per frame for each of the experimental sequences was evaluated with a common desktop computer (Intel Core i5-4200U 2.3GHz, 4GB RAM). The results are presented in Table 5-6. The TIM is measured by the second.

Table 5-6 TIM of different algorithms

Seq. No	1	2	3	4	5	6	Average
COM-US	0.107	0.1	0.13	0.232	0.105	0.145	0.132
PRAG-CZ	0.768	0.92	1.01	1.464	0.895	1.290	1.043
KTH-SE	1.071	0.86	0.83	1.589	0.868	1.092	1.007
Proposed Method (one level wavelet)	0.411	0.38	0.45	1.429	0.355	0.724	0.578
Proposed Method (two level wavelet)	0.357	0.37	0.33	0.625	0.25	0.488	0.391

The average TIM is calculated by $\frac{\text{Total TIM}}{\text{Total No.of frames}}$. Due to its simple structure, the proposed framework with the one-level wavelet transform provides a processing speed of 0.578 sec/frame, which is 0.429 sec less than the KTH-SE.

5.6 Conclusion

This chapter introduced two automatic techniques to fast-process cell images. The hybrid edge detector based on fuzzy entropy and the Canny operator was presented first. The performance of the approach is assessed with other benchmark methods. The hybrid edge detector has been implemented for

visual data captured by a common camera. It will be employed to monitor cells in real-time in further research.

The fast tracking framework designed for time-lapse cell videos was introduced next. This framework is based on segmentation and association. Wavelet transform was implemented to choose a suitable balance between tracking accuracy and processing speed, and a novel cell similarity function was defined for cell association. An evaluation of its performance was also presented which shows that the proposed tracking framework excellently balances the trade-off relationship between tracking accuracy (i.e., 97.66%) and processing speed (i.e., 0.578 sec/frame).

Chapter 6   Concluding Remarks

This chapter provides a summary of the previously presented research, the issues encountered and the achievements of this thesis. It concludes with a proposal for further studies.

6.1 Contributions

This thesis began with a review of literature on image-processing techniques, including segmentation, tracking and 3-D reconstruction. Improved frameworks were established using these automatic processing techniques. Five primary techniques were presented in the thesis.

1. The hybrid segmentation method using both global and local-thresholding techniques

Microscope images of cell filopodia contain a lot of useful information for biological studies. However, few of existing segmentation approaches can accurately extract this information due to the typically low quality of cell images. A hybrid segmentation method has been proposed that is based on both

global and local-thresholding techniques that are designed especially to detect detailed information. This approach overcomes the core challenges shared by most cell images and exhibits excellent performance in the extraction of cell filopodia.

The novel segmentation method uses both global and local-thresholding techniques to segment cell images. The two techniques are combined because problems occur when the techniques are used individually. Local thresholding leads to fragmentation of generated results, and global thresholding fails to recognize cell filopodia. Together, however, the two techniques solve each other's problems; hence, their combination can produce more accurate results.

The performances of the proposed method and some popular segmentation approaches were tested with real cell dataset. The results demonstrate that the proposed method exhibits excellent performance in segmentation (i.e., 49.66%). It outperforms the other benchmarking approaches.

2. The framework for quantitative measures of cell features

Cell monitoring is a typical challenge for biological studies. Since the acquired databases are usually large, manual monitoring becomes extremely laborious. To improve efficiency, a powerful and non-destructive cell-monitoring system is proposed to measure the alterations of important cell features: e.g., cell size and cell shape.

Unlike some traditional methods that use fluorescent markers, the input for the proposed system is a set of cell images in grey scales. This ensures that no additional factor is introduced to the research and that cells are not harmed. Three features are quantitatively measured in the proposed system: cell area, cell volume and cell shape. Various image-processing techniques are employed in the framework to perform different tasks. An image-segmentation algorithm is used to calculate cell adhesion area and cell size, and a phase reconstruction technique is used to calculate cell volume. Based on these two outcomes, measurements of cell shape can be performed.

The proposed cell feature measuring framework has been applied to the real cell dataset captured by the University of Nottingham, United Kingdom. The experimental result is verified by the prediction made by biologists.

3. The tracking framework using multiple extracted cell features

Automatic analyses of cell image sequences can offer efficient statistical measures that are difficult for manual analysis. A generalized framework for automatic cell tracking with various datasets is presented in this thesis. Although many approaches have been proposed for the tracking task, most are in complicated structures and require many parameters or prior-knowledge. The designed framework is general and is easily extended to databases under different image conditions. This general approach is not restricted to tracking particular types of cells. Indeed, it can be applied extensively in various medical imaging applications.

Since the proposed tracking framework is based on an advanced version of the traditional segmentation-and-association algorithm, an analysis of the features of cells is made before establishing the framework. The analysis aims to evaluate the features that can best assist the cell-association process. The tracking approach uses these features to calculate the similarity between cells in adjacent frames. A scoring scheme is proposed for the system to make cell associations. A revised approach to detecting splitting, merging and appearing is presented. The method perfectly solves the errors in the typical method that are caused by rapid cell movements. A 2-step thresholding algorithm is also included in the proposed framework. The method can accurately segment the cell images. It achieves a segmentation accuracy of 85.18% for mouse stem cells.

The developed framework has been applied to four datasets that contain different type of cells. These databases were provided by different institutions at a world-wide scale. The accuracy of the tracking system is demonstrated to be 92.93% using manually track-grounded truths. Furthermore, the proposed system successfully tracks cells with sharp movements that are difficult for older methods. The experimental results demonstrate the effectiveness of the

designed framework and its potential to assist in relevant medical studies.

4. The hybrid edge detector based on fuzzy entropy and the Canny operator

An edge detector has been introduced that is suitable for cell images based on the Canny operator and the fuzzy entropy theory. Due to the routine problem of low contrast in cell images, the method first enhances image quality by morphological operations. However this process introduces noise into the image and so requires the use of a robust edge detector. Widely used existing edge-detection methods were tested, and shortcomings of benchmarking methods were found. For example, most of them are sensitive to noise and are unable to deal with the problem created by inhomogeneous grey scale distribution.

Among the existing detectors, the Canny operator was selected as a method with high potential. Therefore, it was revised to use fuzzy entropy theory to improve its performance in the presence of noise. Entropy is a measure of the volume of information that is contained in a message. The larger the entropy is, the more detailed information retained. So gradient maximizing is achieved by using fuzzy entropy to provide the threshold for the Canny operator.

Through comparisons between the proposed method and others such as Prewitt and typical Canny operator, it was observed that the revised Canny edge detector is more robust with respect to noise and achieves better detail recognition. The proposed approach is a better for edge detection in cell images and has potential for related cell researches.

5. The fast tracking framework for time-lapse cell images

Automatic cell tracking reduces the workload and increases the accuracy of tracking over the manual approach. However, it is hard to apply most existing tracking frameworks in real-time applications due to their complicated structure. A fast and powerful tracking framework for cell datasets is introduced to address this issue.

The primary principal of the proposed framework is also the segmentation and association; however, each component of the framework is designed with a different approach than the previously introduced tracking system. Wavelet transform is used in segmentation components to decompose original cell images. The filtered wavelet frame is set at a lower resolution that is easier for the system to process. A novel cell similarity framework is defined for the tracking process. Events such as cell division, cell fusion, cell entering and cell disappearing can be detected based on the values of the similarity. The design of the proposed approach is general, which means that it can be extended to track various types of cells in different medical applications.

This approach has been applied to the real cell database. The generated results were evaluated with manually tracked ground truths. The tracking accuracy of the framework is 97.66%, and the average time for processing one frame is 0.578 sec. All of the simulations were completed on a common desktop (Intel Core i3-2100 3.1GHz, 4GB RAM), which verifies the effective performances of the proposed framework in fast cell tracking and indicates its great potential in real-time biological analyses.

6.2 Future Direction

The research presented in this thesis can serve as a starting point for further computational investigations. First, the extracted features can be extended to assist with more specific analyses that monitor the life cycles of cells. Second, the proposed segmentation approach must still address the problem created by the segmentation of overlapping cells. This issue is worth further investigation. Third, the proposed algorithms—both of segmentation and visual tracking—can be employed as a starting point for new research directions: for example, for the visual tracking of cars for traffic-monitoring systems.

In this thesis, an automatic monitoring framework for cells is proposed. The framework is able to perform cell feature extraction, cell edge detection and cell tracking. To further develop the system, more complex mechanisms can be included. The possible extensions are identified in what follows.

1. Pattern Recognition

Different cells often have distinct features, and the features of cells alter with respect to different states in their life cycles. Therefore, pattern recognition can recognize the kind or the state of cells by using extracted cell features. In future work, this extension can be employed to detect cells with pathological changes and thereby aid disease diagnosis.

2. Fast tracking for high-throughput cell flows

The tracking of high-throughput cell flows is a major issue in biological studies. There are often hundreds of cells in high-throughput datasets. Although approaches have been proposed to accurately track cells in high-throughput flows, few take processing speed into account. Thus, the implementation of fast tracking for high-throughput cell flows can further improve the efficiency of the system.

3. Real-time monitoring system

This research primarily contributes high-performance algorithms that are supposed to be implemented in the microscopic system in future work. A real-time monitoring system that can fast-extract cell features, track cells, and recognize cell states and cell behaviours is extremely useful for most biological analyses.

6.3 Conclusion

Because a growing number of biological analyses rely on automatic mechanisms, the performances of the techniques employed have gained the increasing attention of developers; however, most existing approaches perform lower than expected. Several automatic techniques that have been developed to process time-lapse microscope images are proposed in this thesis. In Chapter 3, a novel segmentation method and a framework for feature extractions are described. Analysis of their performances is presented with the cell dataset from the University of Nottingham, United Kingdom as a case

study. The work about the newly designed tracking framework using the extracted features to perform accurately tracking of cells is presented in Chapter 4. Our success at tracking cells with rapid movements demonstrates the outstanding performance of the proposed framework. Chapter 5 investigates fast-processing techniques for time-lapse microscope images. Two fast-processing techniques for different tasks—edge detection and tracking—were introduced and evaluated with respect to existing popular approaches. The fast-and-accurate performances of the two proposed approaches show their great potential for implementation in real-time applications.

In conclusion, a monitoring framework has been successfully established based on the aims and objectives stated in Section 1.2. This system can quantitatively measure features of cells and accurately track cells with an accuracy of over 90%. The tracking frameworks designed in this research are all established upon the structure of segmentation and association. The advantage of this structure is its excellent extendibility that makes the frameworks can be divided to separated components and adapted to different datasets. Finally, the presented evaluation results demonstrate that the system is an efficient tool for the analysis of cells that can provide aids for many relevant biological studies.

Appendix

The prototype of the designed tracking system has been evaluated in the Challenge section of 2014 IEEE International Symposium on Biomedical Imaging. The result of performance evaluation can be found at,

http://www.codesolorzano.com/celltrackingchallenge/Cell_Tracking_Challenge/Results_Second_CTC.html.

Some of the datasets provided by the organizers of the Challenge program are used in this research. Detailed information about them is presented in the following.
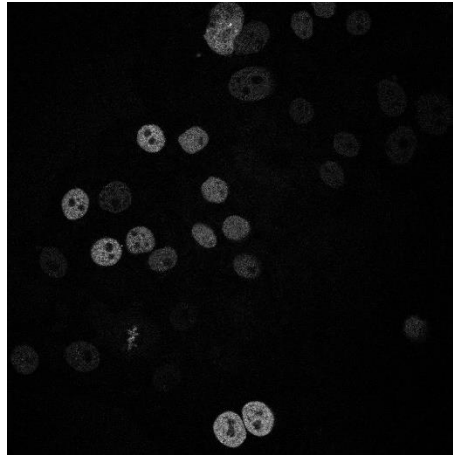
1. Rat mesenchymal stem cells on a flat polyacrylamide substrate (2D)
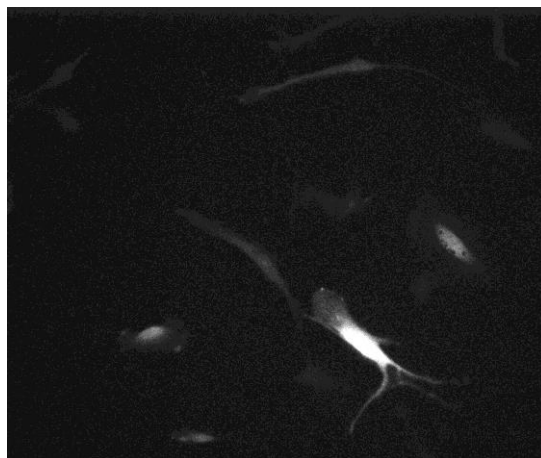
Provider: Dr. F. Prósper.
Cell Therapy laboratory, Centre for Applied Medical Research (CIMA)
Pamplona. Spain

Microscope: PerkinElmer UltraVIEW ERS
Objective lens: Plan-Neofluar 10x/0.3 (Plan-Apo 20x/0.75)
Pixel size (microns): 0.3 x 0.3 (0.3977 x 0.3977)
Time step (min): 20 (30)

2. GFP-GOWT1 mouse stem cells (2D)

Provider: Dr. E. B ártov á
Institute of Biophysics, Academy of Sciences of the Czech Republic. Brno. Czech Republic

Microscope: Leica TCS SP5
Objective lens: Plan-Apochromat 63x/1.4 Oil
Pixel size (microns): 0.240 x 0.240
Time step (min): 5

3. Simulated nuclei moving on a flat surface (2D)
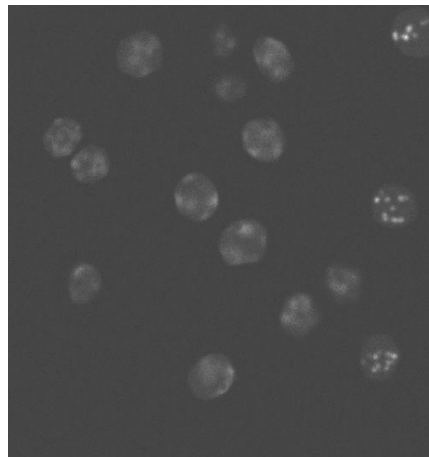
Provider: Dr. V.Ulman and Dr. D. Svoboda.
Centre for Biomedical Image Analysis (CBIA), Masaryk University. Brno. Czech Republic
(Created using Cytopacq)

Pixel size (microns): 0.125 x 0.125

4. Chinese Hamster Ovarian (CHO) nuclei overexpressing GFP-PCNA (3D)
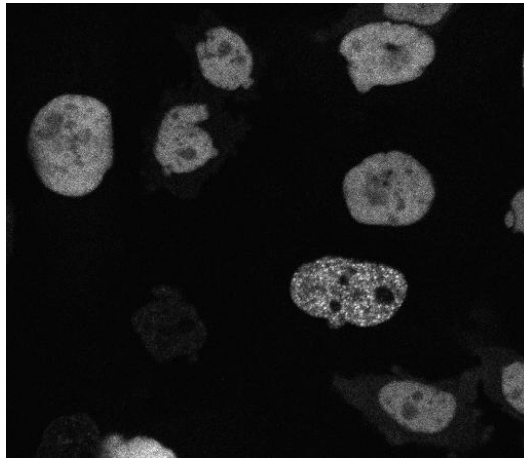
Provider: Dr. J. Essers.
Dept. of Cell Biology, Erasmus Medical Centre. Rotterdam. The Netherlands

Microscope: Zeiss LSM 510
Objective lens: Plan-Apochromat 63x/1.4 Oil
Voxel size (microns): 0.202 x 0.202 x 1
Time step (min): 9.5

5. HeLa cells stably expressing H2b-GFP (2D)

Provider: Mitocheck Consortium

Microscope: Olympus IX81
Objective lens: Plan 10x/0.4
Pixel size (microns): 0.645 x 0.645
Time step (min): 30

6. Simulated nuclei of HL60 cells stained with Hoescht (2D and 3D)
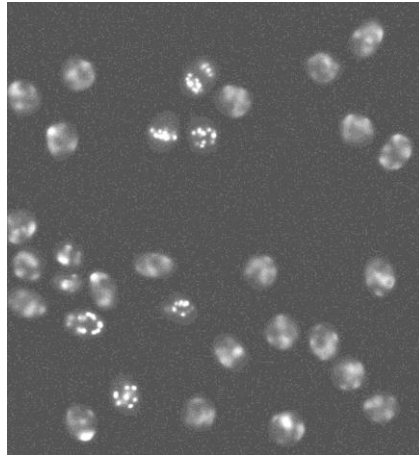
Provider: Dr. V.Ulman and Dr. D. Svoboda.
Centre for Biomedical Image Analysis (CBIA), Masaryk University. Brno. Czech Republic
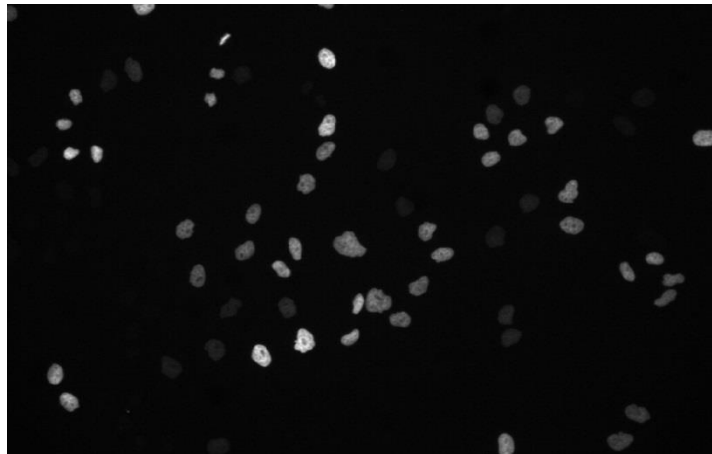(Created using Cytopacq)

Microscope: Zeiss Axiovert 100S with a Micromax 1300-YHS camera
Objective lens: Plan-Apochromat 40X/1.3 (oil)
Pixel size (microns): 0.125 x 0.125 (x 0.200)
Time step (min): 29

REFERENCES

[1]   SHEN, T. and Z. FANG, *Digital-image processing and Pattern Recognition*. 2005, Beijing: BEIJING INSTITUTE OF TECHNOLOGY PRESS.

[2]   Zimmer, C., et al., *Segmentation and Tracking of Migrating Cells in Videomicroscopy with Parametric Active Contours: A Tool for Cell-Based Drug Testing*. IEEE Transactions on Medical Imaging, 2002. **21**(10): p. 1212-1221.

[3]   LI, J., *Experimental Hematology*. 1997, Shanghai: Shanghai Science and Technology Press.

[4]   Maska, M., D. Svoboda, and etc, *A benchmark for comparison of cell tracking algorithms*. Bioinformatics, 2014. **30**(11): p. 1609-1617.

[5]   Haris, K. and etc, *Hybrid images segmentation using watersheds and fast region merging*. IEEE Transactions on Image Processing, 1998. **7**(12): p. 1684-1699.

[6]   Montell, D.J., *Morphogenetic cell movements: Diversity from modular mechanical properties*. Science, 2008. **322**(590): p. 1502-1505.

[7]   Meijering, E., *Cell Segmentation: 50 Years Down the Road [Life Sciences]*. IEEE Signal Process. Mag., 2012. **29**(5): p. 140-145.

[8]   YU, J., *The segmentation method for blood cell images using the thresholding*. Gan su Science and Technology, 2009. **25**(12): p. 70-73.

[9]   WANG, X., *Advanced Image Processing Technology*. 2000, Beijing: Science and Techonlogy of China press.

[10]   Otsu, N., *A threshold selection method from gray-level histograms*. IEEE Transactions on Systems, Man, and Cybernectics, 1979. **9**(1): p. 62-66.

[11]   LUO, X. and J. TIAN, *Survey on the Methods of Image Segmentation*. Pattern Recognition and Artificial Intelligence, 1999. **9**(3): p. 300-312.

[12]   Kittler, J. and J. Illingworth, *Minimum Error Thresholding*. Pattern Recognition, 1986. **19**(1): p. 41-47.

[13]   Cheriet, M., J.N. Said, and C.Y. Suen, *A recursive thresholding technique for image segmentation*. IEEE Transactions on Image Processing, 1998. **7**(6): p. 918-921.

[14]   Ye, D., Y. Zhao, and D. Li, *Local contrast enhancement of the medical image based on multiscale morphology*. CHINESE JOURNAL OF CLINICAL REHABILITATION, 2006. **10**(45): p. 200-202.

[15]   MA, B., L. QIAO, and Y. JIA, *Cell image segmentation method based on partial adaptive thresholds*. Application Research of Computers, 2009. **26**(2): p. 755-756.

[16]   Ayala, H.V.H., et al., *Image thresholding segmentation based on a novel beta differential evolution approach*. Expert Systems with Applications, 2015. **42**(4): p. 2136-2142.

[17]   MA, S., et al., *Improved otsu image segmentation algorithm based on two-dimensional histogram*. Journal of Northwest Normal University (Natural Science), 2009. **45**(1): p. 57-61.

[18]   Kumar, S., M. Pant, and A.K. Ray. *Segmentation of CT Lung Images Based on 2D Otsu Optimized by Differential Evolution*. in *the International Conference on Soft Computing for Problem Solving*. 2011. India: Springer India.

[19]   Kumar, M. and R. Saxena, *ALGORITHM AND TECHNIQUE ON VARIOUS EDGE DETECTION: A SURVEY*. Signal and Image Processing An International Journal, 2013. **04**(03).

[20]   Canny, J., *A computational approach to edge detection*. IEEE Transactions on Pattern Anal. Machine. Intell., 1986. **PAMI-8**: p. 679-698.

[21]   Elder, J.H. and S.W. Zucker, *Local scale control for edge detection and blur estimation*. IEEE Transactions on Pattern Anal. Mach. Intell., 1998. **20**(7): p. 699-716.

[22]   LI, S.Z., *Closed-form solution and parameter selection for convex minimization-based edge preserving smoothing*. IEEE Transactions on Pattern Anal. Mach. Intell., 1998. **20**(9): p. 916-932.

[23]   Ding, L. and A. Goshtasby, *On the Canny edge detector*. Pattern Recognition, 2001. **24**(721-725).

[24]   Medina-Carnicer, R., et al., *A novel method to look for the hysteresis thresholds for the Canny edge detector.* Pattern Recognition, 2011. **44**(6): p. 1201-1211.

[25]   Aruna, N.S. and S. Hariharan, *Edge Detection of Sickle Cells in Red Blood Cells.* International Journal of Computer Science and Information Technologies, 2014. **5**(3): p. 4140-4144.

[26]   ZHANG, X., K. YANG, and B. HAO, *Cell-Edge-detection method Based on Canny Algorithm and Mathematical Morphology*, in *3rd International Congress on Image and Signal Processing*. 2010: Yantai.

[27]   Serra, J. and P. Soille, *Mathematical Morphology and Its Applications to Image Processing*. 1994: Springer Netherlands.

[28]   ZHANG, S., et al., *A Survey of Microscopic Medical Image Segmentation.* Chinese Journal of Biomedical Engineering, 2007. **26**(4): p. 623-629.

[29]   Nipon, T.U., *White blood cell segmentation and classification in microscopic bone marrow images.* Lecture Notes in Computer Science, 2005. **3614**: p. 787-796.

[30]   Vincent, L. and P. Soille, *Watersheds in digital spaces: an efficient algorithm based on immersion simulations.* IEEE Transactions on Pattern Analysis and Machine Intelligence, 1991. **13**(6): p. 583-598.

[31]   CONG, P.-s. and J.-z. SUN, *Application of Watershed Algorithm for Segmenting Overlapping Cells in Microscopic Image.* Journal of Image and Graphics, 2006. **11**(12): p. 1781-1784.

[32]   Anoraganingrum, D., *Cell segmentation with median filter and mathematical morphology operation*, in *International Conference on Image Analysis and Processing*. 1999, IEEE: Venice. p. 1043-1046.

[33]   Chanda, B., M.K. Kundu, and Y.V. Padmaja, *A MULTI-SCALE MORPHOLOGIC EDGE DETECTOR.* Pattern Recognition, 1998. **31**(10): p. 1469-1478.

[34]   Chanho, J. and K. Changick, *Segmenting clustered nuclei using H-minima transform-based marker extraction and contour parameterization.* IEEE transactions on bio-medical engineering, 2010. **57**(10): p. 2600-2604.

[35]   Sharif, J.M., et al., *Red Blood Cell Segmentation Using Masking and Watershed Algorithm: A Preliminary Study*, in *2012 International Conference on Biomedical Engineering*. 2012, IEEE: Penang. p. 258-262.

[36]   Heimann, T., et al., *A Shape-Guided Deformable Model with Evolutionary Algorithm Initialization for 3D Soft Tissue Segmentation.* Lecture Notes in Computer Science, 2007. **4584**: p. 1-12.

[37]   Kass, M., A. Witkin, and D. Terzopoulos, *Snakes: Active contour models.* International Journal of Computer Vision, 1988. **1**(4): p. 321-331.

[38]   XU, C. and J.L. Prince, *Gradient Vector Flow: A New External Force for Snakes.* IEEE Transactions on Image Processing, 1998. **7**(3): p. 359-369.

[39]   Rajendran, A. and R. Dhanasekaran, *A hybrid method based on fuzzy clustering and active contour using GGVF for brain tumor segmentation on MRI images.* European Journal of Scientific Research, 2011.

[40]   Zhang, F., et al., *Contour extraction of gait recognition based on improved GVF Snake model.* Computers and Electrical Engineering, 2012. **38**(4): p. 882-890.

[41]   Cohen, L.D., *On active contour models and balloons.* CVGIP: Image Understanding, 1991. **53**(2): p. 211-218.

[42]   Liu, H.T., T.W.H. Sheu, and H.H. Chang, *Automatic segmentation of brain MR images using an adaptive balloon snake model with fuzzy classification.* Medical and Biological Engineering and Computing, 2013. **51**(10): p. 1091-1104.

[43]   Caselles, V., R. Kimmel, and G. Sapiro, *Geodesic Active Contours.* International Journal of Computer Vision, 1997. **22**(1): p. 61-79.

[44]   Kichenassamy, S., et al., *Conformal curvature flows: From phase transitions to active vision.* Archive for Rational Mechanics and Analysis, 1996. **134**(3): p. 275-301.

[45]   Bergeest, J.-P. and K. Rohr, *Efficient globally optimal segmentation of cells in fluorescence microscopy images using level sets and convex energy functionals.* Medical Image Analysis, 2012. **16**(7): p. 1436-1444.

[46]   Dzyubachyk, O., W. Niessen, and E. Meijering, *Advanced level-set based multiple-cell segmentation and tracking in time-lapse fluorescence microscopy images*, in *5th IEEE International Symposium on Biomedical Imaging: From Nano to Macro*. 2008, IEEE: Paris. p. 185-188.

[47]   Zhang, K., et al., *Active contours with selective local or global segmentation: A new formulation and level set method.* Image and Vision Computing, 2010. **28**(4): p. 668-676.

[48]   Li, C., et al., *Distance Regularized Level Set Evolution and Its Application to Image Segmentation.* IEEE Transactions on Image Processing, 2010. **19**(12): p. 3243-3254.

[49]   Wan, S.Y. and W.E. Higgins, *Symmetric region growing.* IEEE Transactions on Image Processing, 2003. **12**(9): p. 1007-1015.

[50]   Lin, Z., J. Jin, and H. Talbot. *Unseeded Region Growing for 3D Image Segmentation.* in *the Pan-Sydney workshop on Visualisation.* 2001. Sydney: Australian Computer Society.

[51]   Long, F., H. Peng, and E. Myers, *Automatic Segmentation of Nuclei in 3D Microscopy Images of C.elegans*, in *4th IEEE International Symposium on Biomedical Imaging: From Nano to Macro.* 2007, IEEE: Arlington, VA. p. 536-539.

[52]   Blanz, W.E. and S.L. Gish, *A connectionist classifier architecture applied to image segmentation*, in *Pattern Recognition, 1990. Proceedings., 10th International Conference on.* 1990, IEEE: Atlantic City, NJ. p. 272-277.

[53]   Phukpattaranont, P. and P. Boonyaphiphat, *Segmentation of Cancer Cells in Microscopic Images using Neural Network and Mathematical Morphology*, in *SICE-ICASE International Joint Conference.* 2006, IEEE: Bexco, Busan, Korea. p. 2312-2315.

[54]   Liao, S., et al. *Representation Learning: A Unified Deep Learning Framework for Automatic Prostate MR Segmentation.* in *Medical Image Computing and Computer-assisted Intervention: Miccai International Conference on Medical Image Computing and Computer-assisted Intervention.* 2013.

[55]   Sahiner, B., et al., *Image feature selection by a genetic algorithm: Application to classification of mass and normal breast tissue.* Medical Physics, 1996. **23**(10): p. 1671-1684.

[56]   Chen, D.-H. and Y.-N. Sun, *A self-learning segmentation framework - the Taguchi approach.* Computerized Medical Imaging and Graphics, 2000. **24**(5): p. 283-296.

[57]   Manikandan, S., et al., *Multilevel thresholding for segmentation of medical brain images using real coded genetic algorithm.* Measurement, 2014. **47**: p. 558-568.

[58]   Karkavitsas, G. and M. Rangoussi, *Object localization in medical images using genetic algorithms.* International Journal of Medical, Health, Biomedical and Pharmaceutical Engineering, 2007. **1**(2): p. 66-69.

[59]   Kanade, T., et al. *Cell image analysis: Algorithms, system and applications.* in *Applications of Computer Vision (WACV), 2011 IEEE Workshop on.* 2011.

[60]   Ray, N., S.T. Acton, and K. Ley, *Tracking leukocytes in vivo with shape and size constrained active contours.* IEEE Transactions on Medical Imaging, 2002. **21**(10): p. 1222-1235.

[61]   Mukherjee, D., N. Ray, and S Acton, *Level set analysis for leukocyte detection and tracking.* IEEE Transactions on Image Processing, 2004. **13**(4): p. 562-572.

[62]   Maska, M., et al., *Segmentation and Shape Tracking of Whole Fluorescent Cells Based on the Chan–Vese Model.* IEEE Transactions on Medical Imaging, 2013. **32**(6): p. 995 - 1006.

[63]   Comaniciu, D., V. Ramesh, and P. Meer, *Real-time tracking of non-rigid objects using mean shift*, in *IEEE Conference on Computer Vision and Pattern Recognition.* 2000, IEEE: Hilton Head Islan, SC. p. 142-149.

[64]   Debeir, O., et al., *Tracking of migrating cells under phase-contrast video microscopy with combined mean-shift processes.* IEEE Transactions on Medical Imaging, 2005. **24**(6): p. 697-711.

[65]   Kalman, R., *A new approach to linear filtering and prediction problems.* Transactions of the ASME, 1960. **82**(D): p. 35-45.

[66]   Godinez, W.J. and K. Rohr. *Tracking virus particles in fluorescence microscopy images via a particle Kalman filter.* in *Biomedical Imaging (ISBI), 2015 IEEE 12th International Symposium on.* 2015.

[67]   Chen, X., X. Zhou, and S.T. Wong, *Automated segmentation, classification, and tracking of cancer cell nuclei in time-lapse microscopy.* IEEE Transactions on Biomedical Engineering, 2006. **53**(4): p. 762-766.

[68]   Vincent, L., *Morphological grayscale reconstruction in image analysis: Applications and efficient algorithms.* IEEE Transactions on Image Processing, 1993. **2**(2): p.

176-201.

[69]   Hauwer, C.D., et al., *In vitro motility evaluation of aggregated cancer cells by means of automatic image processing.* Cytometry, 1999. **36**(1): p. 1-10.

[70]   Padfield, D., J. Rittscher, and B. Roysam, *Coupled minimum-cost flow cell tracking for high-throughput quantitative analysis.* Medical Image Analysis, 2011. **15**(4): p. 650-668.

[71]   Bise, R., Z. Yin, and T. Kanade. *Reliable cell tracking by global data association.* in *Biomedical Imaging: From Nano to Macro, 2011 IEEE International Symposium on*. 2011.

[72]   Amat, F., et al., *Fast, accurate reconstruction of cell lineages from large-scale fluorescence microscopy data.* Nature methods, 2014. **11**(9): p. 951-958.

[73]   Magnusson, K.E.G., et al., *Global Linking of Cell Tracks Using the Viterbi Algorithm.* IEEE Transactions on Medical Imaging, 2015. **34**(4): p. 911-929.

[74]   Huntley, J.M. and H. Huntley, *Temporal phase-unwrapping algorithm for automated interferometry analysis.* Appl. Opt., 1993. **32**(17): p. 3047-3052.

[75]   Salder, H.O. and J.M. Huntley, *Temporal phase unwrapping: application to surface profiling of discontinuous objects.* Appl. Opt., 1997. **36**(13): p. 2770-2775.

[76]   Ching, N.H., D. Rosenfeld, and M. Braun, *Two-dimensional phase unwrapping using a minimum spanning tree algorithm.* IEEE Transactions on Image Processing, 1992. **1**(3): p. 355-361.

[77]   Flynn, T.J., *Two-dimensional phase unwrapping with minimum weighted discontinuity.* Journal of the Optical Society of America A 1997. **14**(10): p. 2692-2701.

[78]   Zhong, H., et al., *An Improved Quality-Guided Phase-Unwrapping Algorithm Based on Priority Queue.* IEEE Geoscience and Remote Sensing Letters, 2011. **8**(2): p. 364-368.

[79]   Weng, J.-F. and Y.-L. Lo, *Integration of robust filters and phase unwrapping algorithms for image reconstruction of objects containing height discontinuities.* Optics express, 2012. **20**(10): p. 10896-10920.

[80]   Huang, M.J. and C.-J. Lai, *Innovative phase unwrapping algorithm: hybrid approach.* Opt. Eng., 2002. **41**(6): p. 1373-1386.

[81]   Huang, Y., et al. *Path-independent phase unwrapping using phase derivative and total-variation (TV) denoising.* in *Biomedical Optics and 3-D Imaging*. 2012. Miami, Florida: Optical Society of America.

[82]   Chang, Y.S., et al., *The significance of morphological observation of blood cells in the diagnosis of hematological diseases.* Laboratory Medicine, 2007. **22**(1): p. 78-80.

[83]   Cheng, X.M., J.M. Guo, and Y.Q. Yang, *Analysis of morphological diagnosis of bone marrow cells with 1929 samples.* Journal of China Pediatric Blood and Cancer, 2007. **12**(6): p. 271-272.

[84]   nanoAnalytics. Available from: http://www.nanoanalytics.com/en/hardwareproducts--/cellzscope/index.php.

[85]   Zangle, T.A., et al., *Quantification of Biomass and Cell Motion in Human Pluripotent Stem Cell Colonies.* Biophysical Journal, 2013. **105**: p. 593-601.

[86]   FENG, L., X. CAO, and Y. REN, *Synergistic Effect of Fibronection and Basic Fibroblast Growth Factor on Osteoblast Adhesion Efficiency.* Chinese Journal of Reparative and Reconstructive Surgery, 2007. **21**(4): p. 390-395.

[87]   Mukhopadhyay, S. and B. Chanda, *A multiscale morphological approach to local contrast enhancement.* Signal Processing, 2000. **80**(4): p. 685-696.

[88]   Popescu, G., et al., *Fourier phase microscopy for investigation of biological structures and dynamics.* OPTICS LETTERS, 2004. **29**(21): p. 2503-2505.

[89]   Withers, J.A. and K.A. Robbins, *Tracking cell splits and merges* in *IEEE Southwest Symposium on Image Analysis and Interpretation*. 1996, IEEE: San Antonio, TX. p. 117-122.

[90]   *Cell Tracking Challenge*. 2014; Available from: http://www.codesolorzano.com/cell--trackingchallenge/Cell_Tracking_Challenge/Datasets.html.

[91]   Dzyubachyk, O. and etc, *Advanced level-set-based cell tracking in time-lapse fluorescence microscopy.* IEEE Transactions on Med Imaging, 2010. **29**(6): p. 1331.

[92]   Clark, J.J., *Authenticating edges produced by zero crossing algorithms.* IEEE Transactions on Pattern Anal. Mach. Intell., 1989. **11**(1): p. 43-57.

[93]   Xie, J., S. Khan, and M. Shah, *Automatic tracking of escherichia coli bacteria.*

Proceedings of Medical Image Computing and Computer Assisted Intervention, 2008. **5241**: p. 824-832.

[94]   Li, K., et al., *Cell population tracking and lineage construction with spatiotemporal context.* Medical Image Analysis, 2008. **12**(5): p. 546-566.

[95]   Sahoo, P.K., S. Soltani, and A.K.C. Wong, *A survey of thresholding techniques.* Computer Vision, Graphics, and Image Processing, 1988. **41**(2): p. 233-260.

[96]   McInerney, T. and D. Terzopoulos, *Deformable models in medical image analysis: a survey.* Med Image Anal, 1996. **1**(2): p. 91-108.

[97]   KOSKO, B., *Fuzzy Entropy and Conditioning.* INFORMATION SCIENCES, 1986. **40**: p. 165-174.

[98]   Ihara, S., *Information theory for continuous systems.* 1993, Singapore: World Scientific.

[99]   Zadeh, L.A., *Fuzzy sets.* Information and Control, 1965. **8**(3): p. 338-353.

[100]   Jiang, X., G. Tang, and L. Xu, *Method for image segmentation based on fuzzy theory.* Computer Engineering and Design, 2007. **28**(16): p. 3940-3942.

[101]   Genovesio, A., et al., *Multiple particle tracking in 3-D+t microscopy: method and application to the tracking of endocytosed quantum dots.* IEEE Transactions on Image Processing, 2006. **15**(5): p. 1062-1070.

[102]   Akansu, A.N., W.A. Serdijn, and I.W. Selesnick, *Wavelet Transforms in Signal Processing: A Review of Emerging Applications.* Physical Communication, 2010. **3**(1): p. 1-18.